Master's thesis

NTNU
Norwegian University of Science and Technology
Faculty of Natural Sciences
Department of Materials Science and Engineering

Harald Skar

Parameter Optimization of Mini 3D Printer for Additive Manufacturing of Hypereutectic Aluminum Silicon Alloys

Master's thesis in Materials Science and Engineering
Supervisor: Yanjun Li
Co-supervisor: Yijiang Xu and Eivind Johannes Øvrelid
June 2023

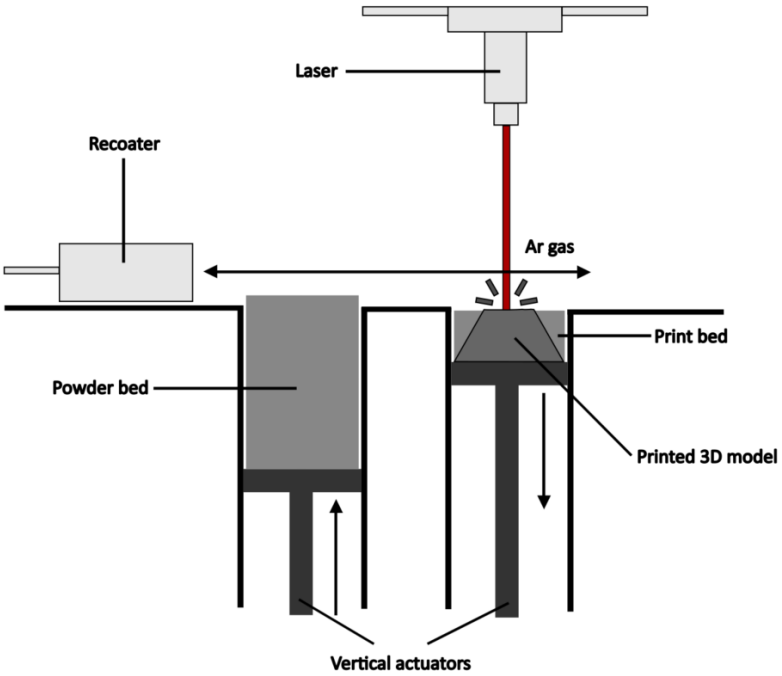

Harald Skar

NTNU
Norwegian University of
Science and Technology

Harald Skar

Parameter Optimization of Mini 3D Printer for Additive Manufacturing of Hypereutectic Aluminum Silicon Alloys

Master's thesis in Materials Science and Engineering
Supervisor: Yanjun Li
Co-supervisor: Yijiang Xu and Eivind Johannes Øvrelid
June 2023

Norwegian University of Science and Technology
Faculty of Natural Sciences
Department of Materials Science and Engineering

NTNU
Norwegian University of
Science and Technology

Preface

This report is part of the TMT4905 master's thesis and has been performed at the Department of Material Science and Engineering at NTNU in the spring of 2023.

I would like to thank my supervisor Yanjun Li for his guidance and feedback during the project. I would also like to thank my co-supervisors Yijiang Xu and Eivind Johannes Øvrelid for their help throughout the project. Special thanks are extended to Yingda Yu for always being of assistance at the SEM lab.

Trondheim, June 2023

Harald Skar

Abstract

This thesis will inquire into the continuously expanding field of additive manufacturing (AM) techniques employed for the fabrication of complex three-dimensional metal components. Particularly, there has been a surge of interest from a manifold of industries in utilizing selective laser melting (SLM) to produce aluminum-based products due to their favorable characteristics, including lightweight, versatile applications, and moderate mechanical strength. The rapid cooling rates inherent to the AM process offer the potential for refining the metal microstructure, thereby significantly enhancing the strength of the printed components. Nevertheless, the exploration of aluminum alloys in the field of 3D printing is still in its emerging stages, requiring further development of printing techniques and a deeper understanding of the response of various aluminum alloys to SLM methods.

The aim of this study was therefore to optimize the printing parameters of a SLM based mini 3D printer recently developed at the SINTEF-NTNU lab, based on a laser pulse laser source. The metal powder used in the SLM process was a gas-atomized hypereutectic Al-40Si alloy. In particular, the influence of scanning speed, laser power, repetition rate, hatching distance, and different scanning strategies was systematically investigated. The parameter testing was carried out starting with single-track scanning of one single layer ($\sim$50 μm) of Al-40Si powder on a wedge-cast Al-40Si plate. Furthermore, multiple tracks and closely hatched scans were performed on the same single layer of powder. Two additional scanning strategies were conducted, which involved preheating the building platform and rescanning with 50% laser power, respectively. In the final parameter optimization part, multiple-layered printed parts were produced with up to 4 layers of Al-40Si powder. The samples were thereupon characterized with SEM, OM, and ImageJ, where increasing laser scanning speed was found to decrease the droplet diameter of the remelted powder. The optimal printing parameters for this specific 3D printer employing the Al-40Si alloy proved to be scanning speeds of 10-30 mm/s, 28.5 W (maximum) laser power, 100 kHz (maximum) repetition rate, and 20 % hatching overlap. The balling phenomenon emerged as a major issue throughout the parameter optimization work, where poor wetting between oxide layers, Marangoni convection, and Plateau-Rayleigh instability was put forward as possible causes. The preheating and rescanning approaches were observed to have a negligible effect on the predicament of balling. Meanwhile, high-temperature preheating proved to form larger droplets than low-temperature preheating. The same effect, i.e. general larger droplet sizes, was found when performing rescanning of the same scanning pattern with 50% laser power. The existing challenges with the mini printer equipment and the methodology used were also brought up as reasons for the porosity obtained in the printed parts. Further improvements to the mini printer and printing strategy are suggested for future work.

Sammendrag

Denne oppgaven vil undersøke det stadig voksende feltet med additive produksjonsmetoder (AM) som brukes i produksjonen av komplekse tredimensjonale metallkomponenter. Det har spesielt vært en økning i interessen fra ulike bransjer for å benytte selektiv lasersmelting (SLM) for å produsere aluminiumsbaserte produkter på grunn av deres gunstige egenskaper, som inkluderer lav vekt, allsidige bruksområder og moderat mekanisk styrke. De raske kjølehastighetene forbundet med AM-prosessen, gir potensiale for å forbedre mikrostrukturen og dermed øke styrken til de trykte komponentene betydelig. Utforskningen av aluminiumslegeringer innen 3D-printing er imidlertid fortsatt i en tidlig fase, der det er behov for videre utvikling av printe-teknikker og en dypere forståelse av hvordan ulike aluminiumslegeringer responderer på SLM-metoder.

Målet med denne studien var derfor å optimalisere laserparametrene til en mini 3D-printer basert på SLM-teknologi, nylig utviklet ved SINTEF-NTNU laboratoriet, som benytter en pulserende laser som energikilde. Metallpulveret som ble brukt i SLM-prosessen var en gassatomisert hypereutektisk Al-40Si-legering. Spesielt ble innflytelsen av skannehastighet, laserkraft, repetisjonsfrekvens, avstand mellom skannelinjer og ulike skannestrategier vurdert. Parametertestingen ble utført ved å starte med enkeltsporet laserskanning av ett enkelt lag ($\sim$50 μm) med Al-40Si-pulver på en kilestøpt Al-40Si-byggeplate. Videre ble det utført flere spor og tett skraverte skanninger på det samme laget med pulver. To andre skannestrategier ble utført, som involverte henholdsvis oppvarming av byggeplattformen og reskanning med 50 % laserkraft. I den siste delen av parameteroptimaliseringen ble flerlags komponenter produsert med opptil 4 lag Al-40Si-pulver. Prøvene ble deretter karakterisert med SEM, OM og ImageJ, der det ble funnet at økende laserskannehastighet reduserte diameteren til det omsmeltede Al-40Si-pulveret. De optimale parameterne for denne spesifikke 3D-printeren som bruker Al-40Si-legeringen viste seg å være skannehastigheter på 10-30 mm/s, 28.5 W (maksimal) laserkraft og 100 kHz (maksimal) repetisjonsfrekvens. Sfæroidisering av det omsmeltede metallpulveret viste seg å være en utfordring gjennom parameteroptimaliseringen, der dårlig fukting mellom oksidlag, Marangoni-konveksjon og Plateau-Rayleigh-instabilitet ble foreslått som mulige årsaker. Oppvarming og reskanning viste seg å ha neglisjerbar effekt på sfæroidisering av smelten. Samtidig viste foroppvarming ved høy temperatur seg å danne større dråper av smelte enn foroppvarming ved lavere temperatur. Samme effekt, det vil si generelt større dråpestørrelser, ble observert når det ble utført reskanning av samme skannemønster med 50 % laserkraft. De eksisterende utfordringene med mini-printerutstyret og den eksperimentelle metodikken ble også nevnt som årsaker til porøsiteten som oppstod i de produserte prøvene. Videre forbedringer av mini-printeren og printe-strategien blir foreslått som muligheter for videre arbeid.

Table of Contents

List of Figures

List of Tables

Abbreviations

2D two-dimensional. 5

3D three-dimensional. ix, 1, 3, 5

AM Additive manufacturing. ix, 1, 3, 11, 14, 15

BSE backscattered electrons. 36

CAD computer-aided design. ix, 4, 5

CW continuous wave. 7

DED direct energy disposition. 3

DMLS direct metal laser sintering. 3

EBM electron beam melting. 3

EPM electronic packaging materials. 17

HAZ heat affected zone. 7, 10

L-PBF laser-assisted powder bed fusion. 15

LBW laser beam welding. x, 10, 11

LOM laminated object manufacturing. 3

OM optical microscope. iii, 2, 29, 32, 35, 36, 38, 48, 57

PBF powder bed fusion. 3

PDS powder distribution system. 24

PSD powder size distribution. 10

SE secondary electrons. 36

SEM scanning electron microscope. iii, 2, 32, 35–37, 40, 42, 44, 46, 47, 50, 51, 53, 54, 56–58, 60, 61

SLM selective laser melting. iii, v, ix, x, 1–7, 9–16, 18, 19, 21, 22, 24, 26, 27, 34, 35, 38, 48, 49, 57, 58, 60–63

SLS selective laser sintering. 3

STL standard triangle language. ix, 4, 5

TGM thermal gradient mechanism. 12

USP ultra short pulses. 1, 7, 8

VLM Visual Laser Marker. 33, 35, 45

1 Introduction

Additive manufacturing (AM) is a terminology used to describe all computer-controlled processing techniques that use three-dimensional (3D) data to construct components layer by layer. Multiple approaches to AM is available today, but a common feature for all of them is the unique degree of freedom in design they offer. This combined with short design-to-manufacture time has given AM technologies a foothold within a multitude of industries, such as the automobile, biomedical, and aerospace industries [1]. The application of AM has also shown exceptional growth over the last few decades, where implementation in other fields will most presumably follow [2].

Selective laser melting (SLM) is a AM method that is designed to print metal components by fusing metal powder together. This technique offers a wide use of alloys, such as steel, aluminum, copper, and titanium-based alloys. Aluminum-based alloys have particularly gained recognition due to their light weight, combined with moderate mechanical strength, excellent corrosion resistance, and good weldability. However, despite the immense collective research effort within AM of Al-alloys over recent years, there are still many alloys and utilizations yet to be discovered. The hypereutectic Al-Si alloy (>13 wt% Si) is an alloy that exhibits the qualities mentioned earlier, along with high thermal conductivity and a thermal expansion coefficient similar to that of semiconductor materials [3]. This makes the Al-Si alloy well-suited for use in for example electronic packaging applications. Nevertheless, the great majority of studies have focused on the hypoeutectic compositions of close to 12 wt % Si, such as AlSi10Mg [4]. Up until recently, relatively few studies have been conducted on high-silicon content aluminum alloys in the SLM process [5]. One study by Kang et al. [6], however, demonstrated the possibility of producing nearly dense parts of hypereutectic Al-Si-alloys through SLM. Another study by Ullsperger et al. [7] showed promising results by utilizing ultra short pulses (USP) in a SLM process on an Al-40Si powder. Meanwhile, it is important to emphasize the need for further research to find the full potential of the Al-40Si alloy in SLM printed products.

The main benefit of using SLM instead of other traditional methods producing Al-Si components is the significantly higher cooling rates involved. It is widely recognized that the cooling rates during the process have a direct impact on the microstructure and grain size of the finished product, i.e. refining is known to happen with higher cooling rates [8]. The SLM process will therefore give a dramatic decrease in average grain size compared to conventional techniques, improving the mechanical strength of the material. In theory, this enables the production of complex structures with super high strength, which would not be possible with standard printing techniques. The main issue, however, is to adjust the SLM process so that it couples with the specific alloy in use. For instance, Rashid et al. [9] reported that varying a single SLM parameter, can result in significantly different microstructural and mechanical properties of the printed parts. Therefore, it is crucial to understand the effects of the different SLM process parameters.

The main objective of this thesis is to investigate the influences of different processing parameters on the properties of an Al-40Si alloy during the laser-assisted selective laser melting (SLM) printing process. Continuous optimization of printing parameters will be presented in the experimental section. The initial testing consisted of relatively simple single-track scans of a single-layer Al-40Si powder on a cast Al-40Si building plate. The scheme of parameters was then narrowed down, and more complex single-layer scanning patterns such as multiple line scans and hatched square scans were utilized. With the aim of finding the best conditions and scanning strategy, preheating, and rescanning were also tested. Lastly, multiple-layer 3D printing was carried out. The parameter testing was conducted with an in-house 3D-mini printer assembled in conjunction with a bachelor thesis by Mostad et al. [10]. A big advantage of this specific 3D printer is the ability to produce small samples, which easily can be characterized with various material characterization techniques. Thus, analysis of the SLM samples in optical microscope (OM), scanning electron microscope (SEM), and ImageJ will be presented. Lastly, the influence of the laser parameters on the printed Al-40Si parts, and the optimal laser parameters for the Al-40Si-alloy will be contemplated.

2 Background

2.1 Additive Manufacturing (3D Printing)

Additive manufacturing (AM), also known as 3D printing, is a general term used for the computer-controlled process that builds three-dimensional objects layer by layer. Today, a broad range of different techniques are practiced in the AM industry. The main difference between the numerous methods, however, is the process in which the material is deposited for each layer [2]. Some examples of such consolidation mechanisms are direct energy disposition (DED), laminated object manufacturing (LOM) and, powder bed fusion (PBF). All of these approaches have their own merits and drawbacks. When selecting a method for a specific printing task, concerns such as costs, material choice, and building speed are considered. The PBF method offers the usage of a wide range of different powders, the possibility for cost-saving by recycling excess powder, and relatively fast building speeds.

PBF selectively fuses regions in a powder bed by using a thermal energy source. To melt the substrate, various methods are employed such as direct metal laser sintering (DMLS), electron beam melting (EBM), or selective laser sintering (SLS)/selective laser melting (SLM). In this project, a SLM process is utilized as the printing method.

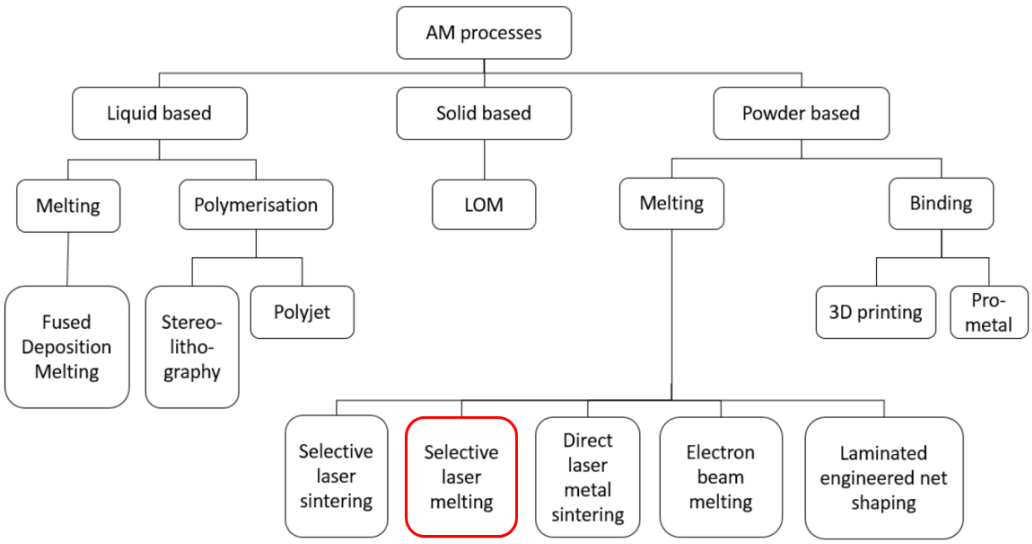

Figure 1: Overview of the most common AM processes. The SLM process, most relevant for this project, is marked in red. [11]

2.2 Selective Laser Melting (SLM)

As described in the previous section, SLM is a process where a laser is used as a heat source to selectively melt the substrate on the powder bed. The printing begins with a recoater adding a single layer of metal powder (15 - 60 µm) from the powder bed to the

build platform. A laser beam is then directed onto the layer and scans in the x-y plane to selectively melt the desired regions. This is repeated for each layer until the product is complete. The build platform is lowered by an amount equal to the layer thickness after each layer is added. The print bed is located in an inert gas chamber (e.g. Ar or N_2) to prevent oxidation during the process [12]. Fig. 2 shows an illustration of the SLM process.

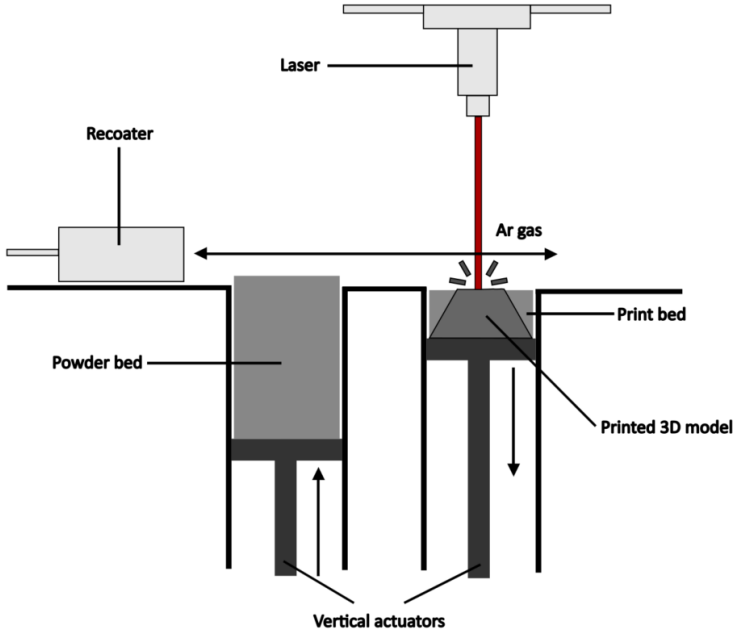

Figure 2: Sketch of the SLM printer system.

2.2.1 CAD and STL Files

The laser used in the SLM process is computer-controlled and operates on a layer-by-layer basis, following a pre-determined pattern of continuous lines. The pattern is typically obtained from a 3D computer-aided design (CAD), which is then converted into an standard triangle language (STL) file. The STL format only describes the surface geometry of the 3D object and does not include information about color or texture. The file consists of many small triangles that together make up the surface of the object, as shown in Fig. 3. This format is widely supported by many modeling software programs due to its simplicity [13].

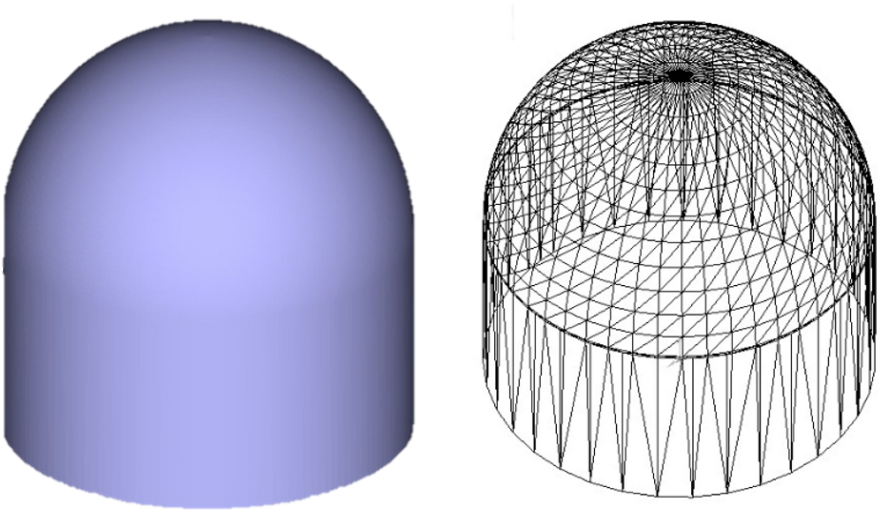

Figure 3: Illustration of a 3D CAD file to the left and the corresponding STL file to the right. [14]

2.2.2 Slicing

To construct the desired structure, the STL file must be divided into multiple layers using slicing software. The software cuts the 3D model into two-dimensional (2D) layers, with the number of slices determined by the layer thickness. The thinner the layer, the more slices will be produced. Contrarily, a thicker layer will result in fewer slices. The layer thickness is a critical factor that influences the final product's material properties and physical performance, which will be discussed in more detail in section 2.3 [15]. By stacking each layer on top of the other, the 3D structure is recreated, as shown in Fig. 4.

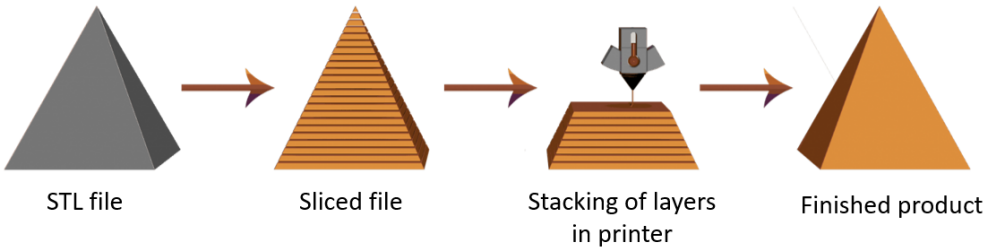

Figure 4: Illustration of the process from STL file to finished product. [15]

2.3 Influence of Printing Parameters

The optimization of material properties in SLM often relies on controlling key process parameters, such as laser power, scan speed, hatch spacing, and layer thickness. To

determine the optimal parameters for achieving optimal material properties, it is necessary to consider their interplay. One useful approach for simplifying this complex relationship is to express the process parameters in terms of linear energy density, E_L (J/mm):

$$E_L = \frac{P}{v} \tag{1}$$

where P (W) is the laser power used and v (mm/s) represents the scanning velocity. The areal energy density, E_A (J/mm^2), is given by:

$$E_A = \frac{P}{vh} \tag{2}$$

where h (µm) refers to the hatch spacing between the scanned tracks. The volumetric energy density, E_V (J/mm^3), is given by:

$$E_V = \frac{P}{vht} \tag{3}$$

where t (µm) is the layer thickness during the process [16]. As is evident from the equations (1), (2) and (3), different parameters can give the same energy density. However, it is important to mention that these equations are an oversimplification and have been experimentally proven to be inaccurate in a study by Pauly et al. [17]. The complex thermodynamic and fluid behavior present in the melt pool is shown to not be covered by the energy density equations given above. The main weakness of the formulas is that they do not consider the material properties. A more accurate equation has been proposed in another study by Thomas et al. [18]. The energy density, E' (J/mm^3), is then given by:

$$E' = \left(\frac{AP}{2vtr}\right) \cdot \left(\frac{1}{0.67\rho C_p(T_m - T_0)}\right) \cdot \left(\frac{1}{h^*}\right) \tag{4}$$

Where A is the material's absorptivity, r (m) is the laser beam radius, ρ (g/cm^3) is the material's density, C_p (J/(kg °C)) is its specific heat capacity, T_m (°C) is the melting point, T_0 (°C) is the initial temperature of the powder-bed, and h^* is the dimensionless hatch spacing derived from (h/r).

2.3.1 Laser Power, Scan Speed, and Layer Thickness

The laser power in the SLM process is of great importance as it directly impacts the temperature attained in the melt pool. Inadequate melting, poor adhesion between layers, and porosity may result from low laser power, which reduces the energy density. While laser power is a critical parameter, it must be considered in conjunction with other parameters such as scan speed and hatch spacing. Increasing the scan speed or hatch spacing can

compensate for high laser power, but there is a limit to the extent to which this can be done. Moreover, excessively high laser power can cause balling, an unwanted phenomenon, which will be discussed in Section 2.6.3. As a result, the P/v relationship is crucial in controlling the SLM process.

Moreover, the production of components of high quality requires the correct choice of powder layer thickness. For instance, if the layer thickness is too high, the powder will not melt sufficiently as the laser is unable to penetrate the layer. On the other hand, if the layer thickness is thin enough, the laser will be able to penetrate the powder completely causing it to melt adequately [19]. This phenomenon was also confirmed in a study by Sun et al. [20], where rising powder thickness led to a rising nodulizing (balling) tendency and uneven melt. The consequence of this is porosity and poor mechanical strength in the printed components. It is thus crucial to apply a suitable powder layer thickness seeking dense high-quality 3D-printed components.

2.3.2 Laser Pulse Parameters

The traditional method for SLM has relied on continuous wave (CW) lasers, but recent advancements in the use of ultra short pulses (USP) have demonstrated promising results [21]. These pulses, typically in the femto- to picosecond range, give a considerably smaller heat affected zone (HAZ) compared to CW methods. As a result, USPs are widely utilized in micro-machining and local welding processes [22]. The method works by striking the surface with laser pulses that increase the temperature of the substrate until it reaches the material's melting point. The small melt pool produced by this method offers a major advantage over traditional methods due to quicker heat extraction, leading to a finer microstructure and improved mechanical properties [23].

The heating source used in this project, namely the PowerLine F 30 laser, offers two adjustable variables in terms of laser pulse parameters; the pulse frequency and the pulse width. The pulse frequency, or repetition rate, f_{rep} (Hz), determines the pulse emission frequency. The pulse width, τ (s), quantifies the duration between the start and end of each pulse. The period, Δt (s), is related to the pulse by:

$$\Delta t = \frac{1}{f_{rep}} \tag{5}$$

The pulse energy, E_p (J), is a measure of one pulse's total emission and is given by:

$$E_p = P_{avg} \cdot \Delta t = \frac{P_{avg}}{f_{rep}} \tag{6}$$

where P_{avg} is the energy emitted if the pulse was spread over the entire period. The peak power, P_{peak}, can be estimated by:

$$P_{peak} \approx \frac{E_p}{\tau} \tag{7}$$

which gives:

$$P_{avg} = f_{rep} \cdot \tau \cdot P_{peak} = f_{rep} \cdot E_p \tag{8}$$

The equations are visualized in Fig. 5. According to equation (6), as the repetition rate, f_{rep}, increases, the energy per pulse will decrease in proportion. The inverse is also true when decreasing the repetition rate. The impact of changing the pulse width, τ, can be observed from equations (7) and (8). An increase in τ will result in a corresponding increase in both P_{avg} and E_p, given that the other parameter remains constant. Conversely, a decrease in τ will result in a decrease in energy per pulse for both P_{avg} and E_p [24].

It is also important to notice that the peak power, P_{peak}, and pulse width, τ, may have large variations, but still give the same average power, P_{avg}. For example, in a study by Ullsperger et al. [23], two USP experiments were conducted, both with an average power of 25 W. However, the pulse width was set to 500 femtoseconds and 800 picoseconds, corresponding to a peak power of 10 MW and 5 kW, respectively. Hence, by adjusting the pulse width, the peak power varied in the 10^3 order of magnitude, while still preserving the same average power. It is therefore important to consider how these parameters affect the material when irradiated, especially with respect to vaporization and ablation of the material. In general, the pulse energy threshold for ablation damage increases with increasing pulse duration. It has also been highlighted in another study by Kaden et al. [25], that it is important to maintain a high repetition rate (in the range of MHz) to obtain good melting of the substrate powder. Ullsperger et al. [26] also noticed that repetition rates under 10 MHz could cause a blasting effect on the scanned single tracks. They were also able to show that the deviation of mean track width, i.e. the homogeneity of the scanned tracks, was smaller at shorter pulse widths. It is thus critical to combine high repetition rates with small pulse widths to ensure the best printing results. Unfortunately, the PowerLine F 30, presented in Table 1, laser only offers a maximum repetition rate of 100 kHz, which could affect the quality of the printed products negatively.

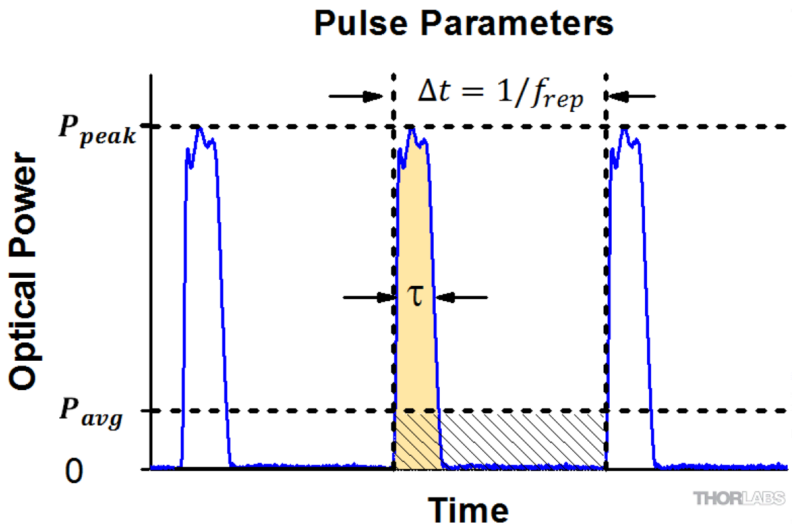

Figure 5: Illustration of the parameters used to characterize a pulsed laser. The pulse energy (E_p) is represented by the shaded area beneath the pulse curve. [24]

2.4 Feedstock Materials

Currently, a wide range of feedstock materials are used in the powder-based SLM process. Generally, the source materials can be divided into two main categories; pre-alloyed and in-situ alloyed powders [27]. Each of these categories has its unique characteristics that impact the properties of the final product.

Pre-alloyed powders, as the name suggests, are powders that possess the desired composition prior to being utilized in the SLM process. This implies that each particle in the metal powder consists of the same alloy composition. Upon irradiation by the laser beam, the powder particles simply melt together, retaining the original composition. Conversely, in-situ alloying involves adding each element in the alloy in powder form, resulting in powder particles with different compositions before printing [12]. During the laser exposure to the powder bed, the powder is melted, and the alloy is formed. However, in-situ alloying also carries the risk of insufficient mixing of the alloying elements. The advantage of both methods is the possibility for unfused particles to be recycled and reused in the same process.

2.4.1 Powder Characteristics

To get the full picture of the SLM process, it is important to consider the powder characteristics. A sufficient material deposition process requires good flowability and high packing density within the powder [27]. If these powder qualities are not present, porosities and other defects may easily emerge in the printed components. Morphology, granulometry, rheology, and thermal properties are all subjects that play a crucial role in the behavior of

the feedstock powder. When it comes to powder morphology, spherical-shaped particles are most often desired. This is due to their ability to increase both density packing and rheology properties. Also important is the powder granulometry, i.e. the powder size distribution (PSD). PSD quantifies the particle sizes in terms of volume composition [28]. This plays a particularly important role when recycling the powder. Some granulometry changes may occur in the recycled powder due to detachment from the built structure, which means that the PSD becomes more dominated by coarser particles. Nevertheless, few studies have been conducted on the influence of PSD on feedstock quality, hence giving difficulties in predicting the powders' performance solely based on this information. The average particle size for the Al-40Si powder used in this project is roughly 40 μm, as the micrographs in Fig. 6 show.

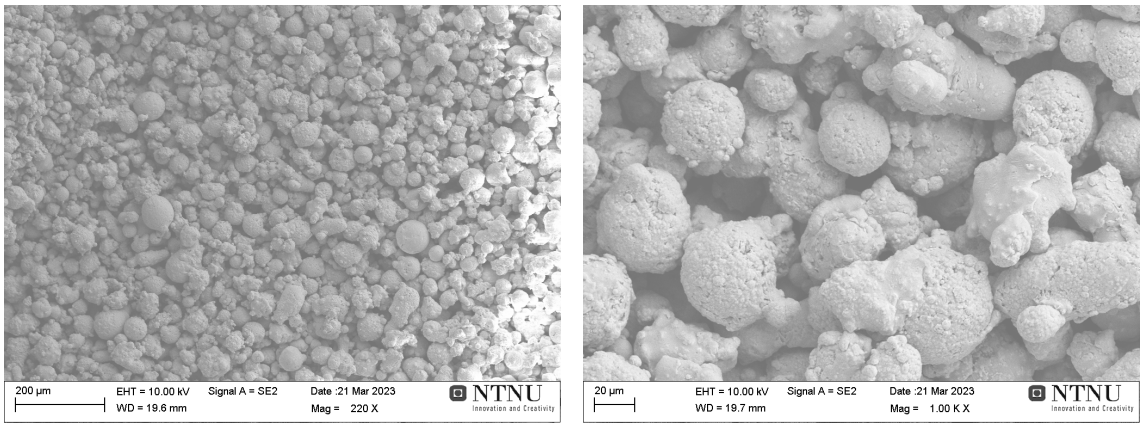

(a) (b)

Figure 6: Al-40Si powder used in this study imaged in SEM at (a) 220x, and (b) 1000x magnification.

2.5 Laser Beam Welding (LBW)

The process of laser beam welding (LBW) is a relatively new technique developed for joining materials. LBW has emerged as a highly advantageous welding method for aluminum alloys. By directing a concentrated laser beam, the technique produces a narrow and profound weld and reduces the heat affected zone (HAZ) considerably. To comprehend the key features of this method can be useful knowledge in the SLM. LBW can be categorized into two welding modes: thermal conductive welding and deep penetration welding, also known as keyhole welding [29].

Thermal conduction welding is characterized by using low power density and thereby only affecting the material surface. The heat build-up at the surface is transmitted deeper into the metal by thermal conducting forces. This creates a hemispherical melt pool and HAZ, as can be seen in Fig. 7 (a). The melt pool is stable, giving fewer defects such as porosity.

To perform keyhole welding, a higher laser power density is necessary, leading to violent

vaporization of the material. This results in the formation of a keyhole-shaped cavity, allowing the laser to penetrate deeper into the material. The cavity absorbs most of the laser energy, generating plasma due to the partial ionization of metal vapor, as shown in Fig. 7 (b). However, this process can cause the formation of pores in the melt pool during solidification, negatively impacting the material's mechanical properties. The power density E' (J/mm^3) and the parameters given in Eq. (4) determine the welding mode achieved, with the aluminum alloys having a higher threshold for keyhole welding in theory due to their low laser absorptance [30].

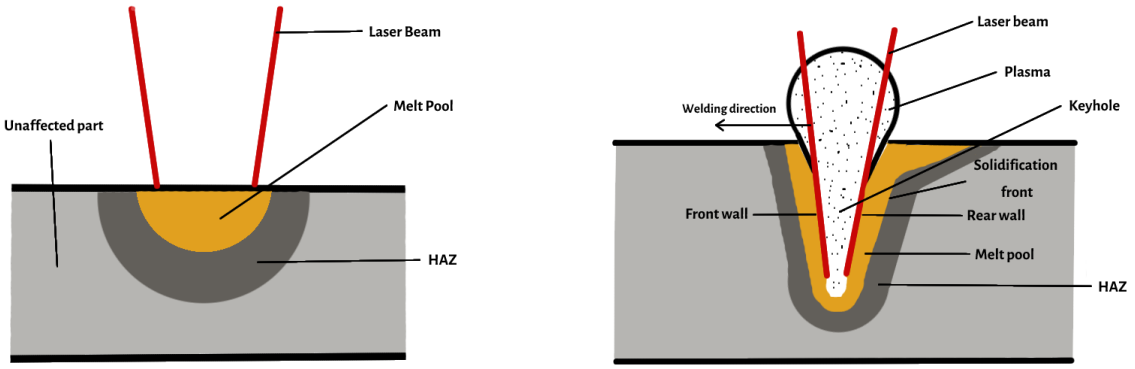

(a) (b)

Figure 7: Basic principles of (a) the LBW modes thermal conductive welding, and (b) keyhole welding.

2.6 Defects in SLM

Structures built with SLM are prone to suffering from defects due to complex heat and mass transfer mechanisms. In order to improve the material properties of the 3D printed products, it is essential to understand where the flaws originate from. The most frequent ones, namely porosity, residual stresses, balling, and oxidation, will be discussed in the following sections.

2.6.1 Porosity

Porosity is a commonly occurring defect in laser-irradiated aluminum alloys, and its presence in solidified material can result in stress concentrations, leading to reduced mechanical strength. Therefore, it is crucial to prevent porosity, almost regardless of the intended application. Two types of porosity can occur, namely metallurgical and keyhole porosity.

Metallurgical pores are small, spherical bubbles, typically up to tens of microns in size [31], originating from hydrogen or other gases in the melt pool. During laser irradiation, hydrogen is absorbed in the melt pool, and upon cooling, supersaturated hydrogen repels the melt due to a decrease in hydrogen solubility. Because the AM process involves rapid

cooling, the bubbles do not have enough time to migrate, leading to porosity, illustrated in Fig. 8 [32]. To avoid hydrogen-induced metallurgical pores, it is essential to reduce the humidity of the substrate surface by utilizing pre-heat treatments [33].

Keyhole pores, in contrast, are large, irregularly shaped cavities, usually, hundreds of microns in size [31], shown in Fig. 8 (b-d). These pores occur when the melt pool necks and the rear wall collapse, trapping bubbles opposite the welding direction by the solidification front. The process is illustrated in Fig. 7b (a). The primary approach to prevent keyhole pores is by controlling the laser parameters.

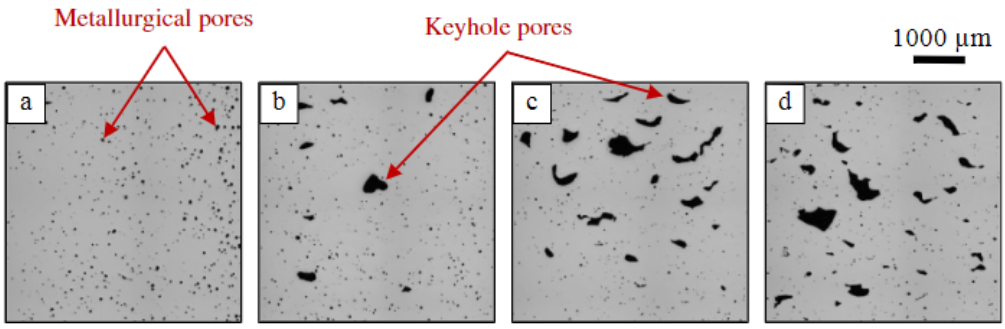

Figure 8: The progress of pores for a SLM AlSi10Mg alloy with increasing scan speeds. (a) 250 mm/s, (b) 500 mm/s, (c) 750 mm/s, and (d) 1000 mm/s. [34]

2.6.2 Residual Stresses

During the SLM process, the high irradiation energy leads to steep thermal gradients, resulting in residual stress accumulation. These stresses can cause thermal deformations, delamination, and distortions such as part warping, which can propagate over multiple layers [27]. The two main mechanisms responsible for this effect are the thermal gradient mechanism (TGM) and the cool-down phase mechanism.

TGM occurs when the already solidified underlying layers are heated upon melting a new layer. This causes the material near the irradiation zones to expand, which is restricted by the colder portions of the material located further away. Consequently, stress is induced into the material, and if the stresses exceed the maximum yield limit of the material, it may cause cracking. On the other hand, the cool-down phase mechanism occurs when the melt pool is cooled. During this process, the material contracts, which is restrained by the underlying layers, leading to tensile stresses at the top and compressing stresses at the bottom. Similar to TGM, this can cause cracking, particularly in the upper part experiencing tensile stress. This effect increases with the number of layers, where the largest tensile stresses occur at the surface of the final deposited layer [35].

Addressing these issues has been a significant focus of recent research, and methods have been developed to prevent these unwanted effects [35]. For instance, it is common to

preheat the powder bed, remelt the surface of each deposited layer before adding the next one, and select a suitable scan strategy. These measures against residual stresses will be described in more detail in section 2.7.

2.6.3 Balling

Balling is a common defect in SLM processes that can result in poor inter-layer bonding, high porosity, and poor surface quality. This defect is typically caused by insufficient energy density resulting from either high scanning speeds or low laser beam power [36].

When balling is caused by high scanning speeds, it can be observed through the formation of coarsened, spherical-shaped agglomerates. In a study conducted by Simichi et al. [37], the laser beam was found to concentrate on a spot on the powder bed for approximately 4 ms before moving on to a new spot. As the temperature rises, the surface of the powder particles will melt. The amount of liquid formation is determined by the scanning speed; if the speed is too high, the particles will not have sufficient time to melt, which will restrict the flow and rearrangement of powder particles. As a result, the powder will agglomerate to form a size equivalent to the laser beam's diameter. This phenomenon is depicted in Figure 9.

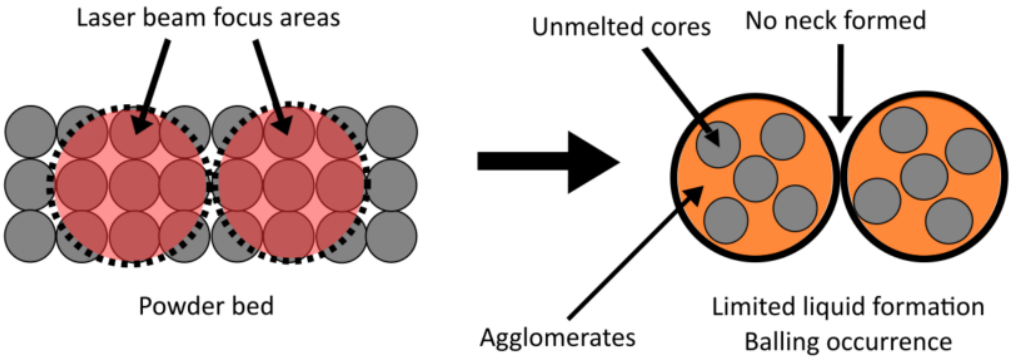

Figure 9: Sketch of balling mechanism due to high scan speed.

The second type of balling occurs when both the laser power and scan speeds are too high. As the laser beam moves across the surface, it generates a continuous cylindrical molten track, with the diameter of the track decreasing due to the decrease in energy density from the laser at high scan speeds. A smaller diameter of the melt pool results in an increase in the surface energy of the liquid, making the melt more unstable and causing droplets to splash from the molten track onto the surrounding surface. Upon solidification, numerous micro-scale spherical-shaped particles can be observed on the surface. Both types of balling can be prevented by carefully controlling the scan speed and laser beam power [36].

2.6.4 Oxidation

Oxidation of the metal substrate is a serious issue in the AM process, causing difficulties in producing components of high quality. The combination of high temperatures present during melting and the presence of oxygen contribute to the formation of oxide films, as Fig. 10 demonstrates [38]. Previous work has proven that the oxide layers have the tendency to induce balling, promote porosity, affect the fluid flow in the melt pool, and influence the absorption of the laser energy [39]. As mentioned in the previous sections this will have adverse effects on the final product, such as poor inter-layer bonding. Obviously, a necessity for oxidation to occur is the presence of oxygen in the surrounding atmosphere. Therefore, a measure against the unfavorable consequences of oxidation is to conduct the SLM process in a protective environment, with low oxygen content. By flushing the printing chamber with noble gases such as argon or nitrogen, an inert atmosphere is achieved. Often it is required to have oxygen levels lower than 0.1-0.2 % during the process to ensure a non-reactive atmosphere [12]. However, if we look at the Ellingham diagram in appendix A and the melting points of aluminum (660.3 °C) and silicon (1410 °C), it is evident that the equilibrium partial pressure of oxygen must be extremely low to prevent oxidation of aluminum ($< 10^{-40}$ $\frac{p_{O_2}}{atm}$) and silicon ($< 10^{-16}$ $\frac{p_{O_2}}{atm}$) [38]. Therefore, oxidation cannot be completely avoided under normal operating conditions.

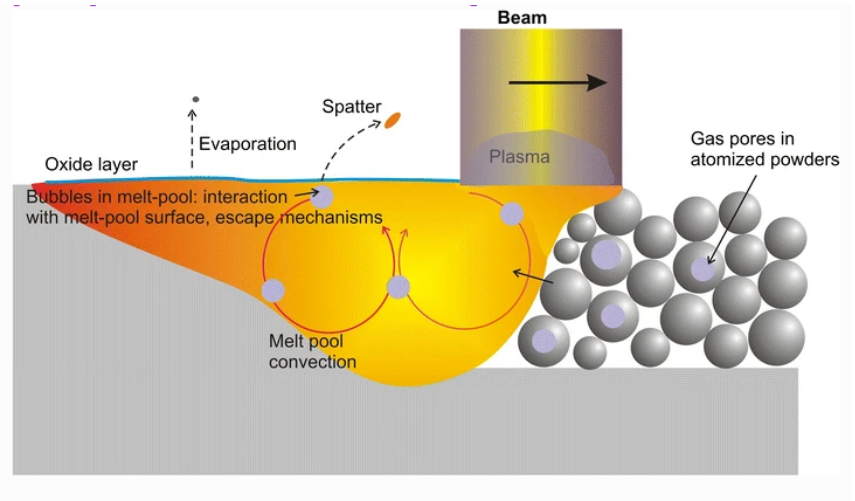

Figure 10: Sketch of the formation mechanism of pores during melting. [28]

Another concern with oxidation in the SLM process, is the contaminations found in the metal powder itself, also illustrated in Fig. 10. Compared to cast or wrought products, metal powders have a much higher degree of contamination. This is due to their significantly higher surface area per unit volume [40]. Consequently, it is extremely difficult to avoid oxides forming on the powder particles while in storage or in the handling process before introducing an inert atmosphere. In addition, depending on production method and shelf life, powders are generally prone to hold other impurities such as moisture, organics, adsorbed gases, and nitride films on particle surfaces [40].

2.7 Printing Techniques within SLM

Within the AM branch of SLM many printing techniques have been developed with the aim to achieve the best possible material properties. This may involve small variations in printing conditions or the scanning strategy used. In this section, some of the most common SLM printing techniques used to avoid the defects mentioned above are presented.

2.7.1 Preheating

By preheating the platform or substrate to be printed on, several beneficial effects can be achieved. As stated in section 2.6.2, residual stresses that build up during the printing process are mainly caused by the major temperature gradient present in the process. Moreover, the steep temperature gradient creates a cellular structure inside the deposited layers in the AM process. Both of these mechanisms weaken the mechanical strength of the manufactured components. In a study by Mertens et al. [41] the application of a base plate preheating during the SLM process of an Al7075 alloy was tested. They found that preheating the building platform up to 400 °C can reduce 50 % of the residual stresses, though it may fail to completely prevent cracking. It is also worth noting that the effect of the preheated base plate was significantly smaller than changing laser parameters such as scan speed or laser power. These observations have also been confirmed for other alloys such as steels in other studies [42, 43].

Because of the Marangoni convection described in detail in section 2.11, it could be favorable to decrease the thermal gradients between the melt and the building platform. This can be achieved with different approaches, for instance by installing a thermoelement in the base plate or by pre-scanning the surface of the substrate.

2.7.2 Pattern Design and Scan Strategy

The computer-controlled process of AM offers a multitude of different scan strategies, which is the geometrical pattern followed by the laser. During the rapid movement of the laser in the SLM process, the temperature distribution undergoes significant changes. This results in a high temperature gradient due to the intense local energy input, leading to nonuniform deformations and high residual stresses in the final parts [44]. Consequently, it can make a great difference in the quality of the final product by altering the scanning pattern. For example, Zhang et al. [45] found that rotating the scanning angle 90° between layers of an L-PBF printed Ti6Al4V alloy can reduce the residual stresses considerably. Defects such as balling can also be avoided in the SLM process by selecting an applicable pattern design [46].

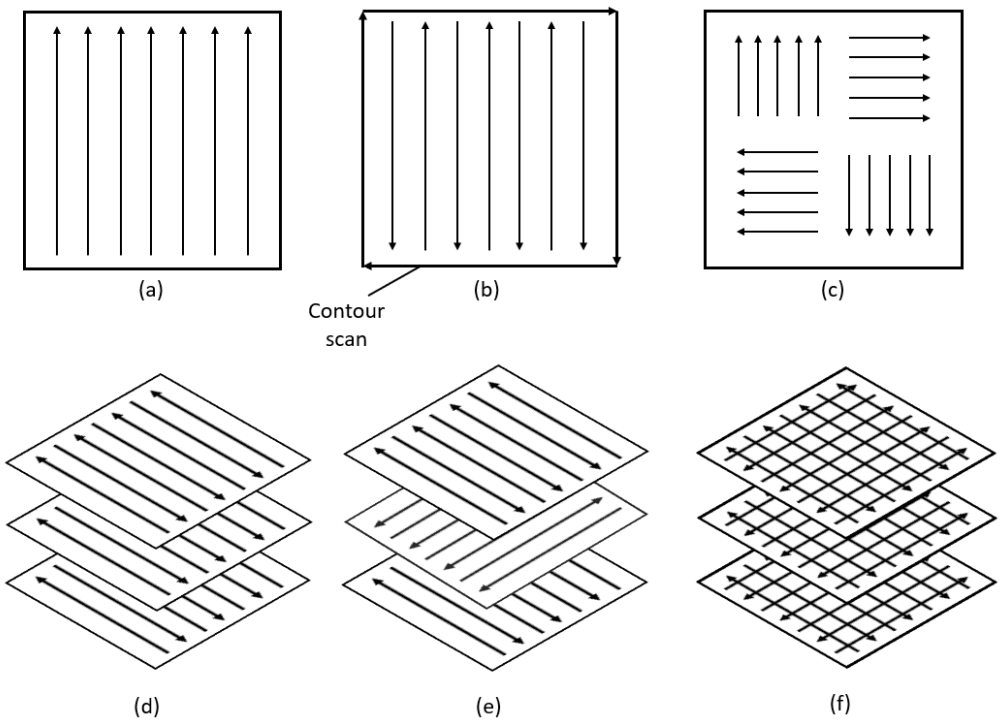

Figure 11: Schematic of different kinds of scanning strategies. (a) Uni-directional scan, (b) bi-directional with contour scan, (c) island scan, (d) bi-directional multi-layer scan, (e) bi-directional with 90° rotation of scan vector between layers, (f) cross scan.

For a single layer, it is possible to vary scanning directions, scanning sequence, scanning vector rotation angle, scanning vector length, scanning time, and hatch spacing, all of which influence the properties of the 3D-printed product [47]. The most common scanning strategies are the bi-directional and the uni-directional scanning strategies, illustrated in 11 (a) and (b). As is evident from these schematic drawings is the relatively large length of each scanning vector. Such long scanning lines may cause stress accumulation to occur during the printing process. A way of solving this problem is to divide the scan into smaller squares or islands, as can be seen in Fig. 11 (c). The contour scans in Fig. 11 (b), are often added to improve surface finish [48]. It is also common to rotate the scanning pattern by 90° as presented in Fig. 11 (e) and (f), which may contribute to relieving some of the residual stress build-ups in the material. It is important to note that the strategies of scanning presented here are just a small selection of the possibilities available. By varying scanning patterns between each layer, seemingly limitless variations of scanning strategies exist.

Rescanning

One promising approach to the SLM printing process is the scanning strategy of rescanning. This process can easily be explained by performing the same scanning pattern one

or more times on one single layer. It was suggested in the study by Ullpsberger et. al [7] that rescanning the lines of an Al-40Si alloy at least 3 times could help the uniformity of the melt pools. Shiomi et al. [35] also found that the tensile residual stresses effectively decrease by conducting rescanning on a 3D-printed standard steel alloy. In light of this, rescanning has emerged as a particularly favorable scanning strategy.

2.8 Strengthening Mechanisms

To achieve a mechanically strong material there are different methods to modify the relatively soft aluminum-based alloys. Some examples of the mostly used strengthening mechanism include grain boundary strengthening, solid-solution strengthening, strain hardening, and precipitation hardening [49]. The main principle for all of these strengthening mechanisms can be explained by their ability to hinder dislocation movement, i.e. plastic deformation. Weak materials will thus have less capability of stopping dislocation movement when stress is applied to the material. The most important mechanism to understand in most cases is grain boundary strengthening. Grain boundaries work as a barrier for dislocation, which increases the threshold for plastic deformation to occur, i.e. grain boundary strengthening. The immediate increase in strength of grain refined alloys can be theoretically explained by the Hall-Petch relation:

$$\sigma_y = \sigma_0 + k_y d^{-1/2} \tag{9}$$

where σ_y is the yield stress, σ_0 is the resistance in the lattice to dislocation motion, k_y is the strengthening coefficient (a constant specific to each material), and d is the average grain diameter [50]. From equation (9) it is evident that an increase in average grain diameter, d, responds to a decrease in yield stress, σ_y. Conversely, a refining of the microstructure (or decrease in average grain diameter, d), will increase the yield stress, σ_y, of the material. Also to be mentioned is the effect of increased ductility with increasing grain numbers.

2.9 Al-40Si Alloy

The Al-40Si alloy has a high silicon content which gives specific properties that have among others gained interest as being the next generation of electronic packaging materials (EPM) [51]. Al-Si alloys are favorable for EPM applications due to low density (< 2.5 g/cm^3), high thermal conductivity, and similar thermal expansion coefficient as semiconductor materials [3]. Also, due to excellent elasticity and corrosion resistance properties, the alloy has gained a foothold in the automobile and aerospace industries [52]. However, a great issue when dealing with hypereutectic Al-Si alloys (>13 wt % Si) in conventional manufacturing techniques, is the formation of coarse primary Si particles. The main cause of this problem is the low cooling rates during conventional casting and the low solubility

of Si in Al. This is evident by studying the Al-Si phase diagram in Fig. 12. If the Al-40Si alloy is slowly cooled from the liquidus line (950 °C) down to the solidus line (577 °C), Si particles will have plenty of time to grow due to the large temperature gap present. The resulting microstructure, consisting of coarse primary Si in a eutectic matrix of eutectic Si and α-Al, seen in Fig. 13 (a), significantly reduces the thermal and mechanical properties [53, 54]. The negative effect on the mechanical strength can be directly explained by the easy initiation of cracks along the coarse Si particles.

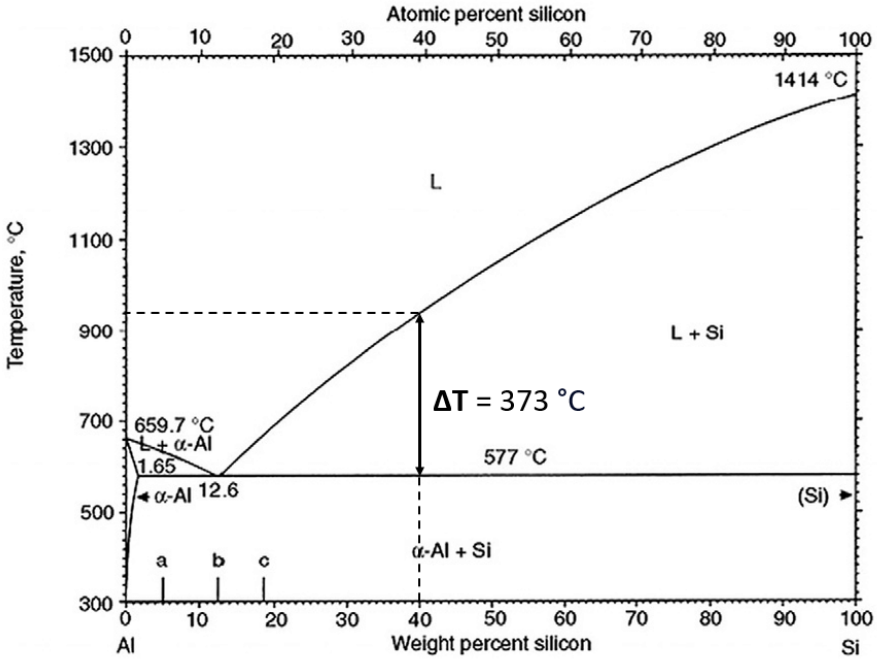

Figure 12: Al-Si phase diagram with stapled line marking the composition of 40 wt% Si and the crossing with the liquids line.

One way of sorting the problem of having a coarse Al-Si microstructure is to increase the cooling rates, by for example utilizing the SLM process. The extremely high cooling rate (10^5-10^6 K/s) present will not give sufficient time for the Si atoms to cluster and grow into large grains [55]. Instead, the Si will disperse in the matrix in smaller grains, which is beneficial for both the mechanical and thermal performance of the material [56]. The microstructure of an Al-40Si powder remelted in the SLM process is shown in Fig. 13 (b). From this micrograph, it is evident that the Si particles in the remelted powder have significantly smaller grains than the conventionally cast Al-40Si.

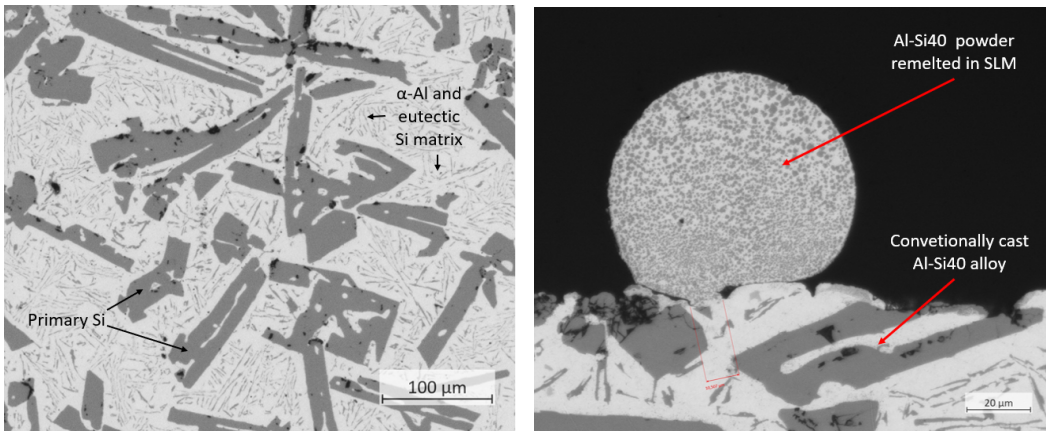

(a) (b)

Figure 13: Micrographs of (a) conventionally cast Al-40Si microstructure, and (b) Al-40Si powder remelted in the SLM process. (Note: Difference in magnification)

2.10 Wetting Angle and Wettability

To manufacture a mechanically strong and dense structure layer by layer in the SLM process, complete wetting between the melted powder and the underlying layer is necessary. The three-phase equilibrium of a liquid in contact with non-interactive solid and gaseous phases is schematically presented in Fig. 14. The equilibrium of interfacial free energies is given by:

$$\gamma_{SV} - \gamma_{SL} - \gamma_{LV} cos(\theta) = 0 \tag{10}$$

where γ_{SV}, γ_{SL}, and γ_{LV} represent the interface free energies or surface energies between the solid, liquid vapor phase, and θ represent the contact angle. It follows that the liquid phase will completely wet the surface as $cos(\theta) \rightarrow 1$, or similarly if $\gamma_{SV} - \gamma_{SL} = \gamma_{LV}$ [38]. Since the surface free energy of metal oxides is considerably lower than the liquid-vapor surface energy (γ_{LV}), liquid metals do not wet metal oxide surfaces [57]. Instead, liquid metals tend to minimize surface area by balling, as seen in Fig. 14 where $\theta > 90°$. First of all, this effect is a concern since the reduced contact area between the molten metal powder and the underlying substrate may cause bad adhesion between layers. In the worst case, the lack of adhesion will lead to either formation of pores or flaking behavior in the consolidated product. As stated in section 2.6.1, porosity within the solidified metal will create concentrations of stress, that significantly reduce the mechanical strength of the product. Poor wettability will also produce cracks in the surface that promotes corrosion and reduces the wear resistance [58]. This problem has been reported in several earlier studies. In two separate studies by Louvis et al. [39] and Olakanmi et al. [59], it was suggested that the cause of the balling phenomenon was the excessive size of the melt pool accompanied by a long liquid lifetime, meaning that too slow scanning speeds

only will produce large agglomerates with unfortunately large wetting angles. Thereby decreasing the energy density by also decreasing the laser scanning speed proved to be beneficial for the smoothness of the single scanned lines. In other words, it seems to be a narrow parameter window of correct scanning speeds that facilitates minimum balling and maximum melting of the powder.

Figure 14: Three-phase equilibrium schematic for wetting of a surface by the liquid droplet.

However, the wetting of a molten liquid on a substrate of its own kind is known as 'homologous wetting'. In this case, wetting involves simultaneous fluid flow, heat transfer to the substrate, and solidification of the powder, i.e. a non-equilibrium process. In addition, the substrate in this project does not have a perfectly smooth surface, which drastically can alter the wetting behavior [60]. Another formula describing wetting on a rough surface, as illustrated in Fig. 15, was introduced by Wenzel and is given by [61]:

$$\cos\theta_1 = R_f \cos\theta \tag{11}$$

where θ_1 is the contact angle on a rough surface, and R_f is the surface roughness coefficient. Furthermore, we can define the fixed volume condition by [62]:

$$V = \pi R_1^3 (1 - \cos\theta_1)^2 (2 + \cos\theta_1)/3 \tag{12}$$

where R_1 is the radius of the drop. The areas of the solid-liquid (S_B) and liquid-gas (S_C) interfaces are estimated by:

$$S_B(\theta_1, R_1) = \pi R_1^2 \sin^2\theta_1 \tag{13}$$

$$S_C(\theta_1, R_1) = 2\pi R_1^2 (1 - \cos\theta_1) \tag{14}$$

With these definitions, it is possible to describe the total surface energy of a liquid droplet on a rough surface, i.e. in Wenzel state by:

$$E_W = \gamma_{LV} S_C(\theta_1, R_1) + (\gamma_{SL} - \gamma_{SV}) R_f S_B(\theta_1, R_1) \tag{15}$$

As a result, the two main elements that influence the wettability on a solid surface are the surface free energy (E_W) and the surface roughness. When dealing with a rough substrate surface the solid-liquid contact area (S_B) increases. Since the fluid desire as low an energy state as possible, it reduces the surface area by increasing the contact angle (θ_1), resulting in poor wettability. This of course impacts the bonding between the molten metal and the previous layer, which gives mechanically weak structures. It is therefore even more challenging to have good wetting of the liquid metal if it is deposited on a rough surface.

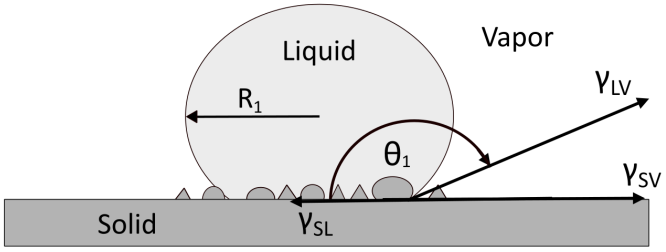

Figure 15: Wetting of droplet on a rough surface (Wenzel state).

2.11 Plateau-Rayleigh Instability and Marangoni Convection

The balling defect of a single track in the SLM process can also be explained by either Plateau-Rayleigh instability or Marangoni forces. Plateau-Rayleigh instability is the effect that causes a falling stream of fluid to break up into smaller packets with the same volume but with less surface area [63]. The driving force causing this phenomenon is the surface tension of the liquid. As mentioned in section 2.10, the liquid always seeks to minimize its energy, which can be done by minimizing the surface area. Consequently, a column of a liquid material tends to decompose into separate droplets. This effect has a close connection to the wetting of a single track described in section 2.10. The minimum time for a liquid cylinder to break up can be described by the following equation [64]:

$$t_{break} = \left\{0.3433\sqrt{\gamma_{LV}/[\rho(D/2)^3]}\right\}^{-1} \tag{16}$$

where ρ is the density of the liquid, γ_{LV} is the interface free energy between the liquid and vapor phase, and D is the diameter of the liquid cylinder. With this in hand, it is possible to observe that the break-up time, t_{break}, is proportional to the diameter of the pool, D. Thus implying that a small cylinder diameter corresponds to a short break-up time. Given that the surface free energy of Al-40Si and argon gas, γ_{LV}, is 0.821 Nm^{-1} [65], the density of the molten Al-40Si is 2.54 $\mathrm{g/cm}^3$ [66], and the diameter of the melt pool is 200 μm, it is possible to calculate the break-up time t_{break}. The break-up time would then be about 0.16 ms. This calculation is obviously just theoretical and depends on all the assumptions above being correct. Anyhow, this knowledge can be useful when looking at the relatively narrow cylindrical-shaped single tracks in the SLM process.

The Marangoni effect was first discovered on the Spacelab mission D2 in 1992 [67]. They observed that it was difficult to create a liquid bridge by putting it in contact with two liquid drops before isothermal conditions were reached [63]. Later it was imposed that a large temperature difference between a drop and a solid surface inhibits the drop to wet the surface. This phenomenon is caused by an imbalance in surface tension within the drop induced by surface temperature differences. The surface tension is a decreasing function of the temperature. A liquid with high surface tension pulls more strongly on the surrounding liquid than one with a low surface tension [68]. The flow inside a drop of molten metal sitting on a cold substrate will therefore be upward along the droplet surface in the opposite direction of the thermal gradient, as illustrated in Fig. 16. Similarly, the flow inside the drop close to the symmetry axis is directed downward toward the contact point. The tendency of the molten metal to flow upwards limits the wetting of the substrate, thus forming a sphere-shaped drop. The balling effect happens almost spontaneously after the powder has been heated enough to liquefy [61].

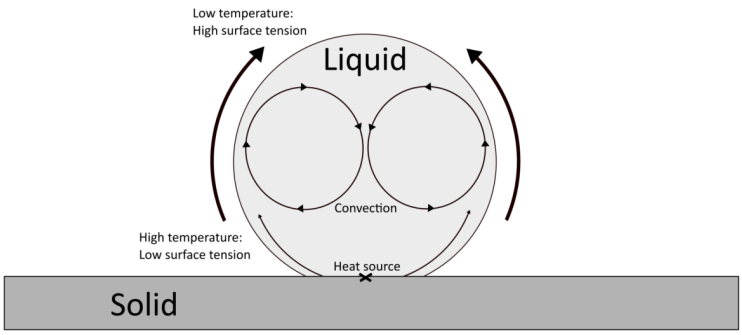

Figure 16: Schamtic drawing of the Marangoni convection flows inside a molten metal drop on a flat surface.

2.12 Equipment

The general process of how to perform SLM was in section 2.2 explained, though a great variation in the specific equipment utilized exists. Depending on the scale of the components and material input, the machinery being used can appear dramatically different. In this section, the equipment used in this study will be presented.

2.12.1 PowerLine F 30 Laser

The PowerLine F 30 is a fiber-pulsed engraving laser, which exhibits specific characteristics detailed in Table 1. These specifications serve as a reference for selecting appropriate printing parameters. For the present project, the key parameters of interest are the maximum output power ranging from 3 to 28.5 W, and its pulse frequency spanning from 30 to 100 kHz. The beam diameter measures 7.5 nm, enabling concentrated laser energy within

a considerably small region, resulting in highly precise and narrow melt pools. Notably, the laser lacks an automatic focusing system, demanding manual adjustment of the focusing point by modifying the distance between the laser head and the substrate. Accurate adjustments along the z-axis are critical to achieving the desired melting conditions for optimal outcomes.

Table 1: Specifications of the PowerLine F 30 laser head [69].

Specifications PowerLine F 30 laser head	
Laser Medium	Fiber laser
Wavelength [nm]	1055-1070
Linewidth [FWHM]	<10 nm
Output power, nominal [W]	>28.5
Minimal adjustable output power [W]	3
Pulse frequency [kHz]	30 -100
Pulse length [ns]	100 +- 20 @ 30 kHz
Power stability [min/max]	<+- 2.5 %
Pulse energy [mJ]	0.95 @ 30 kHz
M^2	<2.0
Beam diameter (collimator output) [nm]	7.5 +- 1.5
Beam roundness	>80 %
Beam divergence [mrad]	+- 0.3
Operating surrounding temperature [°C]	15 - 35
Maximum diameter of the beam ray inside the marking head [mm]	14

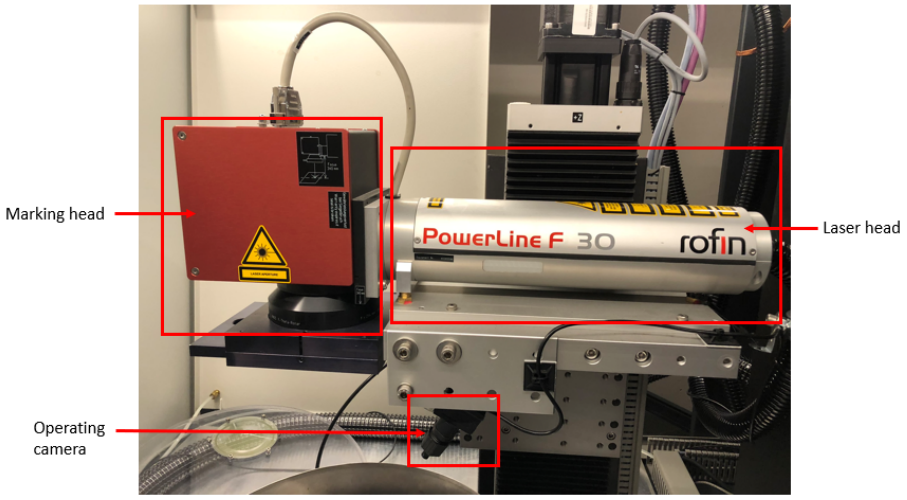

Figure 17: Picture of the PowerLine F 30 laser configuration.

2.12.2 Printing Chamber

The main objective of the printing chamber is to ensure an inert atmosphere during the SLM process. Imaged in Fig. 18, it consists of two primary components, a bottom, and a top part, respectively. The bottom part consists of a stainless steel pot with a diameter of 40 cm and a height of 9 cm. The top cylindrical part sits on top of the lower one and shares the same dimensions. To ensure a sealed system, a detachable plexiglass cover has been added to the top. The joint between the two steel parts is reinforced with tape to achieve a tight seal. Additionally, a circular glass with specific optical properties that permit the passage of laser light has been added directly over the printing bed. Argon gas is immersed into the chamber from a gas bottle connected to the bottom of the chamber. To monitor the oxygen level within the chamber while purging it with argon gas, the Rapidox 2100 oxygen detector is connected to the system. Given the higher density of argon compared to air, the detector is attached to the top of the chamber, ensuring that the oxygen level is sufficiently low before printing starts.

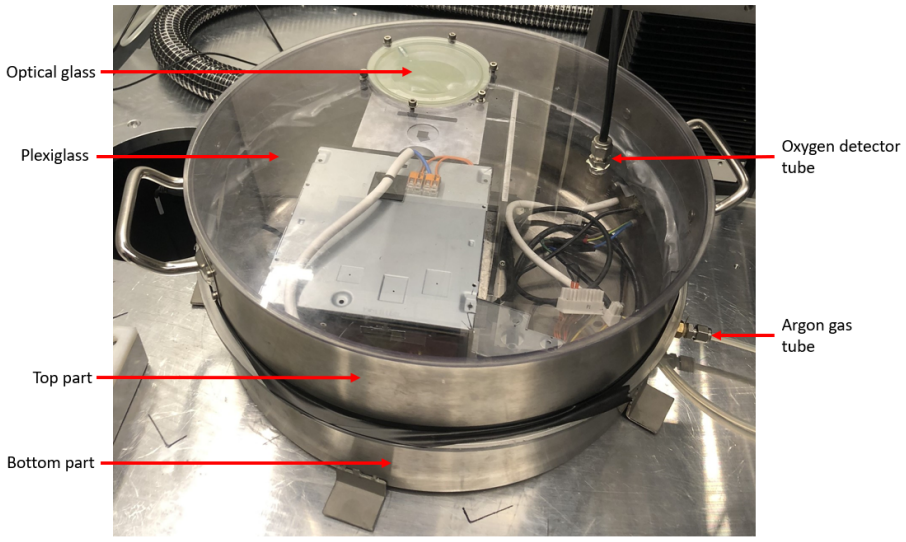

Figure 18: Picture of the printing chamber setup.

2.12.3 Powder Distribution System (PDS)

The powder distribution system (PDS) was the result of a bachelor thesis by Martini et al. [70] and was further developed in another bachelor thesis by Mostad et al. [10]. The system, depicted in Fig. 19, consists of two actuators, whereas one is meant to be a powder stage and the other a printing stage, respectively. Both stages have functionality similar to pistons and move vertically up and down, during the printing process, as described in section 2.2. The actuators can move with a minimum step size of 0.09525 μm [71], which makes them ideal for 3D printing with extremely thin layers of powder. In addition, the stages have a maximum travel range of 20 mm, which also limits the maximum height of

the 3D printed components.

The recoater moves in the horizontal direction and has the task of distributing powder from the powder stage to the printing stage. Originally, the recoater consisted of a similar system as the two other vertical actuators but malfunctioned during the Mostad et al. [10] bachelor project. Consequently, an improvised solution to this problem was introduced in the same bachelor thesis. The new actuator function uses a DVD player, replicating the horizontal movement of a recoater by triggering the eject button. A sharp steel blade is attached to the end of the DVD drive with the purpose of evenly distributing the powder. Moreover, two powder overflow collectors can be found on each side of the printing platform. This system has its advantages, but also some drawbacks, which will be discussed in more detail in the discussion section.

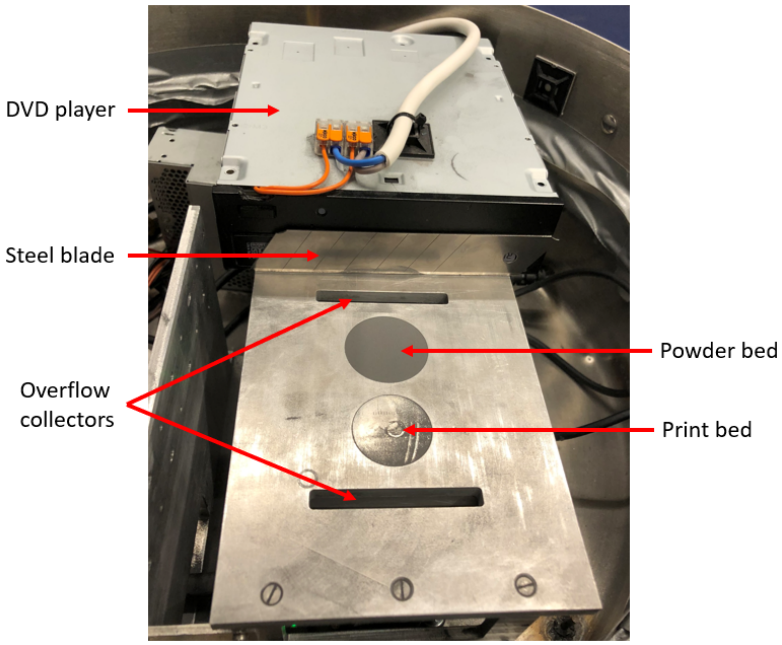

Figure 19: Picture of the powder distribution system (PDS).

3 Experimental

The experimental part is divided into four distinct sections that chronologically follow the continuous development of the parameter optimization process. Due to the concurrent testing and analysis conducted throughout the process, it posed a challenge to logically partition this section. However, to give a concise overview of the experimental work proceeding of this study, the flowchart depicted in Fig. 20 can serve as helpful guidance.

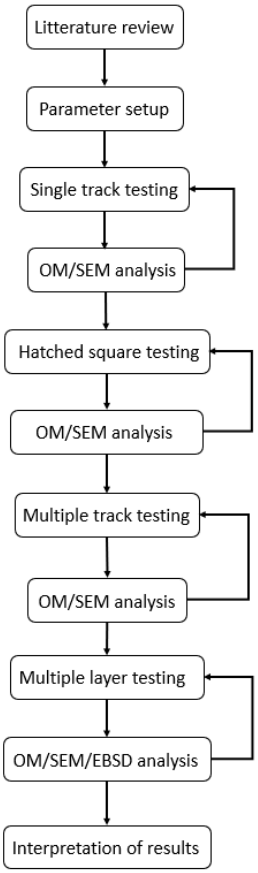

Figure 20: Flowchart of the experimental proceeding of this study. The arrows going backward represent the retesting after OM/SEM analysis that occurred if the analysis showed insufficient results.

3.1 Building Plate and Powder Substrate

The building plate used in the SLM experiments was a wedge-cast Al-Si40 substrate. The wedge casting method was specifically selected to provide a fine microstructure in the building plate, to replicate a SLM layer. Subsequent to casting the cast product was machined into 2 mm thick discs with a diameter of 30 mm, with the aim of fitting into the print bed. Also to replicate a 3D-printed surface in the single-layer tests, the Al-Si40 discs were sandblasted with very fine sand particles. The powder used in this study was a gas-atomized Al-40Si powder. The average particle size of the powder was about 40 μm.

3.2 Selection of Laser Parameters and Single Track Scanning

3.2.1 Single Track Scan Test 1

The first set of testing parameters was determined based on the knowledge obtained from the specialization project conducted in the fall of 2022. This project's primary objective was to use surface laser remelting of an Al-2.5Cu alloy to simulate the SLM printing conditions. A crucial aspect was the utilization of the same 3D-printing equipment that will also be used in this study. One of the main findings from this project was the threshold scanning speed of 75 mm/s when a 100 kHz repetition rate and 28.5 W laser power were applied. Obviously, the specialization project results are not directly in line with the aim of this project. However, the overall discoveries in terms of both methodology and specific parameter choices can be used as guidance for the first setup of parameters in this project.

To account for some of the shortcomings of the parameter tests mentioned above, a short literature review on the subject of SLM of Al-Si alloys was performed. For instance, a preliminary study on blended Al-38Si powder by Garrard et al. [5] showed that line energy below 0.150 J/mm resulted in lack-of-fusion defects and failure to melt the silicon particles completely. Jia et al. [72] processed Al-50Si from blended and pre-alloyed powder and found that blended Al-50Si achieved full density within the line energy range of 0.227-0.342 J/mm. Due to the fact that these studies lie relatively closer to Al-40Si in alloy composition than the Al-2.5Cu analyzed in the specialization project, they were weighted heavier in the preparation of the first test. With this in hand, the first set of parameters to be tested was set according to Table 2.

Table 2: Parameters in the first single track scan test, where P_{avg} (W) is the average laser power, f_{rep} (kHz) is the repetition rate, Δt (s) is the pulse period, v (mm/s) is the scanning speed, τ (s) is the pulse duration, E_p (J/mm) is the linear energy output, and P_{peak} (W) is the peak power.

No.	P_{avg} (W)	f_{rep} (kHz)	Δt (s)	v (mm/s)	τ (s)	E_p (J/mm)	P_{peak} (W)
1	28.5	100	1.00E-05	50	5.00E-06	0.57	57.00
2	28.5	100	1.00E-05	75	5.00E-06	0.38	57.00
3	28.5	100	1.00E-05	100	5.00E-06	0.29	57.00
4	28.5	100	1.00E-05	150	5.00E-06	0.19	57.00
5	28.5	100	1.00E-05	200	5.00E-06	0.14	57.00
6	28.5	30	3.33E-05	50	1.00E-07	0.57	9500.00
7	28.5	30	3.33E-05	75	1.00E-07	0.38	9500.00
8	28.5	30	3.33E-05	100	1.00E-07	0.29	9500.00
9	28.5	30	3.33E-05	150	1.00E-07	0.19	9500.00
10	28.5	30	3.33E-05	200	1.00E-07	0.14	9500.00
11	14.3	100	1.00E-05	50	5.00E-06	0.29	29.00
12	14.3	100	1.00E-05	75	5.00E-06	0.19	29.00
13	14.3	100	1.00E-05	100	5.00E-06	0.15	29.00
14	14.3	100	1.00E-05	150	5.00E-06	0.10	29.00
15	14.3	100	1.00E-05	200	5.00E-06	0.07	29.00
16	14.3	30	3.33E-05	50	1.00E-07	0.29	4833.33
17	14.3	30	3.33E-05	75	1.00E-07	0.19	4833.33
18	14.3	30	3.33E-05	100	1.00E-07	0.15	4833.33
19	14.3	30	3.33E-05	150	1.00E-07	0.10	4833.33
20	14.3	30	3.33E-05	200	1.00E-07	0.07	4833.33

The test scheme can be divided into two parts. The first 10 scans (1-10) utilize 28.5 W (100 %) laser power, and the remaining 10 scans (11-20) utilize 14.5 W (50 %) laser power. Each section of scans are again divided into portions of 100 kHz, and 30 kHz repetition rate, respectively. The scan speeds were primarily chosen to give line energy outputs in the range of 0.2-0.4 J/mm, thus varying between 50 and 200 mm/s.

The parameter test was conducted on a cast Al-Si40 disc described in section 3.1. One layer of Al-40Si powder with a thickness of about 50 µm was distributed over the disc prior to scanning. To ensure as little oxidation as possible during the printing process, the printing chamber was flushed with argon gas, until the oxygen level was below 0.01 %. The layout of the single-track scanning is illustrated in Fig. 21, where each line has an in-between spacing of 1 mm and a length of 15 mm. The spacing of the single tracks was specifically selected to ensure no interference between adjacent melt pools.

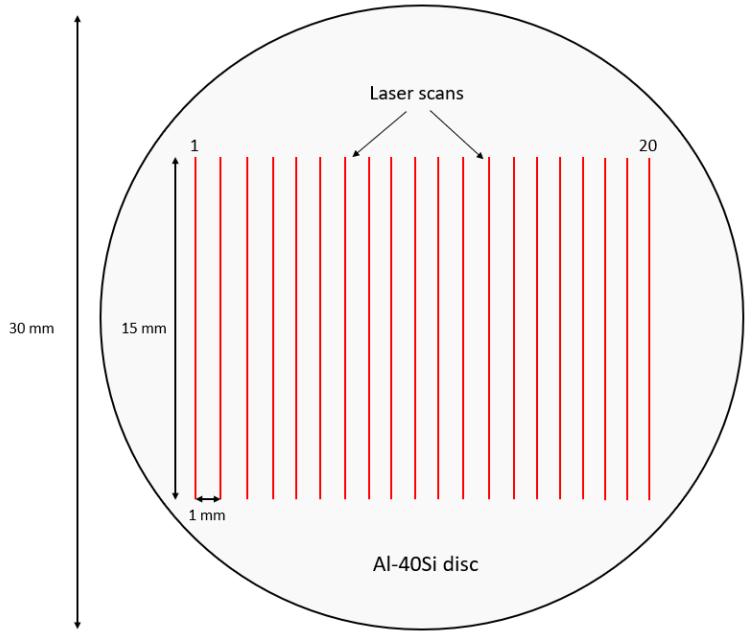

Figure 21: Layout of the single-track laser scanning test. Each scanned line has a specific set of parameters corresponding to Table 2.

3.2.2 Single Track Scan Test 2

The second test was set up in a similar manner as the first one but with some adjustments based on the OM analysis from Test 1 in section 3.2.1. To improve adhesion between the Al-40Si disc and the remelted powder, the scan speeds were lowered ranging from 100 to 55 mm/s for the 30 kHz scans, and 70 to 25 mm/s for the 100 kHz scans. The laser parameters are presented in Table 3. By keeping the surrounding conditions, like the oxygen level somewhat the same, it was easier to compare the results from tests 1 and 2.

Table 3: Laser parameters for the second test, where P_{avg} (W) is the average laser power, f_{rep} (kHz) is the repetition rate, Δt (s) is the pulse period, v (mm/s) is the scanning speed, τ (s) is the pulse duration, E_p (J/mm) is the linear energy output, and P_{peak} (W) is the peak power.

No.	P_{avg} (W)	f_{rep} (kHz)	Δt (s)	v (mm/s)	τ (s)	E_p (J/mm)	P_{peak} (W)
1	28.5	30	3.33E-05	55	1.00E-07	0.52	9500.00
2	28.5	30	3.33E-05	60	1.00E-07	0.48	9500.00
3	28.5	30	3.33E-05	65	1.00E-07	0.44	9500.00
4	28.5	30	3.33E-05	70	1.00E-07	0.41	9500.00
5	28.5	30	3.33E-05	75	1.00E-07	0.38	9500.00
6	28.5	30	3.33E-05	80	1.00E-07	0.36	9500.00
7	28.5	30	3.33E-05	85	1.00E-07	0.34	9500.00
8	28.5	30	3.33E-05	90	1.00E-07	0.32	9500.00
9	28.5	30	3.33E-05	95	1.00E-07	0.30	9500.00
10	28.5	30	3.33E-05	100	1.00E-07	0.29	9500.00
11	28.5	100	1.00E-05	25	5.00E-06	1.14	57.00
12	28.5	100	1.00E-05	30	5.00E-06	0.95	57.00
13	28.5	100	1.00E-05	35	5.00E-06	0.81	57.00
14	28.5	100	1.00E-05	40	5.00E-06	0.71	57.00
15	28.5	100	1.00E-05	45	5.00E-06	0.63	57.00
16	28.5	100	1.00E-05	50	5.00E-06	0.57	57.00
17	28.5	100	1.00E-05	55	5.00E-06	0.52	57.00
18	28.5	100	1.00E-05	60	5.00E-06	0.48	57.00
19	28.5	100	1.00E-05	65	5.00E-06	0.44	57.00
20	28.5	100	1.00E-05	70	5.00E-06	0.41	57.00

3.2.3 Single Track Scan Test 3

The main learning point from the previous test was to lower the scanning speeds even more and to employ the maximum repetition rate (100 kHz). Suspecting that the laser pulses may have an explosive effect on the powder, causing it to uncontrollably evaporate or scatter around, laser powers at 21,4 W (75 %) and 14,3 W (50 %) were experimented with. Also, the single scans with 0,950 and 0,814 J/mm linear energy gave the most promising results in the previous test. Therefore, a scheme of similar linear energies, but lower scan speeds were tested from scan number 7 to 10. The resulting laser parameter testing scheme is shown in Table 4. Only 15 single-track scans were performed in this test, making room for more advanced testing such as multiple scans. This will be presented in the next section.

Table 4: Laser parameters for the third test, where P_{avg} (W) is the average laser power, f_{rep} (kHz) is the repetition rate, Δt (s) is the pulse period, v (mm/s) is the scanning speed, τ (s) is the pulse duration, E_p (J/mm) is the linear energy output, and P_{peak} (W) is the peak power.

No.	P_{avg} (W)	f_{rep} (kHz)	Δt (s)	v (mm/s)	τ (s)	E_p (J/mm)	P_{peak} (W)
1	28.5	100	1.0E-05	1	5.0E-06	28.50	57.00
2	28.5	100	1.0E-05	2	5.0E-06	14.25	57.00
3	28.5	100	1.0E-05	4	5.0E-06	7.13	57.00
4	28.5	100	1.0E-05	6	5.0E-06	4.75	57.00
5	28.5	100	1.0E-05	8	5.0E-06	3.56	57.00
6	28.5	100	1.0E-05	10	5.0E-06	2.85	57.00
7	28.5	100	1.0E-05	15	5.0E-06	1.90	57.00
8	28.5	100	1.0E-05	20	5.0E-06	1.43	57.00
9	28.5	100	1.0E-05	25	5.0E-06	1.14	57.00
10	28.5	100	1.0E-05	30	5.0E-06	0.95	57.00
11	28.5	100	1.0E-05	35	5.0E-06	0.81	57.00
12	21.4	100	1.0E-05	26	5.0E-06	0.82	42.75
13	21.4	100	1.0E-05	20	5.0E-05	1.07	42.75
14	14.3	100	1.0E-05	18	5.0E-06	0.79	28.50
15	14.3	100	1.0E-05	15	5.0E-06	0.95	28.50

3.3 Multiple Track Scanning

The initial single track is an effective and simple way of finding the correct range of laser parameters to use in more advanced testing. However, a set of hatched lines was tested to see the effect of the laser parameters when multiple scans are added close together. Only the most promising parameters from the single-track scanning were carried out in this part of the study. The multiple scans were utilized simultaneously as the single-track scans, maximizing the use of the Al-40Si disc's surface area. In addition, this setup will spare time as the single scan parameter testing is narrowed down to only test 10 parameters in each experiment. The layout of the laser scanning scheme is shown in Fig. 22.

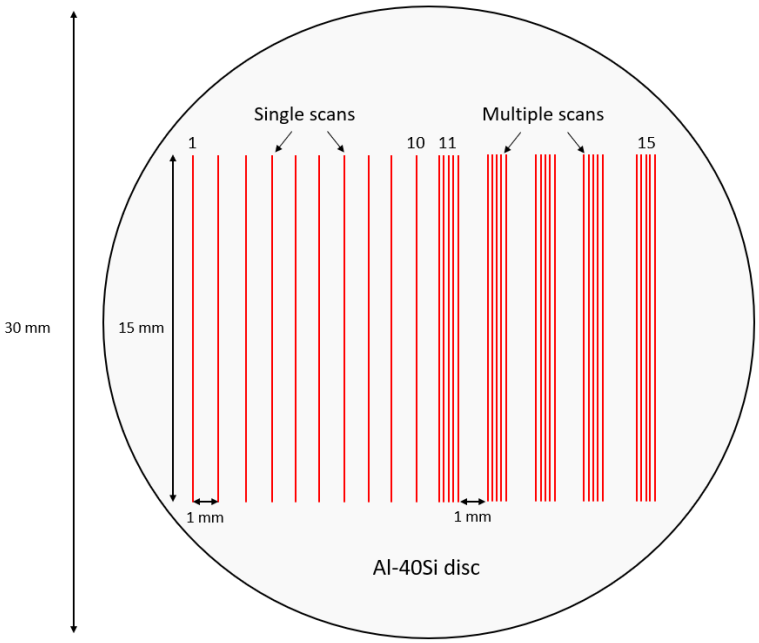

Figure 22: Layout of the single-track combined with multiple scanning laser scanning test.

Each set of the multiple scanned lines consisted of 5 single scans arranged close together. The hatching distance, i.e. the distance between scans, was varied between 0.1 mm and 0.05 mm. This particular hatching was determined based on the thickness of the single track lines analyzed in OM and SEM. Similar to the single scans, a distance of 1 mm was set between each group of multiple scans, avoiding interference among the scanned lines. Similar to the single-scan tests, one single layer with a thickness of about 50 μm was added to the building platform before scanning.

Table 5: Parameters tested for the multiple scanned lines, where P_{avg} (W) is the average laser power, f_{rep} (kHz) is the repetition rate, Δt (s) is the pulse period, v (mm/s) is the scanning speed, τ (s) is the pulse duration, E_p (J/mm) is the linear energy output, and d is the hatching distance.

No.	P_{avg} (W)	f_{rep} (kHz)	Δt (s)	v (mm/s)	τ (s)	E_p (J/mm)	d (mm)
1	28.5	100	1.00E-05	1	5.00E-06	28.50	0.10
2	28.5	100	1.00E-05	2	5.00E-06	14.25	0.10
3	28.5	100	1.00E-05	4	5.00E-06	7.13	0.05
4	28.5	100	1.00E-05	6	5.00E-06	4.75	0.05
5	28.5	100	1.00E-05	8	5.00E-06	3.56	0.05
6	28.5	100	1.00E-05	30	5.00E-06	0.95	0.10
7	28.5	100	1.00E-05	25	5.00E-06	1.14	0.10
8	28.5	100	1.00E-05	30	5.00E-06	0.95	0.05
9	28.5	100	1.00E-05	25	5.00E-06	1.14	0.05

3.4 Hatched Square Scanning

The next step in the process was to look at hatching and particularly how the hatching parameters influence the printing results. Therefore, a set of 9 hatched squares with the dimensions of 4x4 mm was added to the VLM software, as illustrated in Fig. 23. Only one layer with a thickness of about 50 μm was added to the building plate before scanning. The hatching followed a bidirectional pattern, i.e. the lines were executed alternately in both directions. Each square was also finished with an outline contour scan. With the experience from the multiple track scanning, the hatching overlap was set to 20 %. The laser parameter scheme is shown in Table 6 and was selected based on the previous parameter tests.

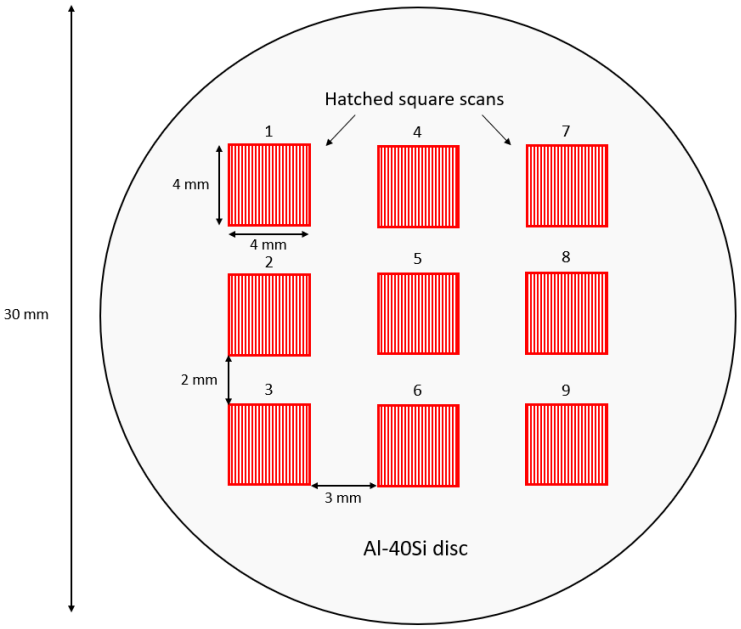

Figure 23: Layout of the hatched squares scanning test.

Table 6: Parameters tested for the hatched square scanning, where P_{avg} (W) is the average laser power, f_{rep} (kHz) is the repetition rate, Δt (s) is the pulse period, v (mm/s) is the scanning speed, τ (s) is the pulse duration, and E_p (J/mm) is the linear energy output. The overlap represents the percentage of overlap between scans.

No.	P_{avg} (W)	f_{rep} (kHz)	Δt (s)	v (mm/s)	τ (s)	E_p (J/mm)	Overlap (%)
1	28.5	100	1.00E-05	2	5.00E-06	14.25	20
2	28.5	100	1.00E-05	5	5.00E-06	5.70	20
3	28.5	100	1.00E-05	10	5.00E-06	2.85	20
4	28.5	100	1.00E-05	15	5.00E-06	1.90	20
5	28.5	100	1.00E-05	20	5.00E-06	1.43	20
6	28.5	100	1.00E-05	25	5.00E-06	1.14	20
7	28.5	100	1.00E-05	30	5.00E-06	0.95	20
8	28.5	100	1.00E-05	35	5.00E-06	0.81	20
9	28.5	100	1.00E-05	40	5.00E-06	0.71	20

3.4.1 Preheating of Building Platform

The parameter scheme presented above in Table 6 in section 3.4 was also utilized with preheating of the building platform. To find the effect of preheating on single-track scanning, one low and one high-temperature preheating scheme was carried out. The low-temperature preheating test was done by scanning the building plate with a scanning speed of 5 mm/s and 0 % hatch overlapping until the total surface area to be built on was completely heated. The high-temperature preheating test was also carried out with a laser scanning speed of 5 mm/s, but additionally, a scan with 2 mm/s was performed directly after the first scan ended. Consequently, reaching a higher temperature in the building plate. Since no thermocouple or other measuring devices were fixed to the building plate, it was not possible to get the exact temperature reached in this phase. However, the primary objective of this part of the study was only to find the general effect of preheating with the use of an Al-40Si alloy in this particular SLM process. At the same time, by studying the surface exposed to preheating in an electron microscope it was possible to observe substantial remelting of the surface material. Considering the melting point of the Al-40Si alloy is about 950 °C, this can say something of the temperatures reached in the surface layer. However, as mentioned earlier in this study, the Al-40Si alloy has a significantly good conducting ability which will lead a lot of the heat away quickly. This will of course limit the heating of the building plate.

3.4.2 Rescanning

Previous studies have, as mentioned in the theory section 2.7.2, proven that rescanning the same layer one or more times can improve the printing result. It was therefore attempted to rescan the already irradiated layer a second time with 50 % (14.25 W) laser power. The same VLM parameter setup as described in section 3.4 was reused for this test, i.e. a hatching overlap of 20 % was applied.

3.4.3 Multiple Layer Printing

Printing of multiple layers was conducted by gradually increasing the number of layers. Firstly, a test with the same setup as in Fig. 23 in section 3.4, but with two layers of powder was performed. All other conditions, like oxygen level (< 0.01 %) and layer thickness (50 μm) were kept constant. The final parameter test in this study was carried out with 4 layers of powder.

3.5 Preparation of Samples

Two main preparation techniques were performed after the SLM part of the experimental study. The first method involved cutting the Al-40Si building plate in half perpendicular to the single tracks with the Struers Accutom 5 fine-cutting machine. This preparation was carried out on the single-track scanned samples, presented in Fig. 24 (a).

The second method was developed to enable cross-section analysis of multiple-layer printed samples. Instead of cutting the sample, the 4x4 mm printed sample was mounted in a supporting clip. This way, the thin 3D-printed sample was able to stay upright as it was cast in epoxy. To expose the cross-section, the sample was ground with coarse #800 SiC paper until the center of the sample was reached. The resulting sample is presented in Fig. 24 (b).

Regardless of the approach to cutting and epoxy casting, the samples were further ground and polished to facilitate for OM and SEM analysis. The samples were ground and polished with the Struers TegraPol 31 semi-automatic grinding and polishing machine in the following order:

- Grinding: #800 - #1200 - #2000 - #4000 (Water as lubricant)
- Polishing: Mol 3 μm - Nap 1 μm (DiaPro solution as lubricant)

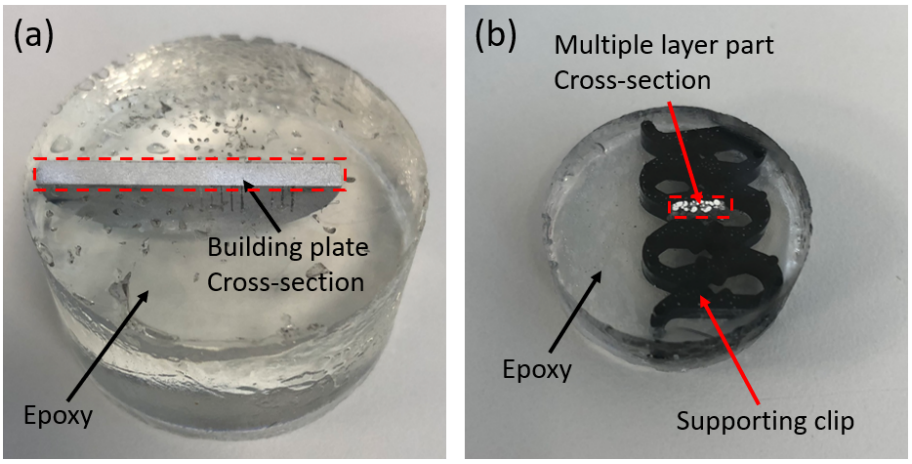

Figure 24: Two examples of laser scanned samples cut in half and cast in epoxy. (a) Cross-section of a building plate with single-track scans, and (b) Cross-section of a multiple-layer printed sample.

3.6 Materials Characterization

3.6.1 OM Analysis

Analysis in OM and SEM were as mentioned continuously used in the development of the experimental part of the study. Subsequent to all of the experiments one or the other of the microscopes was used to get a better understanding of the effect of the laser parameters on the Al-40Si alloy. The OM analysis was performed with the Zeiss Axio Vert.A1 Inverted light microscope, with the bright field mode configuration. To gain an overview of the sample, and be able to locate each single-track cross-section, the stitching tool implemented in the Zen Core software was used. This function makes it possible to create a high-resolution panorama image of the whole length of the surface, presented in Appendix B. By then measuring and comparing the panorama image with the VLM software scanning pattern layout, it is possible to locate each individual single track.

3.6.2 SEM Analysis

The SEM analysis was conducted with the Zeiss ULTRA 55 SEM and the Zeiss Supra 55VP SEM. The configurations used in the SEM depended on the sample type being used, namely a cross-section sample or a surface sample. The specific parameters being used are presented in Table 7. As Table 7 shows, the secondary electrons (SE) and backscattered electrons (BSE) modes were utilized for the cross-section samples. Because of the z-contrast, the BSE mode offers the possibility to observe different phases in the sample. When studying the surface of the sample the SE mode was applied. The benefit of utilizing this method is that it offers a great depth of field and the possibility to look at longer

sections of the single tracks. Conversely, it is difficult to say anything about the continuity of the single tracks by just looking at one cross-section. This flaw in methodology was unfortunately discovered after the first test, after which the SEM characterization was implemented in all of the following optimization work.

Table 7: SEM configurations depending on the two general sample types in this study, cross-section, and surface, where SE stands for secondary electrons, and BSE stands for backscattered electrons.

Sample Type	Mode	Accelerating Voltage (kV)	Working Distance (mm)	Aperture (μm)
Cross-section	SE/BSE	15-20	10-12	60
Surface	SE	10-20	10-20	60

3.6.3 ImageJ Analysis

The micrographs acquired from OM and SEM were also analyzed with the ImageJ software. This software enables post-image treatment, such as measuring the single track widths and average grain size. ImageJ was especially useful when measuring the average droplet sizes of the single tracks and hatched square scans. To obtain representative results, 5 individual measurements of every single track/hatched square were carried out. From these measurements, the average single track width was calculated, in addition to the standard deviation.

4 Results

4.1 Single Track Scanning

4.1.1 Single Track Scan Test 1

The purpose of the first single-track test was to try out a wide specter of the laser's possible parameters, as presented in Table 2, thus having large variations in the laser power (50 - 100 %), the repetition rate (30 - 100 kHz), and the scan speed (50 - 200 mm/s). After preparation of the sample, only two of the scanned tracks showed adhesion to the substrate. The cross-sections of these two tracks are presented in Fig. 25 (a) and (b). The scan in (a) was done with a 50 mm/s scan speed and laser repetition rate of 30 kHz, while the scan in (b) was carried out with a 75 mm/s scan speed and a 100 kHz repetition rate. When studying these single tracks, there are little signs of melt pool formation in the underlying substrate. The remelted droplets of Al-40Si powder also show a very small contact area with the cast Al-40Si building plate. Despite having a diameter of about 80 μm, the point

of contact for the droplet in Fig. 25 (b) only measures 10.5 μm. This is also the case for the droplet presented in Fig. 25 (a). Both scans have a spherical shape, suggesting that balling has occurred in the SLM process. A clear difference between the two scans is also the relatively large size difference, where (a) has a diameter of 18.3 μm, and (b) 80 μm.

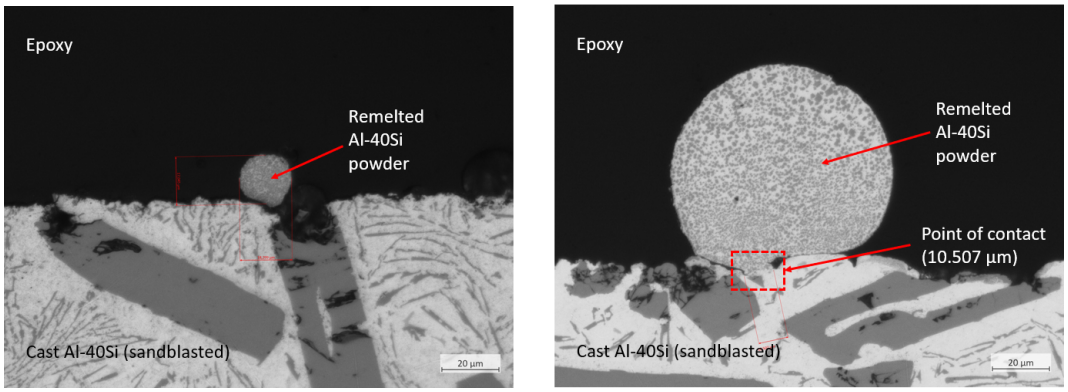

(a) (b)

Figure 25: OM images of the cross-section of the remelted powder from single scan test 1. (a) 50 mm/s scan speed and 100 kHz repetition rate, and (b) 75 mm/s scan speed and 30 kHz repetition rate.

4.1.2 Single Track Scan Test 2

With the knowledge from the first tests, the parameters were set according to the single track that showed adhesion to the building plate as a basis. The purpose was also to see the effect of varying the repetition rate (f_{rep}) between the minimum (30 kHz) and maximum (100 kHz). Subsequent to the preparation of the samples by cutting, casting in epoxy, grinding, and polishing, the sample was analyzed with OM. The OM analysis is presented in Fig. 26, where only single scans with 100 kHz are shown. The reason for this is that the single scans with a 30 kHz repetition rate did not adhere to the building plate, whereas most of the scans with 100 kHz did. In line with single scan test 1, the remelted powder droplets show in general a small degree of wetting to the building plate. The single-track scan with 30 mm/s scan speed in Fig. 26 (b) is the only scan that seems to have wetted the underlying surface. The droplet in Fig. 26 (c) has a similar shape as the droplet in 25 (b), sharing similar laser parameters. However, the dissimilarity in size between the two is apparent with a diameter difference of roughly 70 μm.

The two single tracks with a scan speed of 55 mm/s and 70 mm/s (Fig. 26 (d) and (e)), respectively, share a relatively similar shape. Both seem to consist of two separate droplets on top of each other melted together. A clear distinction in grain size is visible for the two droplets highlighted in separate colors. In Fig. 26 (d) the grains inside droplet 1 close to the cast Al-40Si surface are generally smaller compared to the rest of the droplet. This effect can also be found in droplet 2 close to the droplet 1/droplet 2 interface. In all the

powders, a high density of fine primary Si particles can be observed.

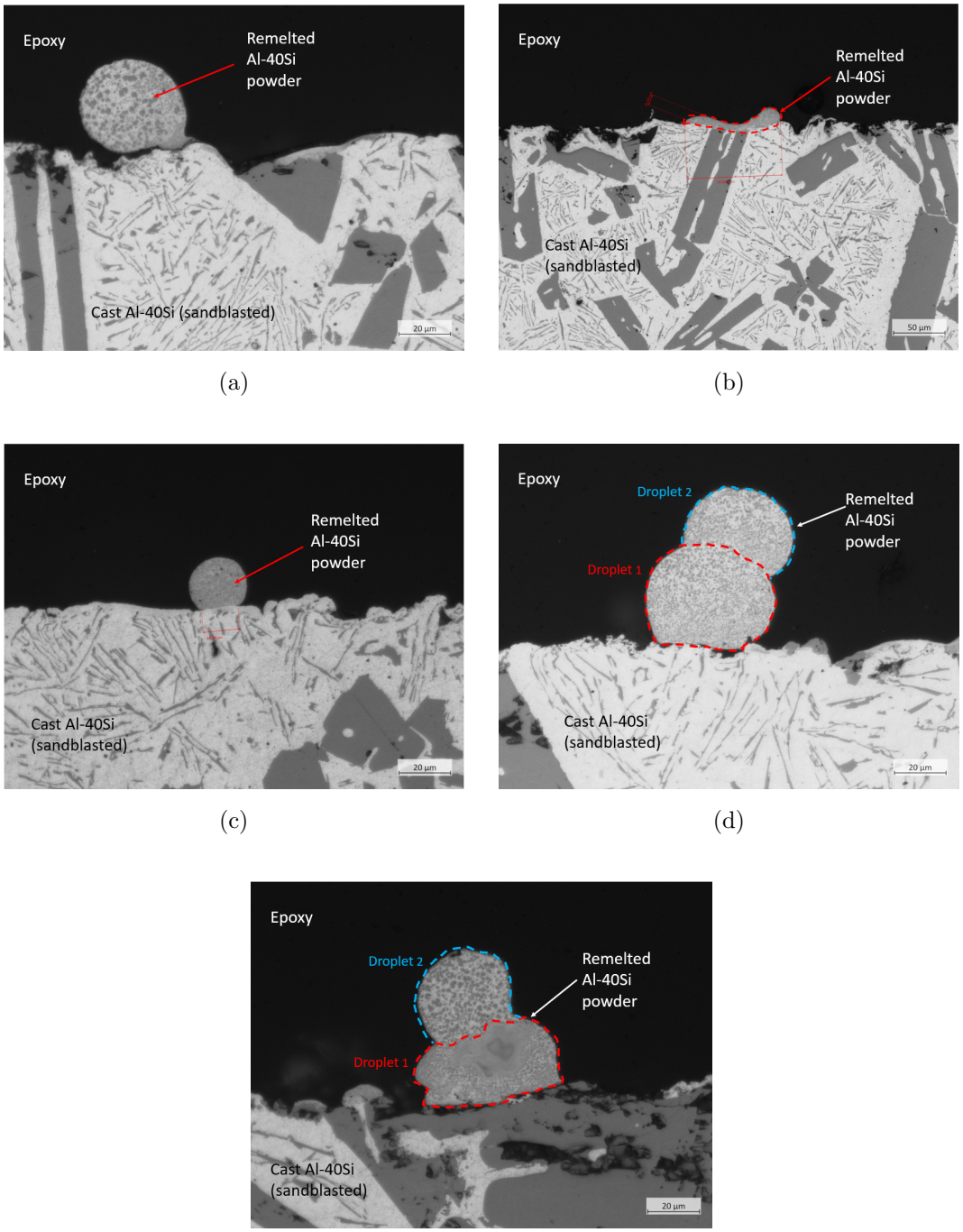

Figure 26: OM images of the cross-section from single track scan test 2. All scans at 100 kHz repetition rate (f_{rep}) and scan speeds (v) of (a) 30 mm/s, (b) 35 mm/s, (c) 50 mm/s, (d) 55 mm/s, and (e) 70 mm/s. (Note: Difference in magnification)

The cross-section view presented above is a great way of characterizing the microstructure inside the remleted powders for the test of single tracks, yet this approach has its limits to show the continuity of tracks. To better gain an overview of how the single tracks appear

in their full length, a SEM surface view is presented in Fig. 27 and 28. Fig. 27 displays the difference in morphology of the single tracks when varying the repetition rate between 30 kHz in (a) and 100 kHz in (b). It is also apparent that the droplet size increase as the scan speed decrease in both (a) and (b), respectively. The scans with a 100 kHz repetition rate in (b) seem to have produced larger droplets, than the scans with a 30 kHz repetition rate in (a).

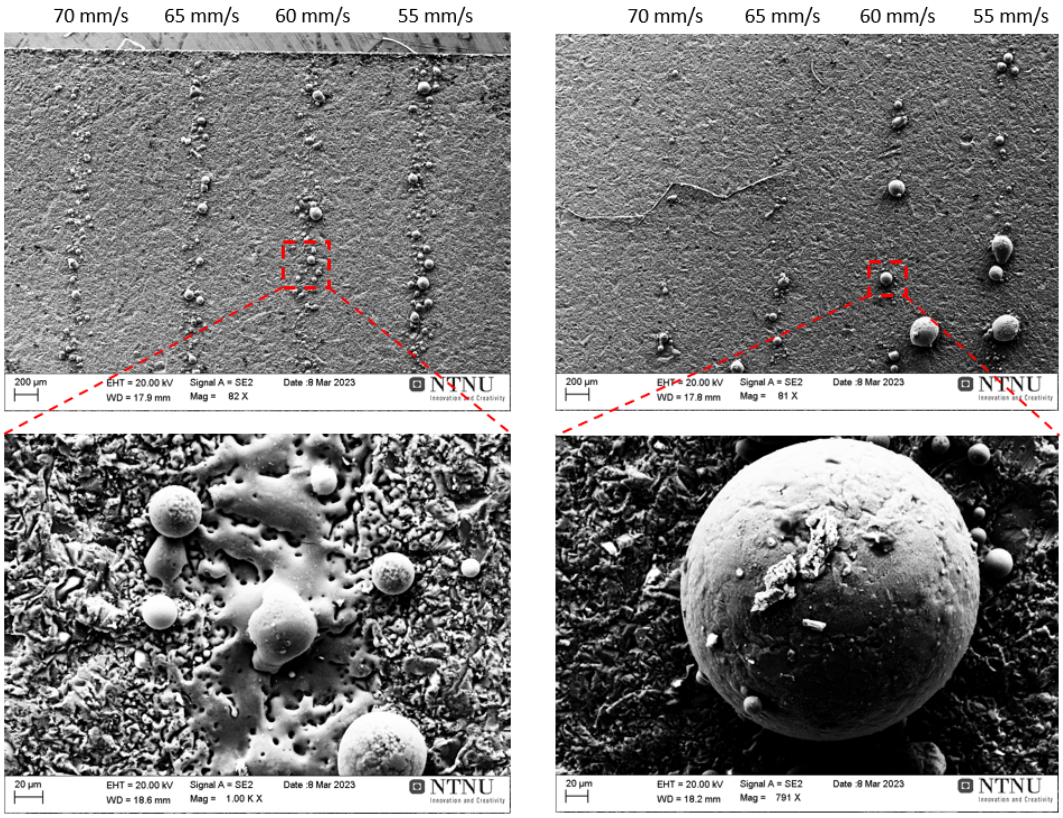

(a) (b)

Figure 27: SEM images of the building plate surface with scanned single tracks of the same scan speed (70-55 mm/s), but different repetition rate. (a) 30 kHz repetition rate, and (b) 100 kHz repetition rate.

The single-track scans imaged in Fig. 28 show the effect of decreasing the scan speed to under 50 mm/s. The droplets formed on the surface are much larger than the droplets already discussed in Fig. 27. However, there is still no sign of continuous single tracks.

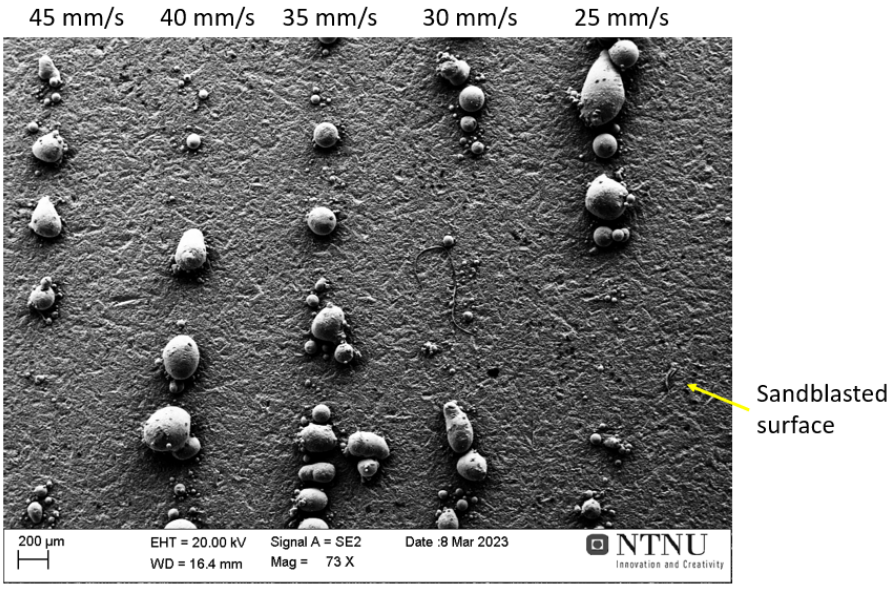

Figure 28: SEM image of the building plate surface with scanned single tracks from 45 mm/s to 25 mm/s scan speed and 100 kHz repetition rate.

4.1.3 Single Track Scan Test 3

In this experiment, the scan speed was set below the previous experiment, i.e. lower than 35 mm/s. This gave better remelting of the Al-40Si powder, but still, the balling phenomenon was present. When barely touching the scanned lines with the tip of a finger, most of the remelted power fell off. The single tracks with scan speeds from 10 mm/s to 35 mm/s are imaged in Fig. 29, where the scan speeds increase from left to right with a 5 mm/s increment.

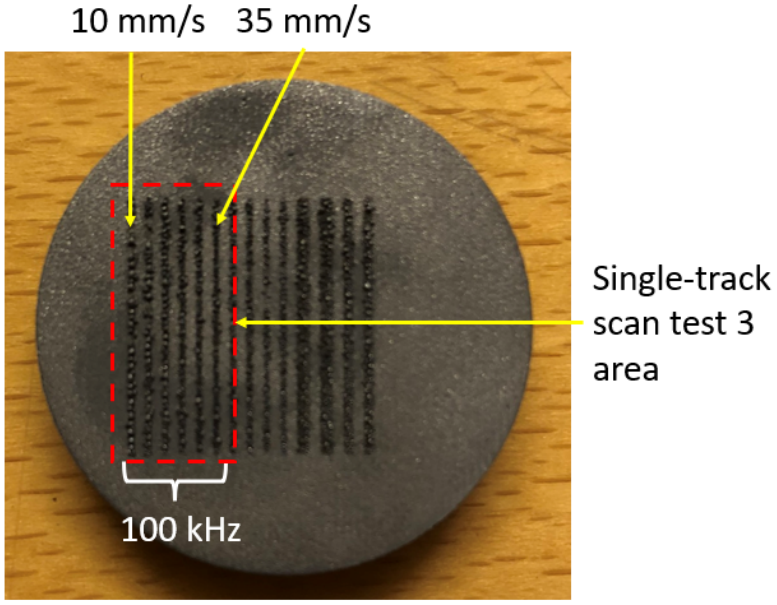

Figure 29: Picture of the single track scan test 3. The area of interest is within the dotted red line. The scans were conducted at scan speeds from 10 to 35 mm/s with a 5 mm/s increment, and 100 kHz repetition rate.

The laser parameter test with scan speeds from 1 mm/s to 20 mm/s, is presented in Fig. 30 (a) and (b). Despite the presence of balling, these single scans show a more continuous character than the scans at higher scan speeds presented above.

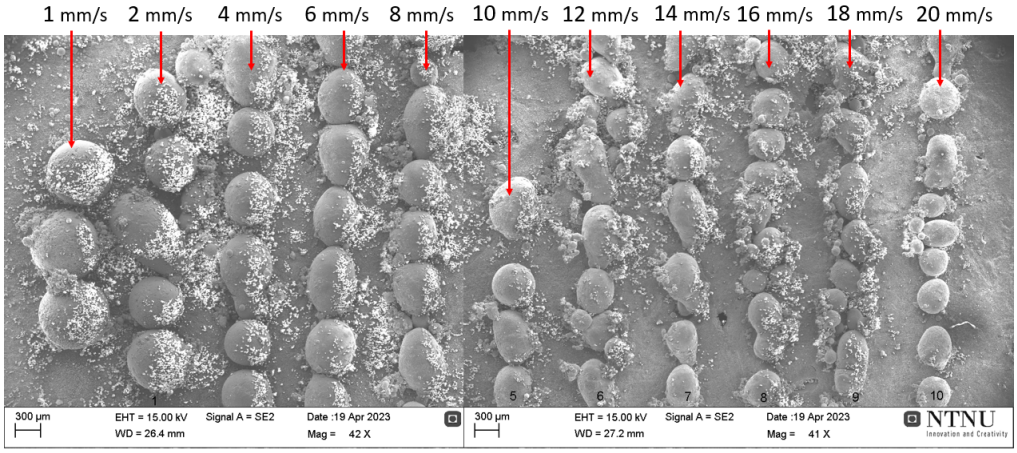

Figure 30: Two SEM images stitched together showing the single track scans with scan speeds from 1 to 20 mm/s and 100 kHz repetition rate.

A summary of the average droplet size as a function of scan speed for the single-track scans is illustrated in Fig. 31, showing a general trend that the droplet size decreases with scanning speed. SEM images of a selection of the data points are also shown in the same figure. The graph in Fig. 32 illustrates the adhesion of the droplets compared to the scan speed and linear energy for each of the single scan parameter tests. It shows that a lower

scan speed in combination with larger linear energy promotes the adhesion between the remelted powder and the building plate.

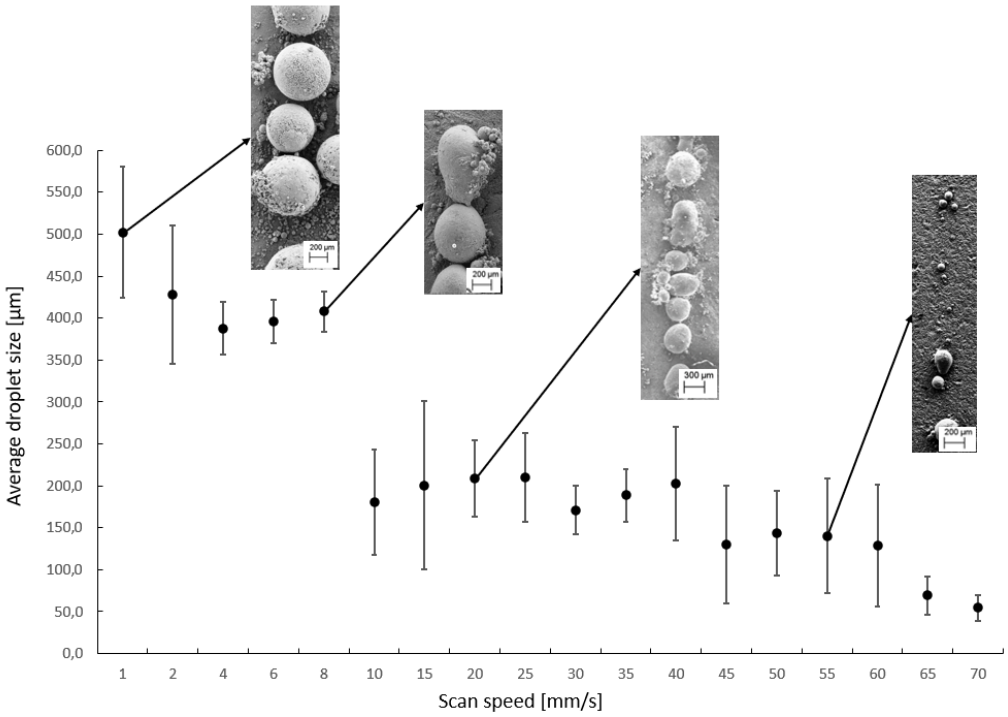

Figure 31: Scan speed as a function of remelted droplet average size (diameter) for the single-track scans, with SEM images for a selection of the data points.

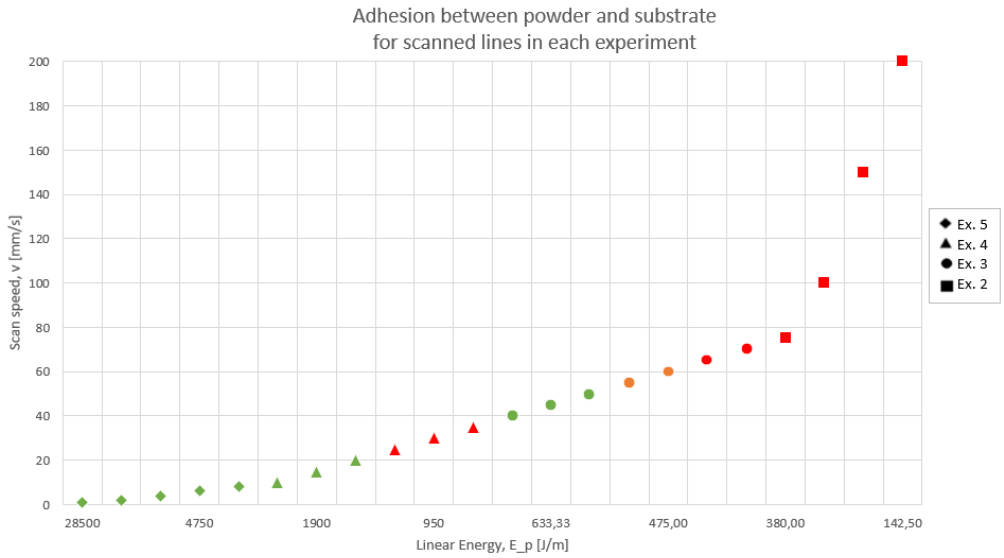

Figure 32: Graph representing the adhesion between the remelted powder and the building plate for each single-track scanned line. Green = adhesion, Orange = partial adhesion, red = no adhesion. (Note: Inverse linear energy x-axis)

4.2 Multiple Track Scanning

The multiple-track scanning test is presented in Fig. 33 (a) and (b), where the multiple scan area is marked in red. From the image in Fig. 33 (b), it is possible to observe a difference in the droplet size between the single scans (yellow) and the hatched scans (red). However, a closer view of the multiple scans is presented in Fig. 34. From this SEM image, one can notice that a line of larger remelted droplets has formed instead of the formation of several small single tracks. The largest droplet from the scans has diameters of 579.5 μm (2 mm/s), 593.0 μm (4 mm/s), 535.3 μm (6 mm/s), and 516.0 μm (8 mm/s), respectively.

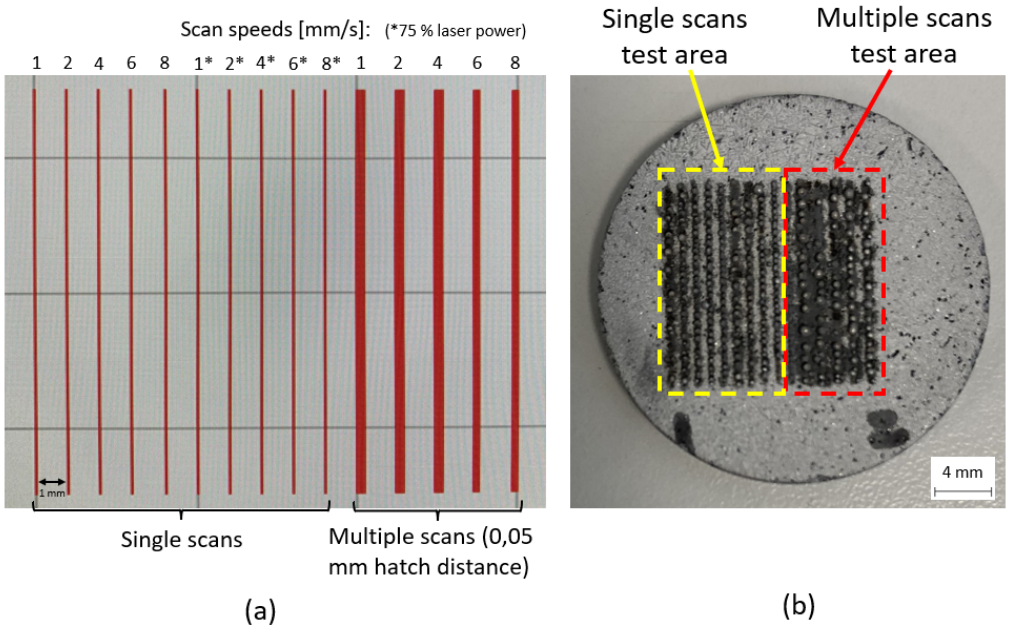

Figure 33: (a) VLM software input before multiple track scan test and (b) laser scanned disc. The two distinctive test areas are marked yellow (single scans) and red (multiple scans).

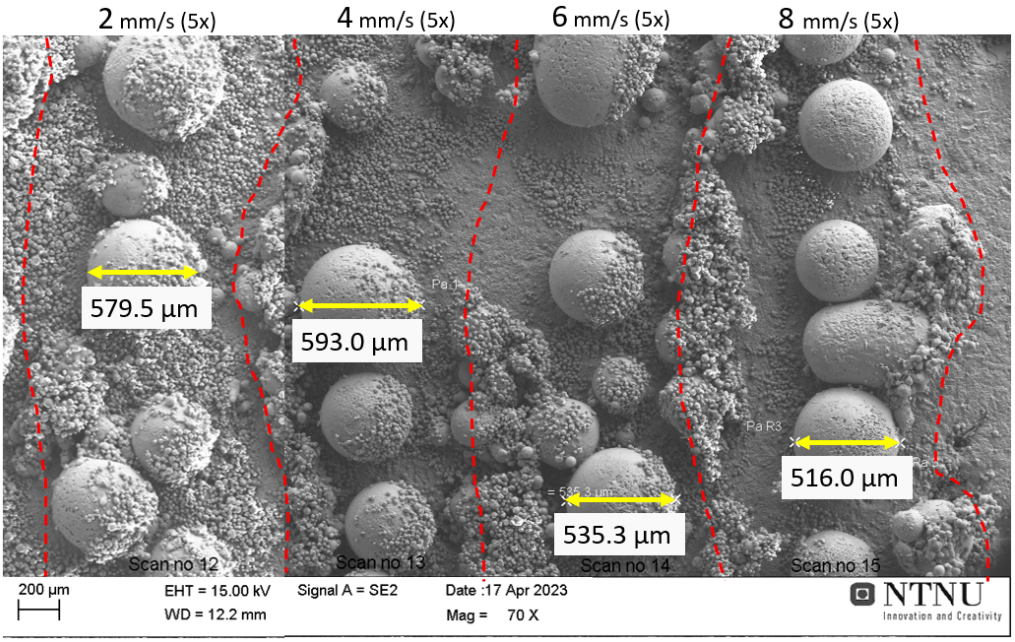

Figure 34: SEM image of the multiple tracks with 0.05 mm hatching distance and scan speeds from 2 mm/s to 8 mm/s. The diameter of the largest remelted droplet for each scan is also measured.

4.3 Hatched Square Scanning

The VLM software input and the resulting laser scanned disc are presented in Fig. 35 (a) and (b). As the VLM layout in (a) shows, the hatching overlap was set to 20 %, and scan speeds were set from 2 mm/s to 40 mm/s. The laser-scanned disc in (b) displays the decreasing droplet size with increasing scan speed.

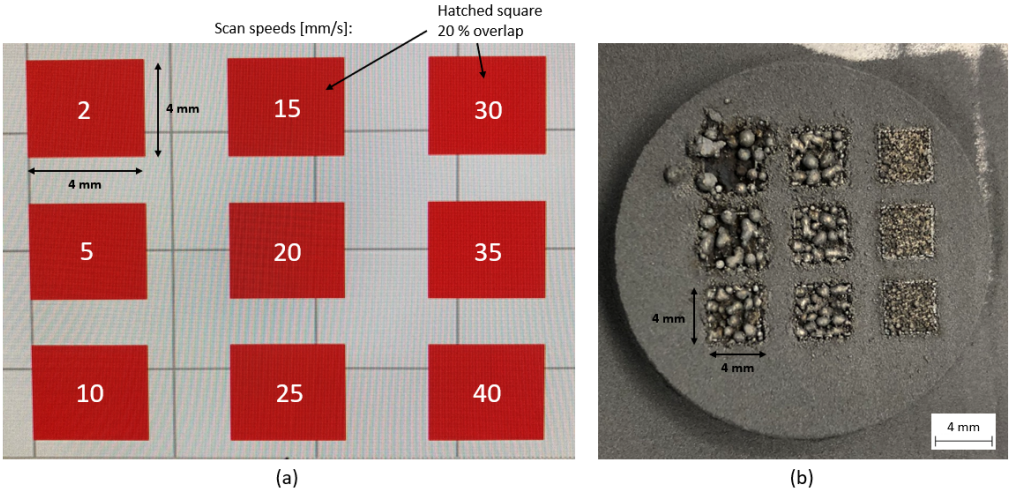

Figure 35: (a) VLM software layout with the specific scan speeds inside each square, and (b) resulting laser scanned disc.

The SEM images in Fig. 36 gives a closer look at the hatched square scans. To illustrate the evolution of average droplet size with scan speed for the hatched square scans, the graph in Fig. 37 can be helpful. The average droplet sizes were calculated by measuring 5 of the longest continuous droplets in ImageJ. Combined with some of the data points are the corresponding SEM images used in the calculations. It shows that a lower scan speed facilitates the joining of droplets, thereby forming larger droplets.

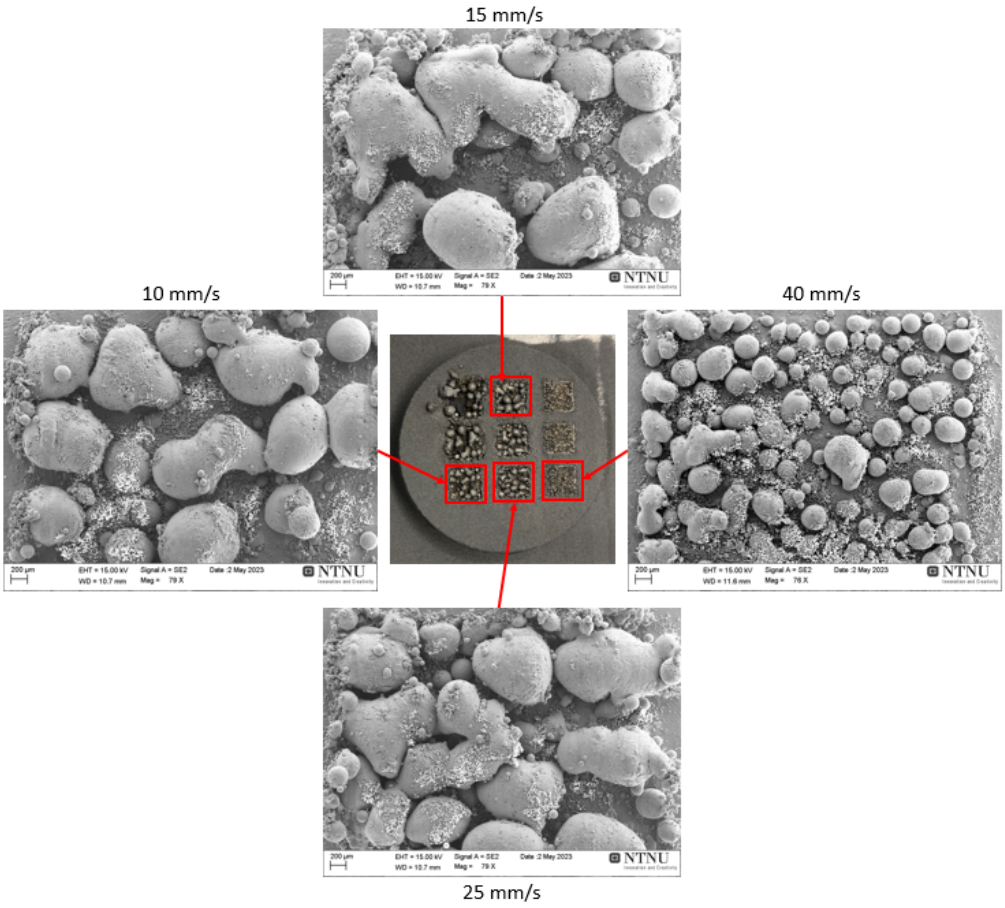

Figure 36: Selection of SEM images from hatched square scan test with 20 % hatching overlap and scan speeds of 10 mm/s, 15 mm/s, 25 mm/s, and 40 mm/s. Conducted at 28.5 W laser power and 100 kHz repetition rate.

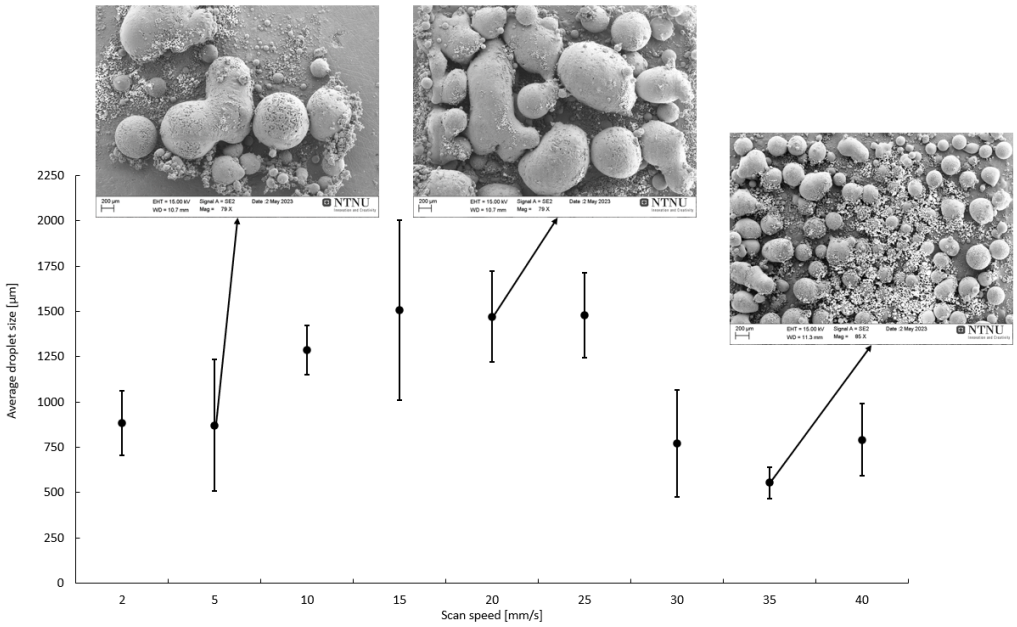

Figure 37: Scan speed as a function of the average size of the longest continuous droplets for hatched square scans, with corresponding SEM images for a selection of the data points.

4.4 Multiple Layer Printing

The printing results with 2 layers of powder are presented with SEM images in Fig. 38. Printing of these multiple-layer parts was conducted at constant laser power (28.5 W) and repetition rate (100 kHz), but at increasing scan speeds (2 mm/s, 20 mm/s, 30 mm/s, and 40 mm/s). Due to excess powder covering the sample in (a), the electron charging effect in the SEM is very strong in the light-colored areas. However, it is possible to observe a relatively dense sample. In addition, an irregular shape of the supposed square sample is evident from the image in Fig. 38 (a). The sample in (c) has lost a small part in the lower left corner during handling, suggesting a brittle mechanical property. Both printed parts in Fig. 38 (b) and (c) share a square shape, but seem to also contain a large fraction of porosity.

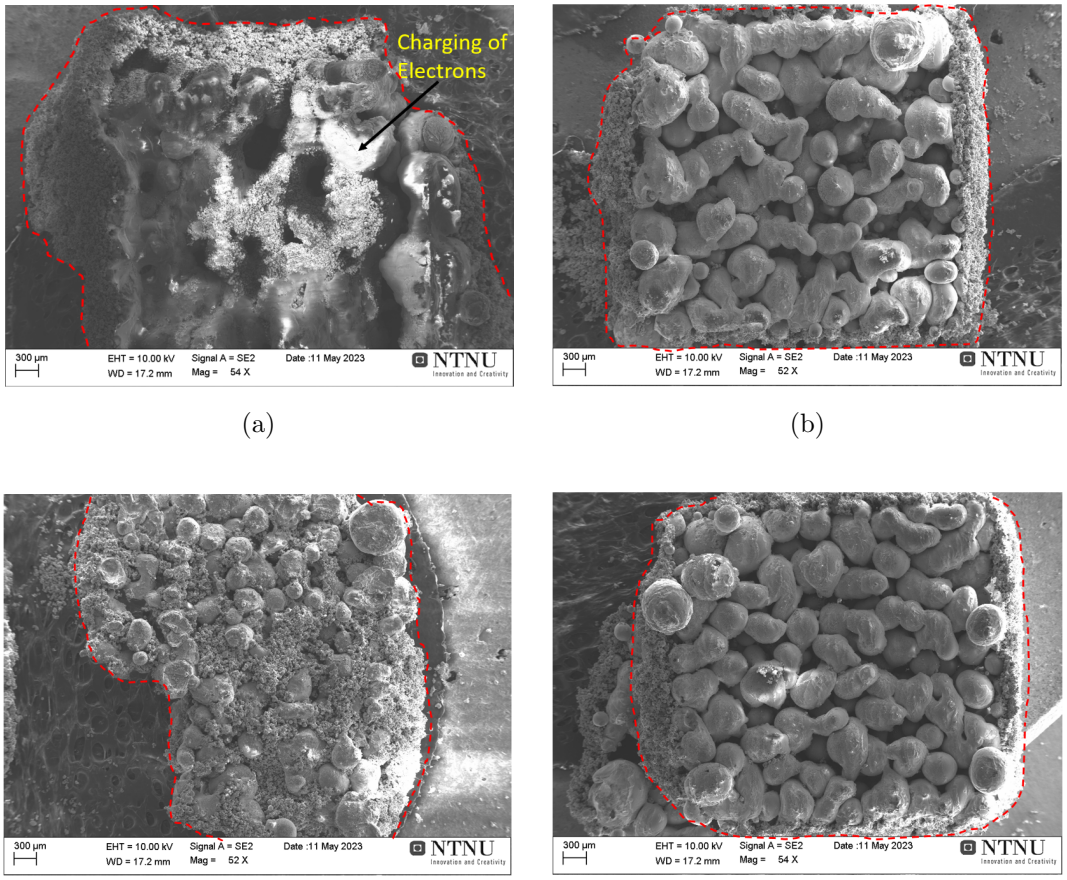

Figure 38: SEM images of the hatched squares with 2 layers of powder and increasing scanning speeds. (a) 2 mm/s, (b) 20 mm/s, (c) 30 mm/s, (d) 40 mm/s. Laser power and repetition rate were held constant at 28.5 W and 100 kHz, respectively. The printed parts are outlined with red dotted lines.

Cross-section OM images of the SLM parts at increasing scan speeds (2 mm/s, 10 mm/s, 15 mm/s, and 20 mm/s) are displayed in Fig. 39 (a-c). These parts were printed with the addition of 2 layers of powder, 28.5 W laser power, and a 100 kHz repetition rate. The cross-sections in (a-c) show a significantly porous structure. Inside the droplets, fine primary Si particles can also be observed.

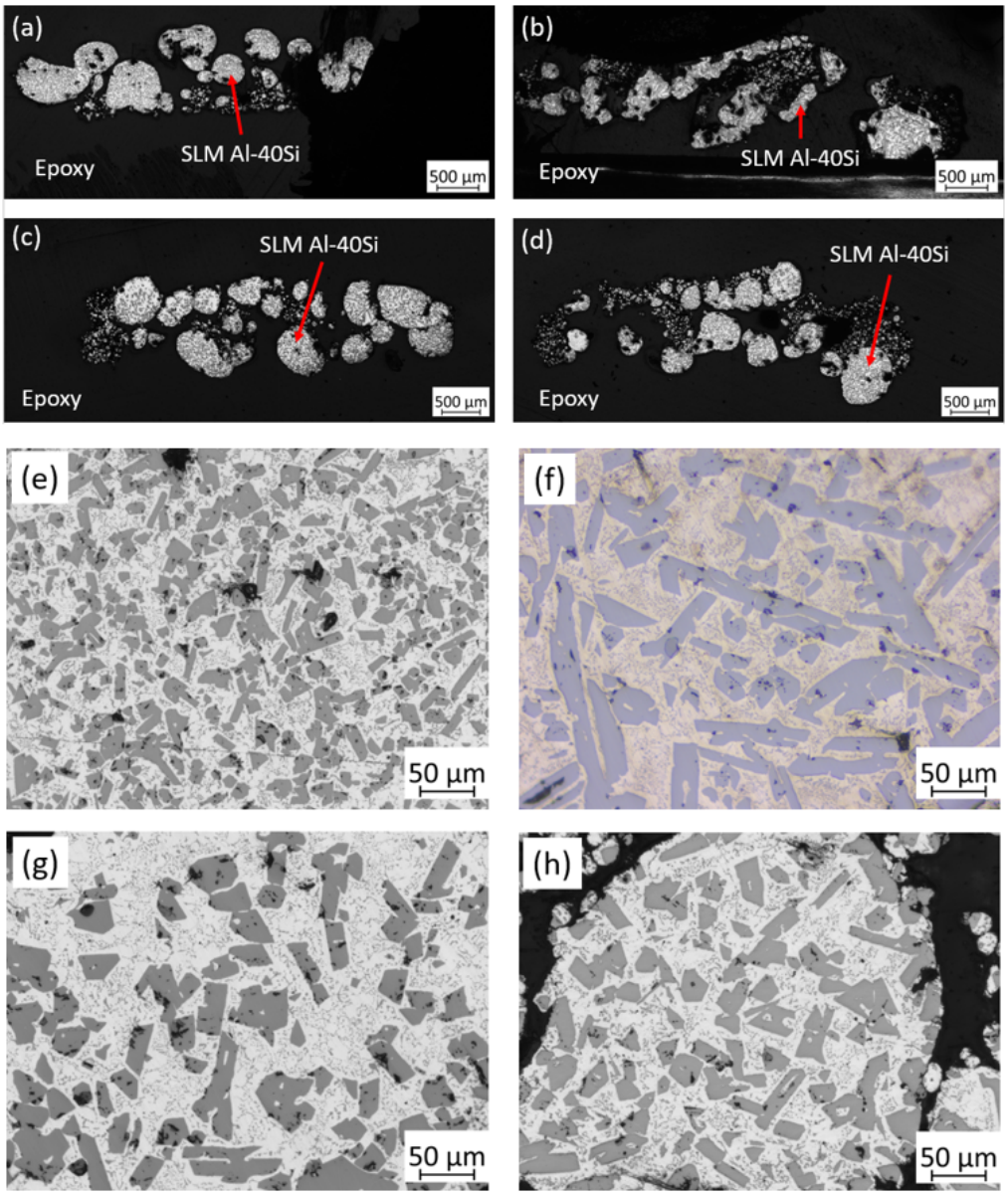

Figure 39: OM images at different magnifications of the cross-section of the 2 layered SLM parts at increasing scan speed. (a) and (e) 2 mm/s. (b) and (f) 10 mm/s. (c) and (g) 15 mm/s. (d) and (h) 20 mm/s. Laser power and repetition rate were held constant at 28.5 W and 100 kHz, respectively.

The 3D printed parts with 4 layers of powder ($\sim$50 μm) are pictured in Fig. 40. The samples were SLM with 28.5 W laser power, 100 kHz repetition rate, and 3 different scan speeds (20 mm/s, 30 mm/s, and 40 mm/s).

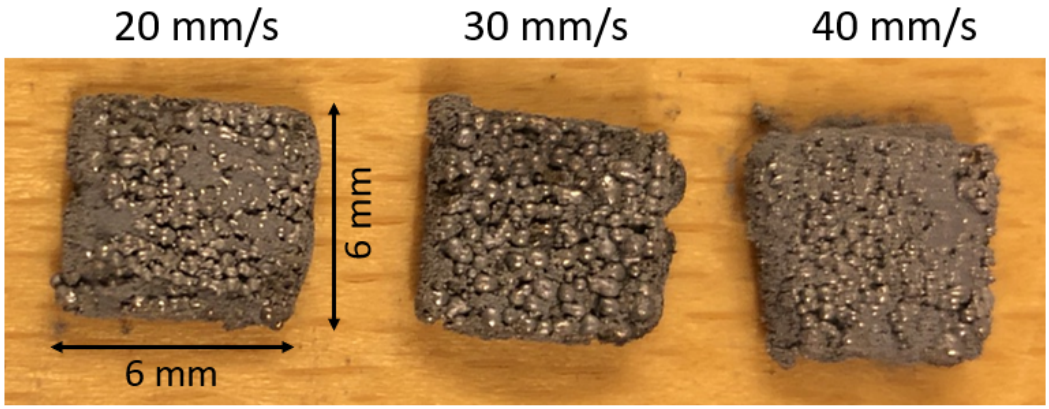

Figure 40: Picture of the 3D printed parts consisting of 4 layers of powder (∼50 μm), 28.5 W laser power, 100 kHz repetition rate. (a) 20 mm/s, (b) 30 mm/s, and (c) 40 mm/s scan speed.

4.5 Preheating

A comparison between the surface of the building plate before and after preheating is shown in Fig. 41 (a) and (b). The SEM image in (a) clearly shows the rough character of the sandblasted Al-40Si building plate. After preheating, a significant difference can be observed in surface structure when comparing (a) to the SEM image in (b).

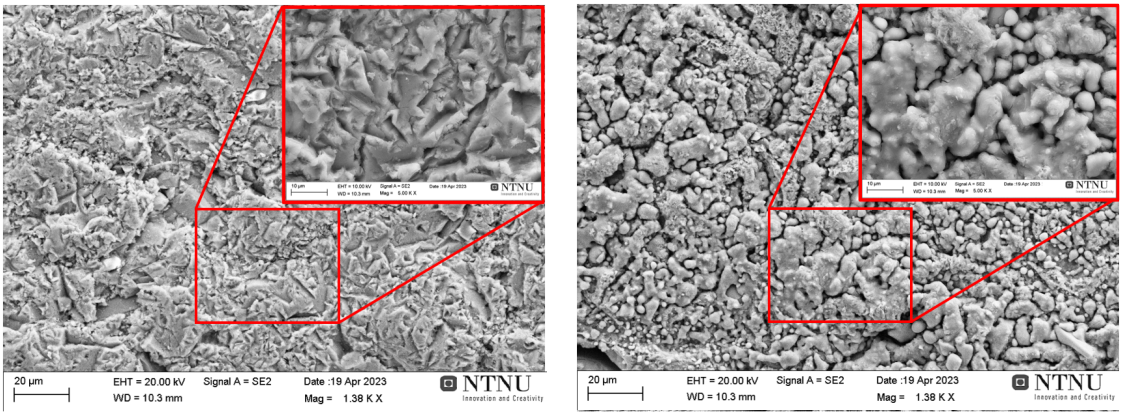

(a) (b)

Figure 41: SEM micrographs of the (a) sandblasted surface of the building plate, and (b) the laser remelted surface of the building plate subsequent to preheating.

The layout of the low-temperature preheating experiment and the resulting laser-scanned disc is presented in Fig. 42 (a) and (b). To compare, the equivalent setup is presented for the high-temperature preheating experiment in Fig. 43 (a) and (b). As Fig. 42 and Fig. 43 show, similar scan speeds were repeated for both of the tests. The remaining laser parameters were kept constant at 28.5 W laser power, and 100 kHz repetition rate.

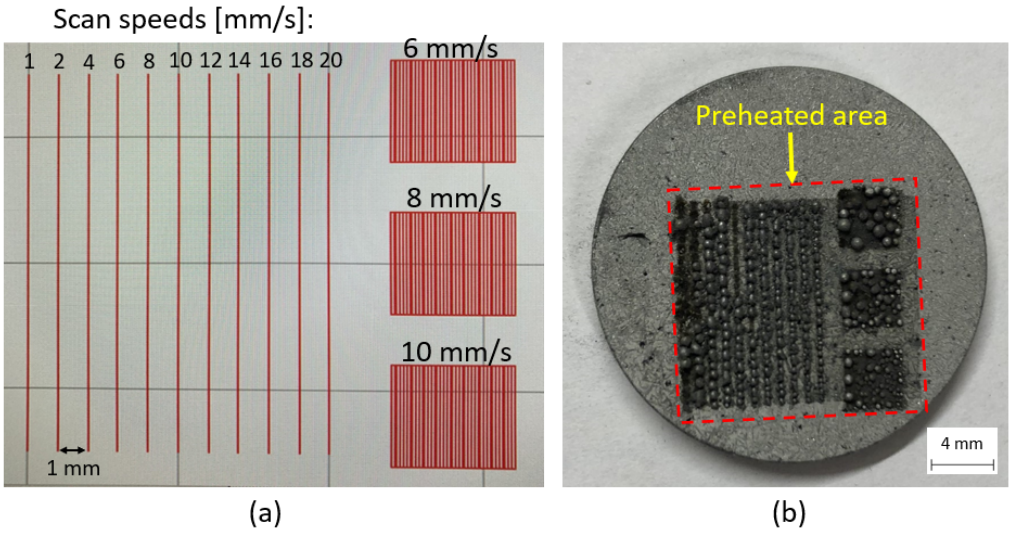

Figure 42: (a) VLM software layout of the lower temperature preheating test, and (b) the resulting laser scanned disc. The preheated area is within the red dotted line. Laser power and repetition rate were held constant at 28.5 W and 100 kHz, respectively.

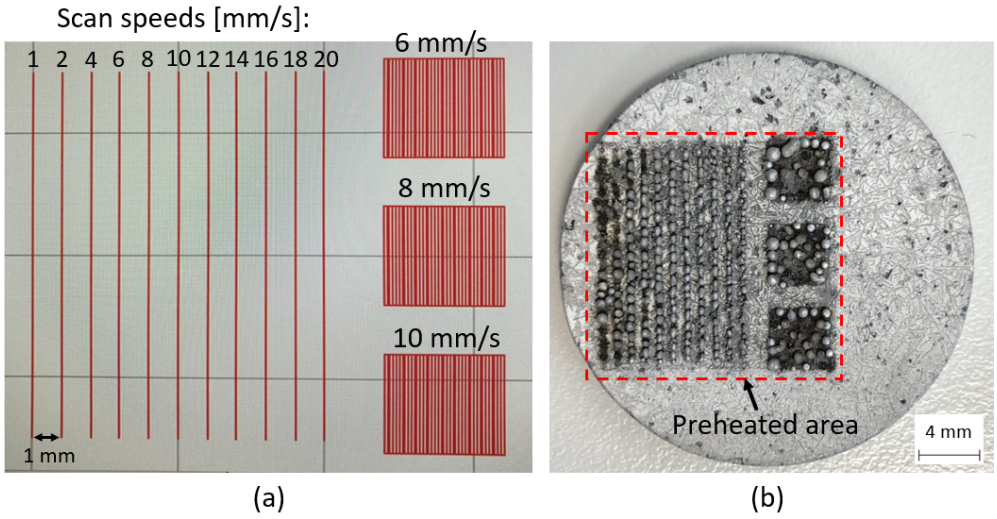

Figure 43: (a) VLM software layout of the higher temperature preheating test, and (b) the resulting laser scanned disc. The preheated area is within the red dotted line. Laser power and repetition rate were held constant at 28.5 W and 100 kHz, respectively.

The average droplet size plotted against the scan speed for the low and high-temperature preheating strategy is presented in Fig. 44 and Fig. 45, respectively. SEM images are also included in both graphs for a selection of the data points. It is from the graphs that the final droplet size decreases with increasing scan speed.

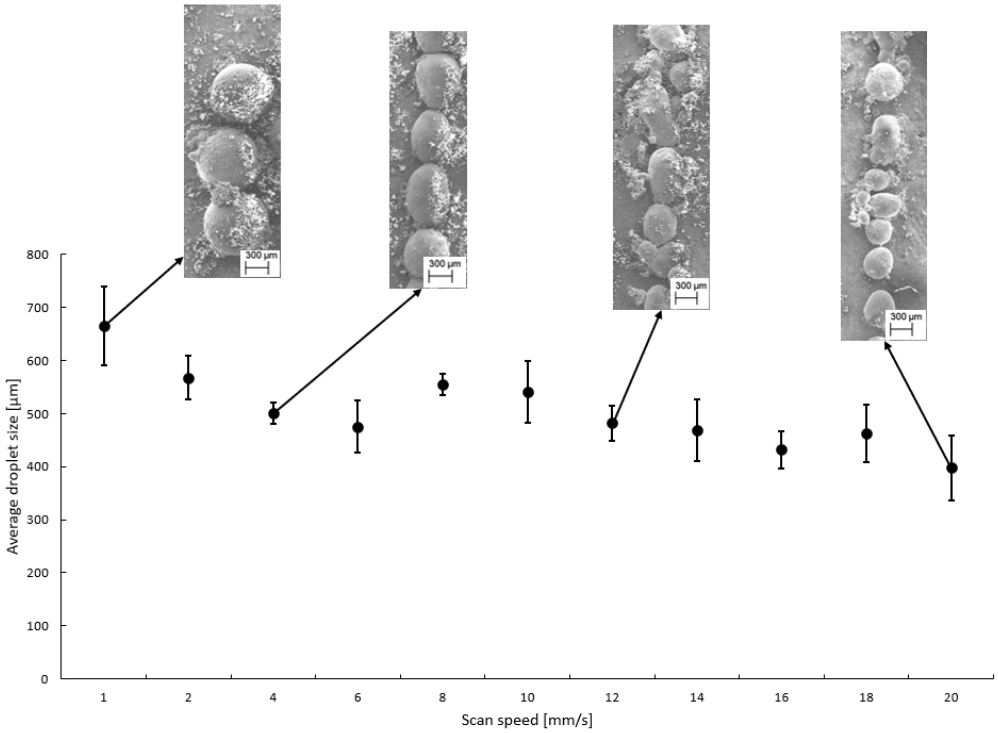

Figure 44: Graph showing the average droplet size (diameter) as a function of scan speed for the low-temperature preheating strategy. A selection of SEM images is also included for some of the data points.

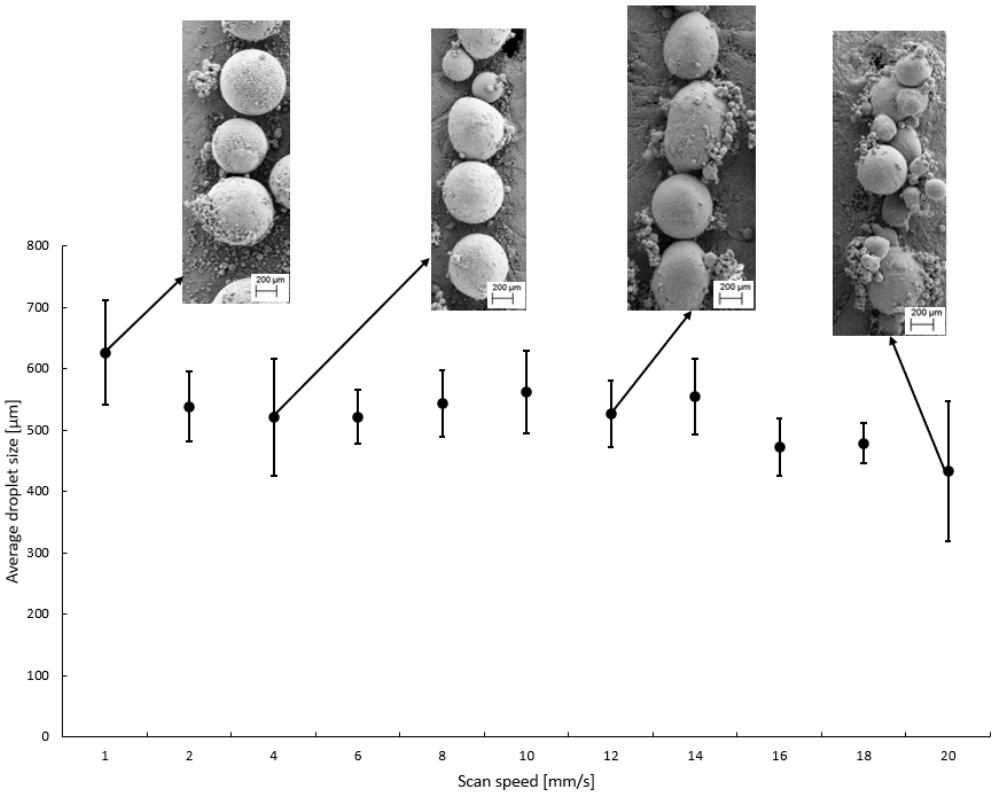

Figure 45: Graph showing the average droplet size (diameter) as a function of scan speed for the high-temperature preheating strategy. A selection of SEM images is also included for some of the data points.

To better visualize the difference between the two preheating strategies, a graph comparing the low and high-temperature experiments with respect to average droplet size against scan speed is shown in Fig. 46. The data sets are produced by analyzing the SEM images by ImageJ. For most of the scans, the high-temperature preheating strategy results in a slightly larger droplet size than the low-temperature preheating strategy.

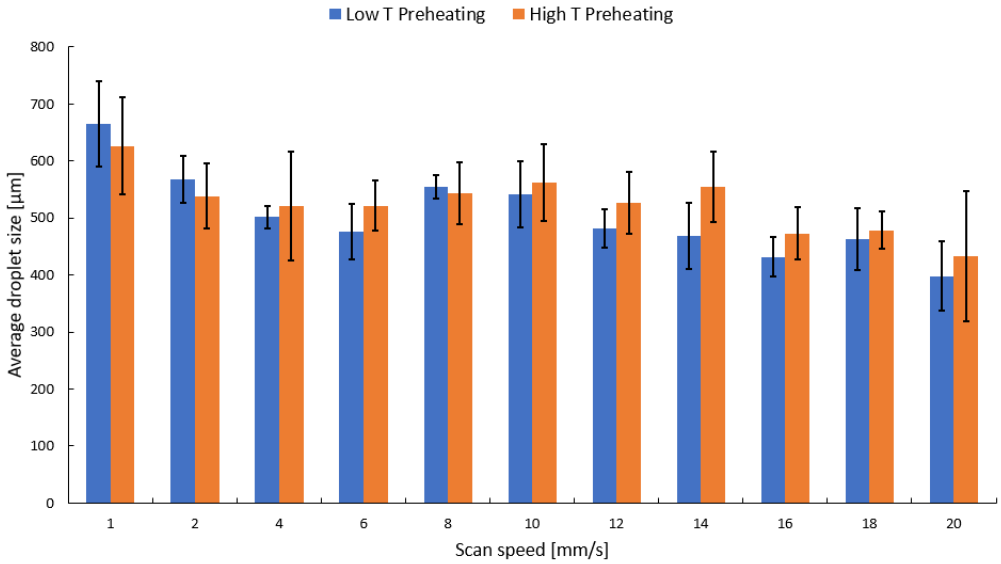

Figure 46: Graph comparing the low and high-temperature preheating strategies with respect to average droplet size and scan speed. The blue columns represent the low-temperature preheating, and the orange columns represent the high-temperature preheating of the single-track scans.

4.6 Rescanning

The experiment where the single layer hatched squares were rescanned with 14.3 W (50 %) laser power and 100 kHz repetition rate is shown in Fig. 47 (a-d). The initial scan was performed with 28.5 W (100 %) laser power and a 100 kHz repetition rate. The scan speeds represented in the SEM images in Fig. 47 are only 25 mm/s, 30 mm/s, 35 mm/s, and 40 mm/s. The reason for this is that the remelted powder at the lower scan speed did not show adhesion to the building plate. As can be seen, after rescanning, the surface of droplets became more smooth than after initial scanning.

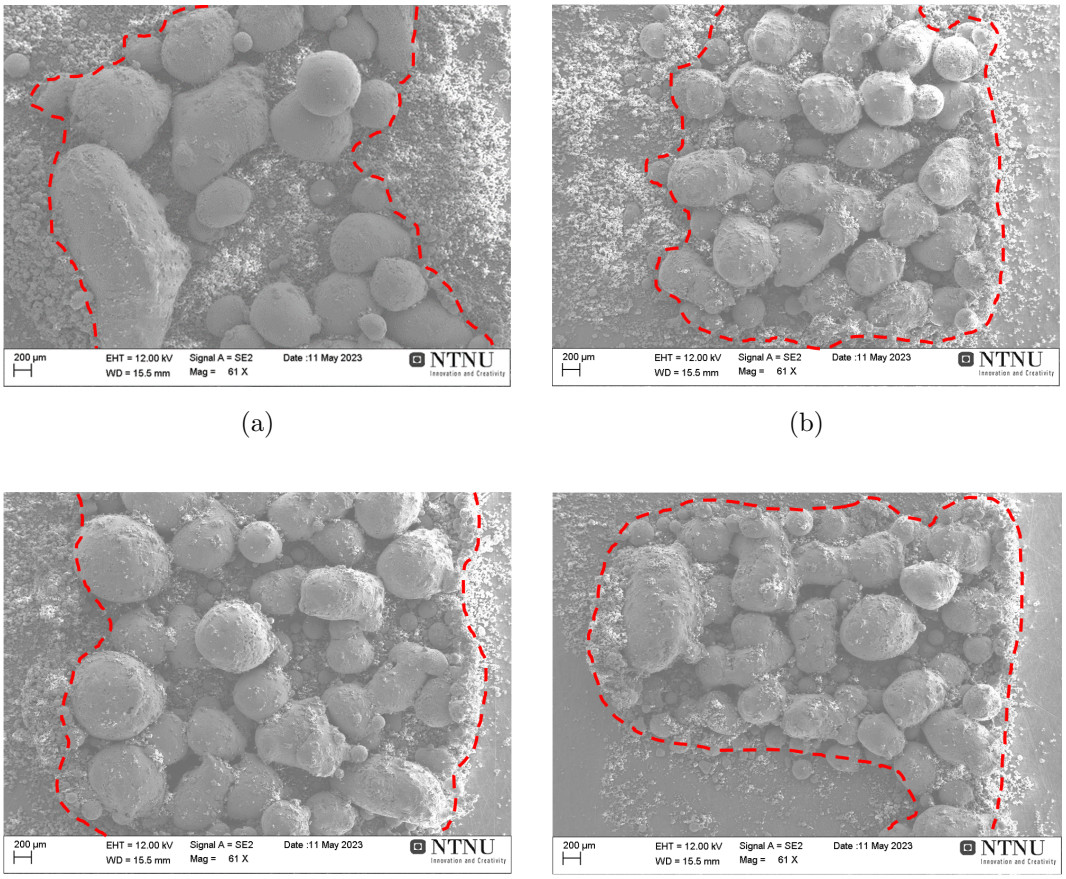

(a) (b)

(c) (d)

Figure 47: SEM images of the single layer hatched squares rescanned at 14.3 W (50 %) laser power with increasing scanning speeds. (a) 25 mm/s, (b) 30 mm/s, (c) 35 mm/s, (d) 40 mm/s. The initial scan was carried out with 28.5 W laser power, and the repetition rate was held constant at 100 kHz. The printed parts are outlined with red dotted lines.

The graph in Fig. 48 compares no rescanning to rescanning with a 14.3 W (50 %) laser power with respect to average droplet size and scan speed. Notable from the graph is the general large standard deviations.

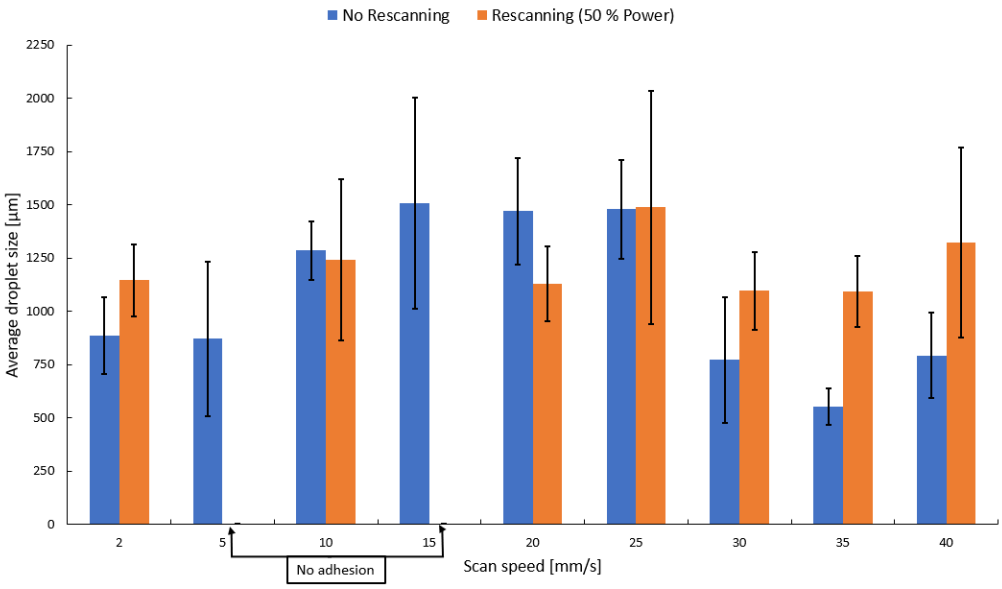

Figure 48: Graph comparing the two scanning strategies of no rescanning, and rescanning with 50 % laser power, with respect to average droplet size and scan speed. The blue columns represent the scans without rescanning, and the orange columns represent the scan with rescanning. Because of no adhesion to the building plate, two orange columns in the rescanning data set are missing.

5 Discussion

5.1 Effect of Scan Speed

As Fig. 31 shows, the tendency of decreasing average droplet size with increasing scan speed is obvious. The scan speed and linear energy can be seen as being inversely proportional to each other if all other parameters are kept constant. Since this study for the most part has fixed the laser power to the printer's maximum (28.5 W), it does not matter which of the parameters above we use to describe the tendencies observed. The SEM images in the same figure (Fig. 31) also display the non-continuous character of the single-track scans. The balling phenomenon described in section 2.6.3 is undoubtedly visible in these images. Unfortunately, the only difference visible when moving from low to high scan speeds is the sizes of the droplets formed, i.e. the balling occurs for the entirety of the scan speeds from 1 mm/s to 70 mm/s. As the adhesion summary graph in Fig. 32 shows this tendency will not stop appearing at scan speeds over 70 mm/s either. By studying the graph it is evident that no adhesion of the powder was registered at scan speeds over 70 mm/s. This may indicate that scan speeds over 70 mm/s combined with 28.5 W laser power and 100 kHz repetition rate is not sufficient to melt a $\sim$50 μm layer of Al-40Si powder. This is also the reason that the experimental work adjusted the scan speed to under 70 mm/s early in the parameter optimization process.

By comparing the 25 mm/s to 45 mm/s scan speed single-tracks in Fig. 28, to the 55 mm/s to 70 mm/s single-tracks in Fig. 27, the droplet size variation is apparent. In other words, it was a step in the right direction in the parameter optimization process when adjusting the scan speed below 50 mm/s. However, the 45 mm/s to 25 mm/s scans still were far from forming continuous single tracks. Meanwhile, an improvement towards achieving continuous single tracks was achieved by lowering the scan speeds to under 20 mm/s. Fig. 30 shows SEM images of the single tracks from 1 to 20 mm/s, with 28.5 W laser power and 100 kHz repetition rate. From this figure, the scan speeds of 4 to 12 mm/s are considered the most promising, although a consecutive line of remelted powder is not present.

The initial single-track scanning was a great way of narrowing the parameter search down, but the multiple-layer parts are surely closer to conventional 3D printing. Fig. 38 (a-d) presents the surface of the 2 layered printed parts with scan speeds from 2 to 40 mm/s and 28.5 W laser power. The part that seemingly has the densest structure, only considering the surface view, is the part in (a). This sample was produced with a 2 mm/s scan speed, which evidently has provided a large energy input. Unlike the parts in (b-d), the part in (a) appears to be solid and without voids between a number of remelted droplets. As the aim of this parameter SLM study is to find the parameters that build the densest and most solid component, this is a promising result. Nevertheless, the mechanical properties of the sample in (a) have not been experimentally tested, but simple handling of the sample in conjunction with this study proved it to be of a brittle character.

Moving on to the 2-layer printed parts cross-section, the OM images in Fig. 39 (a-h) reveal the microstructure within. The lower magnification images in (a-d) demonstrate the porosity in the parts, as discussed before. The individual size of the droplets appearing in the cross-section image (a-d) once again shows how the increase in scanning speed corresponds to smaller droplet sizes. Furthermore, the OM images in (e-f) give a higher magnification view of the microstructure of the same samples. From these images, the dark-colored Si particles seem to be of a relatively coarse character. In theory, the slower scan speeds should result in a longer melt pool lifetime, and thereby coarser grains (2.9). It is, however, not obvious to observe a general trend in average grain size with respect to scanning speed in these images. This may have to do with the fact that the resulting microstructure is closely related to the melt pool and droplet size. Local variations in the printed parts can thus appear and further make it difficult to conclude the effect of scan speed on microstructure. Anyhow, the SLM parts show a much finer microstructure than observed in the wedge cast building plate, imaged in Fig. 25. This proves the promising aspect of utilizing SLM on hypereutectic Al-Si alloys, ensuing grain boundary strengthening (section 2.8), and the possibility of producing parts with super strength.

From the discussion above it is prominent that the scanning speed has an effect on energy input, which ultimately gives a larger droplet diameter. This can be explained by the laser

beam having more time to melt powder along the scanning path, thereby increasing the size of the melt pool. The enhanced size of the melt pool results in larger droplet sizes. Unfortunately, the scan speed alone is not capable of altering the fluid flow of the molten powder, which causes the spheroidisation of the printed parts. The mechanisms behind this phenomenon will be discussed in section 5.7.

5.2 Effect of Laser Power

When studying the cross-section of the single tracks in Fig. 25 and Fig. 26, there are little signs of melt pool formation in the underlying substrate. This may suggest that the laser was unable to penetrate through the powder and into the substrate, i.e. too low laser power was available. The imbalance in laser power is significant comparing the PowerLine F 30 laser used in this work to conventional lasers utilized in the SLM process. Commonly, laser powers from 100 to 500 W are available in the industry [12]. To replicate a conventional 3D printer with the laser available in this project consequently may serve as a challenge. The small degree of melting in the building plate surface also facilitates a limited contact area to the remelted droplet, demonstrated in Fig. 25 (b).

5.3 Effect of Repetition Rate

An important objective in the early parameter study was to find the effect of the repetition rate. The experiment in single track scan test 2 in section 4.1.2 contributed to understanding this effect. The single-track scans with a 30 kHz repetition rate conducted in this parameter test did not adhere to the building plate. As pointed out in section 2.3.2 earlier studies by Ullsperger et al. [26] on metal powders of similar alloy compositions have shown that low repetition rates may cause a blasting effect on the irradiated powder. This can explain the effect observed in this study at low repetition rates (30 kHz).

Fig. 27 compares the 30 kHz repetition rate with the 100 kHz repetition rate, holding all other laser parameters constant. By first studying the SEM image in Fig. 27 (a) displaying 4 single tracks at scan speeds between 70 to 55 mm/s and 30 kHz repetition rate, remelting of the building plate surface is apparent. Moreover, it is possible to follow the path where the laser has irradiated the surface with a number of small droplets arranged in almost straight lines. Again, given the relatively tiny size of the droplets, the 30 kHz repetition seems to have blasted away the majority of the Al-40Si powder. When comparing these single tracks, to the 100 kHz scans imaged in Fig. 27 (b), a large difference is clear. The tracks conducted at the highest scan speeds of 70 and 65 mm/s show little sign of remelted powder on the surface. This may imply that the accelerated 100 kHz frequency has not provided sufficient peak power to remelt the powder, as addressed in the laser pulse parameter section 2.3.2. It was here argued that holding the average laser power constant (28.5 W) and varying the repetition rate (30-100 kHz) will cause the peak power to also

shift by 10^2 orders of magnitude. The fluctuation of the peak power is also presented in the laser parameter Table 2, 3, and 4. In these tables, a constant average power of 28.5 W corresponds to 57 W and 95 kW peak power, for the 100 kHz and 30 kHz repetition rates, respectively. To compensate for significantly higher peak power the pulse duration is lowered from $1.0 \cdot 10^{-7}$ to $5.0 \cdot 10^{-6}$, as the tables also show. In other words, the 30 kHz repetition rate combines shorter pulses with high peak power, causing a blasting effect on the metal powder. The significantly high peak power also remelts the surface as indicated in Fig. 27 (a). Meanwhile, the 100 kHz repetition rate couples a low peak power with longer pulses, remelting the metal powder, but not necessarily causing adhesion to the building plate. As Fig. 27 (b) illustrates, slower scan speeds (60-55 mm/s) are necessary for the laser to create adhesion between the remelted powder and the building plate. Unfortunately, the longer pulse duration conjugated to a 100 kHz repetition rate also gives the remelted powder time to form spherical droplets.

5.4 Effect of Hatching Distance

The multiple track scanning and hatched square scanning presented in Fig. 33 and Fig. 35, were done to determine the effect of hatching distance. Beginning with the multiple scans conducted with 0.05 hatching distance, the large droplet size of the remelted powder is prominent. The diameter of the largest droplets for the tracks at 2 mm/s, 4 mm/s, 6 mm/s, and 8 mm/s is displayed in Fig. 34. Ranging from about 580 μm to 515 μm, the droplet diameters are larger compared to the single track droplet diameters shown in Fig. 31. The single-track scans that were carried out at similar scan speeds (2-8 mm/s) as the multiple scans have in comparison droplet diameters ranging from roughly 430 μm to 370 μm. Seemingly, the effect of having a hatching distance of 50 μm (0.05 mm) is that the droplet sizes enhance. One theory that may support this observation is that the enlarged melt pool, caused by the tightly packed scanning pattern, forms one single line of droplets. Consequently, the enhanced access to more liquefied metal powder results in significantly large spheres of remelted powder. In addition, it is possible to observe that smaller almost continuous lines of remelted powder follow the outer edge of each scanned track. These tracks may be too far away from the middle line of enhanced droplets and given too little time before solidification, to migrate into the middle section of the multiple scans.

Similar observations as already discussed above regarding the hatching distance were also present for the hatched square scans. When utilizing a hatching overlap of 20 %, the printed parts showed to consist of larger continuous droplets compared to the single scan testing, illustrated in Fig. 37. A theory justifying this is the extended melt pool lifetime that provides added time for the balling mechanisms (section 2.11) to occur.

5.5 Effect of Preheating

The effect of the preheating method utilized in this work, where the building plate was laser scanned at slow scan speeds to reach higher temperature is presented in Fig. 41 (a) and (b). The irradiated (preheated) surface in (b) has experienced considerable remelting. As mentioned in the experimental part 3.4.1, the surface temperature of the substrate during the preheating was not monitored. Also considering the good thermal conductivity of the Al-40Si alloy in the building plate, it is difficult to pinpoint the exact temperatures reached in the building plate other than the fact that it was noticeable. This is a reasonable statement bearing in mind that the surface at some point in the preheating process may have reached a temperature over the solidus line of the alloy.

One of the purposes of experimenting with preheating in the SLM process was to eliminate the Marangoni convection forces defined in section 2.11. In short, this phenomenon causes the molten metal inside the droplet to flow such that a spheroidisation of the remelted powder occurs. The convection flow occurring is driven by an internal difference in temperature inside the metal droplet. Consequently, a logical way of restricting this balling phenomenon is to level out the temperature differences between the remelted powder and the building plate by preheating the latter. The resulting laser-scanned discs from the preheating experiments are presented in Fig. 42 and Fig. 43. These images give an overview of how the laser-scanned discs came out subsequent to SLM, but do not offer easy comparison due to the poor resolution. The graphs presented in Fig. 44 and Fig. 45, however, provide an improved analysis of the preheating strategies. As the integrated SEM images in these figures show, the irregularly shaped single tracks are still present. The decrease in the Marangoni convection is, in other words, not sufficient for either of the preheating strategies (low T and high T preheating).

The graph in Fig. 46 presents a comparison of the low and high-temperature preheating with respect to average droplet size and scan speed. The majority of the respective scan speeds show that the high-temperature preheating results in the largest average droplet sizes. This can be explained by the higher temperature in the powder before laser irradiation decreasing the necessary energy input for the powder to remelt. A lower threshold to energy input will in turn give the powder additional time in the melted phase, inducing large droplets. Nevertheless, the error bars in the same graph unveil substantial deviations for a large portion of the data. The tendency of larger average droplet sizes for the single tracks with high-temperature preheating might therefore be overshadowed by these deviations.

5.6 Effect of Rescanning

The primary advantage of rescanning the same scanning pattern on the printed metal parts with a lower laser power is to improve the uniformity of the melt pools and decrease

the residual stresses [7, 35]. Since the rescanning experiment in this study only included a single layer of powder, it does not make sense to investigate the effect on residual stresses, as they tend to be a problem when adding several layers on top of each other. That being said, it is still possible to consider the effect of rescanning on the uniformity of the melt pools. A selection of the results from the single-layer rescanning test is presented in Fig. 47 (a-d). As the SEM images show, outlined with red dotted lines, the rescanning has not improved the uniformity of the droplets noticeably. The main effect of the extra irradiation, however, seems to be increased droplet sizes. This effect is certainly apparent in Fig. 48, where no rescanning is compared to rescanning with respect to droplet size and scan speed. From this graph, it is observable that droplet sizes for the rescanned samples obtain a generally higher average droplet size. This effect can be explained by the theory where the already printed layer is remelted again, giving additional time for the spherical melt pool to grow, thus forming larger solidified droplets.

Also noticeable in the graph, is the large error bars indicating a high degree of standard deviation. However, the fact that a high degree of standard deviation is present is not necessarily a negative attribute. By studying the SEM images in Fig. 47 this data is based on, the printed part consists of a few large agglomerates in combination with a number of smaller ones. To base the average droplet size on the measurement of the 5 largest droplets, will consequently result in a high degree of deviation. Otherwise stated, the presence of large droplets may be a testimony to the laser parameters being closer to forming a continuous dense part than the evenly distributed droplets.

5.7 Spheroidisation and Morphology of the Printed Parts

A reappearing issue in the printed parts was the problem of balling. This has proven to be a particular challenge for the Al-Si alloy, which has been reported in earlier studies. In a study by Olakanmi et al. [59], one argument for balling to occur when performing SLM on an Al-12Si alloy was the lower thermal conductivity of the powder bed. Thus, when the laser beam impacts the powder bed high temperatures and steep thermal gradients will occur, and the Marangoni convection will increase. The effect of Marangoni convection was elaborated in section 2.11, where spheroidisation of the melt pool was pointed out as a consequence. Also reported in the same study as a cause for balling to occur was the difference in wettability of the powder bed and sintered layers. The high degree of mismatch between the oxide film and the parent metal was in section 2.10 appointed to be one of the reasons for balling to transpire in the SLM process. Moreover, a rough building plate surface, as can be seen in Fig. 41 (a) and (b), has proven to facilitate even higher wetting angles [61]. All of the possible causes for balling to appear in the SLM of Al-Si alloys mentioned above have defiantly limited the success of quality in the printed parts.

Another interesting observation made by Olkanmi et al. [59] was that the spheroidisation phenomenon of Al-Si powders was extra prevailing in the single layer parts. This result

can also be found in this study in Fig. 35 and Fig. 36. However, when studying the SEM images of the multiple layered parts in Fig. 38, the balling effect seems to be less transpiring. Particularly the sample in Fig. 38 (a) produced with 2 mm/s scan speed, 28.5 W laser power, and 100 kHz repetition rate shows little signs of balling. A theory explaining this outcome is the protruded droplets from the first layer of powder remelting along with the newly deposited layer. As a consequence, a larger portion of the metal part is fused together. Longer sections of interconnected agglomerates can also be seen in Fig. 38 (b-d), which also can be explained by the same remelting mechanism. Meanwhile, the apparent shape of the printed part in Fig. 38 (a) with a high linear input energy (14.25 J/mm) is significantly deformed. This can indicate that an excessive amount of liquid phase followed by a longer melt pool lifetime has caused the irregular shape.

The excessive balling of the single-track scans, illustrated in Fig. 30 may have a tightly bound connection with Plateau-Rayleigh instability. As derived in section 2.11, the Plateau-Rayleigh instability is the effect that causes a stream of liquid to break up into smaller drops. The minimum time for a liquid cylinder, i.e. melt pool, to break up is proportional to the diameter of the pool. Roughly estimated with equation 16 in section 2.11, the break-up time for the Al-40Si alloy was calculated to be 0.16 ms. Regardless of the specific break-up time, it indicates that the time for spheroidisation to occur is extremely small. By this, it is possible to draw the conclusion that the melt pool will have sufficient time to form agglomerates in the SLM process of Al-40Si, as is evident from the results in Fig. 30.

5.8 Equipment and Methodology

Finally, in the discussion section, it is important to highlight some critiques regarding the equipment and methodology employed in this study. As mentioned in the introduction and background section 2.12, the mini-3D printer operated is not a conventional industry standard printer. Despite offering a fair amount of customized laser parameters, the printer does not provide sufficient laser power or repetition rate. This statement is based on observations made in earlier parameter studies [12, 26] on similar alloys, where higher laser power and repetition rates were emphasized as being crucial for optimal printing results. Additionally, the layer thickness proved to be difficult to set correctly with the current powder distribution system, which suffered from failures and jamming especially when the layer thickness was set to below 0.1 mm (100 μm).

Another observation made during the experimental work was the non-horizontal state of the printing bed, pictured in Fig. 19. The powder distribution system with the attached steel blade did also seem to lack the sufficient force to evenly spread the powder onto the powder bed. Also, when attempting to print multiple-layered parts, the combination of the inaccurate actuators and spheroidisation of the remelted powder caused the horizontally moving steel blade to scrape away the printed parts. Consequently, the layer thickness had

to be adjusted manually, detailed elaborated in Appendix C, which resulted in imprecise layer thicknesses. Ideally, the layer thickness should have been about 50 μm, but this assumption may not be entirely correct with the noted flaws of the powder distribution system and powder bed.

Furthermore, the powder handling process and the printing chamber configuration were not flawless. Despite monitoring the oxygen level in the printing chamber, imaged in Fig. 18, the location of the oxygen sensor may corrupt the reading compared to the actual chamber atmosphere. In practice, it is extremely difficult to completely avoid oxidation in the SLM process as the oxygen partial pressure must be really low (section 2.6.4). It should also be noted that the sealing of the chamber consisted of tape that may have caused leaks. Consequently, oxidation is a highly relevant element for the particular printing chamber employed in this project not having an absolute oxygen-free atmosphere. Preferably, all the handling of the Al-40Si powder should have been done in an inert atmosphere. The present configuration of the chamber, however, forces the user to first expose the powder to the surrounding atmosphere before the chamber is sealed and purged with argon gas. This may have had an impact on the results, where oxidation layers in the powder have been suggested as a cause for balling to occur.

6 Conclusion

- Increasing the scanning speed of the laser beam in the single and multiple-layer scanning was found to give the remelted Al-40Si powder smaller droplet diameters. The best printing results were achieved with scanning speeds from 10 to 30 mm/s, 28.5 W (100 %) laser power, 20 % hatching overlap, and a 100 kHz repetition rate of the laser pulse.

- Utilizing the lowest repetition rate (30 kHz), combining high peak powers with short pulses, was observed to have a blasting effect on the powder bed. Meanwhile, the highest repetition rate (100 kHz) provided a larger portion of remelted powder but also resulted in spheroidisation of the melt pool.

- Balling of the printed parts proved to be a significant issue with the mini 3D printer for SLM of the Al-40Si powder on the wedge cast and sandblasted Al-40Si building plate. Poor wetting of the melt pool was explained by the high degree of mismatch between the remelted powders and the surface oxide layers of the substrate building plate, Marangoni convection, and Plateau-Rayleigh instability.

- Practicing a hatching distance of 50 μm on the printed parts gave larger droplets, as a consequence of extended melt pool lifetime. Using a 20 % overlapping hatching distance proved to result in even larger remelted droplets.

- The printed parts by preheating the building plate and rescanning indicated negligible effects on the balling. The high-temperature preheating resulted in generally larger droplets, than the low-temperature preheating.

6.1 Future Work

- To decrease the balling defects during SLM, an improvement of the wetting between the remelted droplets, and between the droplets and the substrate surface is crucial. This may be achieved by improving the sealing on the printing chamber and increasing the vacuum level of the chamber during SLM.
- The current methodology of exposing the aluminum powder to the surrounding atmosphere before the initiation of the printing process should be avoided. This can be done by integrating the powder handling into an inert atmosphere.
- To achieve printing parts with more than 4 layers and higher precision in dimension, the powder distribution system has to be re-design. In the present form, the uneven distribution of the powders causes immense problems in the SLM process.

References

[1] M Averyanova et al. 'Experimental design approach to optimize selective laser melting of martensitic 17-4 PH powder: part I–single laser tracks and first layer'. In: *Rapid Prototyping Journal* (2012).

[2] Kaufui Wong and Aldo Hernandez. 'A review of additive manufacturing'. In: *International scholarly research notices* 2012 (2012).

[3] George Alan Leatham, Josef Andrew Widawsk Ogilvy and Luis Elias. 'Silicon Alloys for Electronic Packaging'. Feb. 1997. URL: https://patentscope.wipo.int/search/en/detail.jsf?docId=WO1997003775&_cid=P11-LFMG1Y-29853-1.

[4] Panneer Ponnusamy et al. 'Mechanical properties of SLM-printed aluminium alloys: a review'. In: *Materials* 13.19 (2020), p. 4301.

[5] Rebecca Garrard et al. 'Comparison of LPBF processing of AlSi40 alloy using blended and pre-alloyed powder'. In: *Additive Manufacturing Letters* 2 (2022), p. 100038. ISSN: 2772-3690. DOI: https://doi.org/10.1016/j.addlet.2022.100038.

[6] Nan Kang et al. 'Microstructure and wear behavior of in-situ hypereutectic Al–high Si alloys produced by selective laser melting'. In: *Materials & Design* 99 (2016), pp. 120–126. ISSN: 0264-1275. DOI: https://doi.org/10.1016/j.matdes.2016.03.053.

[7] T Ullsperger et al. 'Selective laser melting of hypereutectic Al-Si40-powder using ultra-short laser pulses'. In: *Applied Physics A* 123.12 (2017), p. 798.

[8] Mohammad H. Farshidianfar, Amir Khajepour and Adrian P. Gerlich. 'Effect of real-time cooling rate on microstructure in Laser Additive Manufacturing'. In: *Journal of Materials Processing Technology* 231 (2016), pp. 468–478. ISSN: 0924-0136. DOI: https://doi.org/10.1016/j.jmatprotec.2016.01.017.

[9] Rahman Rashid et al. 'Effect of scan strategy on density and metallurgical properties of 17-4PH parts printed by Selective Laser Melting (SLM)'. In: *Journal of Materials Processing Technology* 249 (2017), pp. 502–511.

[10] Audun Mostad et al. 'Development of miniature metal 3D printer'. May 2022. URL: https://hdl.handle.net/11250/3002913.

[11] Dominik Deradjat and Tim Minshall. 'Implementation of rapid manufacturing for mass customisation'. In: *Journal of Manufacturing Technology Management* (2017).

[12] N. T. Aboulkhair et al. '3D printing of Aluminium alloys: Additive Manufacturing of Aluminium alloys using selective laser melting'. In: *Elsevier* 106 (2019). DOI: https://doi.org/10.1016/j.pmatsci.2019.100578.

[13] *What is an STL file? - Everything You Need To Know About This File Format.* URL: https://www.sculpteo.com/en/3d-learning-hub/create-3d-file/what-is-an-stl-file/. (accessed: 06.10.2022).

[14] *CAD-to-STL Process.* URL: https://www.3dtechno.in/cad-to-stl/. (accessed: 06.10.2022).

[15] *HOW 3D PRINTING WORKS?* 2017. URL: http://my3dconcepts.com/explore/how-3d-printing-works/. (accessed: 06.10.2022).

[16] Shahir M. Yusuf and Nong Gao. 'Influence of energy density on metallurgy and properties in metal additive manufacturing'. In: *Materials Science and Technology* 33.11 (2017), pp. 1269–1289. DOI: 10.1080/02670836.2017.1289444.

[17] Simon Pauly et al. 'Experimental determination of cooling rates in selectively laser-melted eutectic Al-33Cu'. In: *Additive Manufacturing* 22 (2018), pp. 753–757. ISSN: 2214-8604. DOI: https://doi.org/10.1016/j.addma.2018.05.034.

[18] Meurig Thomas, Gavin J. Baxter and Iain Todd. 'Normalised model-based processing diagrams for additive layer manufacture of engineering alloys'. In: *Acta Materialia* 108 (2016), pp. 26–35. ISSN: 1359-6454. DOI: https://doi.org/10.1016/j.actamat.2016.02.025.

[19] E.O. Olakanmi, R.F. Cochrane and K.W. Dalgarno. 'Densification mechanism and microstructural evolution in selective laser sintering of Al–12Si powders'. In: *Journal of Materials Processing Technology* 211.1 (2011), pp. 113–121. ISSN: 0924-0136. DOI: https://doi.org/10.1016/j.jmatprotec.2010.09.003.

[20] Jianfeng Sun, Yongqiang Yang and Di Wang. 'Parametric optimization of selective laser melting for forming Ti6Al4V samples by Taguchi method'. In: *Optics & Laser Technology* 49 (2013), pp. 118–124. ISSN: 0030-3992. DOI: https://doi.org/10.1016/j.optlastec.2012.12.002.

[21] Robby Ebert et al. 'Investigation of cw and ultrashort pulse laser irradiation of powder surfaces: a comparative study'. In: *Laser Applications in Microelectronic and Optoelectronic Manufacturing (LAMOM) XVIII*. Vol. 8607. SPIE. 2013, pp. 93–103.

[22] Boris N Chichkov et al. 'Femtosecond, picosecond and nanosecond laser ablation of solids'. In: *Applied physics A* 63.2 (1996), pp. 109–115.

[23] Tobias Ullsperger et al. 'Ultra-short pulsed laser powder bed fusion of Al-Si alloys: Impact of pulse duration and energy in comparison to continuous wave excitation'. In: *Additive Manufacturing* 46 (2021), p. 102085. ISSN: 2214-8604. DOI: https://doi.org/10.1016/j.addma.2021.102085.

[24] *Pulse Parameters*. URL: https://www.thorlabs.com/newgrouppage9.cfm?objectgroup_id=10823#ad-image-0. (accessed: 08.12.2022).

[25] Lisa Kaden et al. 'Additive manufacturing of pure copper using ultrashort laser pulses'. In: *Laser 3D Manufacturing VI*. Vol. 10909. SPIE. 2019, pp. 49–55.

[26] Tobias Ullsperger et al. 'Laser assisted powder bed fusion of hypereutectic Al-Si using ultra-short laser pulses at different pulse durations (Conference Presentation)'. In: *Laser 3D Manufacturing VII*. Vol. 11271. SPIE. 2020, p. 112710M.

[27] Jun Hao Tan, Wai Leong Eugene Wong and Kenneth William Dalgarno. 'An overview of powder granulometry on feedstock and part performance in the selective laser melting process'. In: *Additive Manufacturing* 18 (2017), pp. 228–255. DOI: https://doi.org/10.1016/j.addma.2017.10.011.

[28] Rainer J Hebert. 'Metallurgical aspects of powder bed metal additive manufacturing'. In: *Journal of Materials Science* 51.3 (2016), pp. 1165–1175. DOI: https://doi.org/10.1007/s10853-015-9479-x.

[29] Rongshi Xiao and Xinyi Zhang. 'Problems and issues in laser beam welding of aluminum–lithium alloys'. In: *Journal of Manufacturing Processes* 16.2 (2014), pp. 166–175. ISSN: 1526-6125. DOI: https://doi.org/10.1016/j.jmapro.2013.10.005.

[30] Rongshi Xiao. 'Laser beam welding of aluminum alloys'. In: *Lasers in Material Processing and Manufacturing III*. Vol. 6825. SPIE. 2008, pp. 40–49.

[31] Kun V. Yang et al. 'Porosity formation mechanisms and fatigue response in Al-Si-Mg alloys made by selective laser melting'. In: *Materials Science and Engineering: A* 712 (2018), pp. 166–174. ISSN: 0921-5093. DOI: https://doi.org/10.1016/j.msea.2017.11.078.

[32] KH Hou and WA Baeslack. 'Effect of solute segregation on the weld fusion zone microstructure in CO2 laser beam and gas tungsten arc welds in Al-Li-Cu alloy 2195'. In: *Journal of materials science letters* 15.3 (1996), pp. 208–213.

[33] Christian Weingarten et al. 'Formation and reduction of hydrogen porosity during selective laser melting of AlSi10Mg'. In: *Journal of Materials Processing Technology* 221 (2015), pp. 112–120. ISSN: 0924-0136. DOI: https://doi.org/10.1016/j.jmatprotec.2015.02.013.

[34] Nesma T. Aboulkhair et al. 'Reducing porosity in AlSi10Mg parts processed by selective laser melting'. In: *Additive Manufacturing* 1-4 (2014). Inaugural Issue, pp. 77–86. ISSN: 2214-8604. DOI: https://doi.org/10.1016/j.addma.2014.08.001.

[35] M. Shiomi et al. 'Residual Stress within Metallic Model Made by Selective Laser Melting Process'. In: *CIRP Annals* 53.1 (2004), pp. 195–198. ISSN: 0007-8506. DOI: https://doi.org/10.1016/S0007-8506(07)60677-5.

[36] Dongdong Gu and Yifu Shen. 'Balling phenomena in direct laser sintering of stainless steel powder: Metallurgical mechanisms and control methods'. In: *Materials & Design* 30.8 (2009), pp. 2903–2910. ISSN: 0261-3069. DOI: https://doi.org/10.1016/j.matdes.2009.01.013.

[37] A. Simchi and H. Pohl. 'Direct laser sintering of iron–graphite powder mixture'. In: *Materials Science and Engineering: A* 383.2 (2004), pp. 191–200. ISSN: 0921-5093. DOI: https://doi.org/10.1016/j.msea.2004.05.070.

[38] Suman Das. 'Physical aspects of process control in selective laser sintering of metals'. In: *Advanced Engineering Materials* 5.10 (2003), pp. 701–711.

[39] Eleftherios Louvis, Peter Fox and Christopher J Sutcliffe. 'Selective laser melting of aluminium components'. In: *Journal of Materials Processing Technology* 211.2 (2011), pp. 275–284. DOI: https://doi.org/10.1016/j.jmatprotec.2010.09.019.

[40] B Engel and DL Bourell. 'Titanium alloy powder preparation for selective laser sintering'. In: *Rapid Prototyping Journal* 6.2 (2000), pp. 97–106.

[41] R. Mertens et al. 'Application of base plate preheating during selective laser melting'. In: *Procedia CIRP* 74 (2018). 10th CIRP Conference on Photonic Technologies [LANE 2018], pp. 5–11. ISSN: 2212-8271. DOI: https://doi.org/10.1016/j.procir.2018.08.002.

[42] Saad Waqar, Kai Guo and Jie Sun. 'Evolution of residual stress behavior in selective laser melting (SLM) of 316L stainless steel through preheating and in-situ re-scanning techniques'. In: *Optics & Laser Technology* 149 (2022), p. 107806. ISSN: 0030-3992. DOI: https://doi.org/10.1016/j.optlastec.2021.107806.

[43] Karolien Kempen et al. 'Lowering thermal gradients in selective laser melting by pre-heating the baseplate'. In: *Solid Freeform Fabrication Symposium Proceedings*. 2013.

[44] Ketai He and Xue Zhao. '3D thermal finite element analysis of the SLM 316L parts with microstructural correlations'. In: *Complexity* 2018 (2018).

[45] Wenyou Zhang, Mingming Tong and Noel M. Harrison. 'Scanning strategies effect on temperature, residual stress and deformation by multi-laser beam powder bed fusion manufacturing'. In: *Additive Manufacturing* 36 (2020), p. 101507. ISSN: 2214-8604. DOI: https://doi.org/10.1016/j.addma.2020.101507.

[46] Jamasp Jhabvala et al. 'On the effect of scanning strategies in the selective laser melting process'. In: *Virtual and physical prototyping* 5.2 (2010), pp. 99–109.

[47] Haolin Jia et al. 'Scanning strategy in selective laser melting (SLM): a review'. In: *The International Journal of Advanced Manufacturing Technology* 113 (2021), pp. 2413–2435.

[48] R Stamp et al. 'The development of a scanning strategy for the manufacture of porous biomaterials by selective laser melting'. In: *Journal of Materials Science: Materials in Medicine* 20 (2009), pp. 1839–1848.

[49] Jan Ketil Solberg. *Teknologiske metaller og legeringer*. Ed. by Institutt for materialteknologi NTNU. 2017, pp. 209–214.

[50] Ren-Guo Guan and Di Tie. 'A review on grain refinement of aluminum alloys: progresses, challenges and prospects'. In: *Acta Metallurgica Sinica (English Letters)* 30.5 (2017), pp. 409–432.

[51] Nan Kang et al. 'Characterization of the microstructure of a selective laser melting processed Al-50Si alloy: Effect of heat treatments'. In: *Materials Characterization* 130 (2017), pp. 243–249. ISSN: 1044-5803. DOI: https://doi.org/10.1016/j.matchar.2017.06.026.

[52] Karolien Kempen et al. 'Processing AlSi10Mg by selective laser melting: parameter optimisation and material characterisation'. In: *Materials Science and Technology* 31.8 (2015), pp. 917–923.

[53] Zhang et al. 'Formation of microstructure in Al-Si alloys under ultrasonic melt treatment'. In: *Light metals 2012* (2016), pp. 999–1004.

[54] S.C. Hogg et al. 'Microstructural characterisation of spray formed Si–30Al for thermal management applications'. In: *Scripta Materialia* 55.1 (2006). Viewpoint set no. 41 "3D Characterization and Analysis of Materials" Organized by G. Spanos, pp. 111–114. ISSN: 1359-6462. DOI: https://doi.org/10.1016/j.scriptamat.2006.02.051.

[55] K.G. Prashanth and J. Eckert. 'Formation of metastable cellular microstructures in selective laser melted alloys'. In: *Journal of Alloys and Compounds* 707 (2017). Selected papers presented at ISMANAM 2016, July 3rd-8th, Nara, Japan, pp. 27–34. ISSN: 0925-8388. DOI: https://doi.org/10.1016/j.jallcom.2016.12.209.

[56] Eyitayo Olatunde Olakanmi, Robert F Cochrane and Kenneth W Dalgarno. 'A review on selective laser sintering/melting (SLS/SLM) of aluminium alloy powders: Processing, microstructure, and properties'. In: *Progress in Materials Science* 74 (2015), pp. 401–477.

[57] David Edward Bunnell. *Fundamentals of selective laser sintering of metals*. The University of Texas at Austin, 1995.

[58] KURIAN Antony, N Arivazhagan and K Senthilkumaran. 'Studies on wettability of stainless steel 316L powder in laser melting process'. In: *Journal of Engineering Science and Technology* 16.3 (2014), pp. 533–540.

[59] EO Olakanmi, RF Cochrane and KW Dalgarno. 'Spheroidisation and oxide disruption phenomena in direct selective laser melting (SLM) of pre-alloyed Al-Mg and Al-Si powders'. In: *Proceedings: TMS Annual Meetings and Exhibition*. 2009, pp. 371–380.

[60] Pierre-Gilles De Gennes. 'Wetting: statics and dynamics'. In: *Reviews of modern physics* 57.3 (1985), p. 827.

[61] Jie Liu et al. 'Influence of substrate surface morphology on wetting behavior of tracks during selective laser melting of aluminum-based alloys'. In: *Journal of Zhejiang University-SCIENCE A* 19.2 (2018), pp. 111–121.

[62] Chieko Ishino, Ko Okumura and David Quéré. 'Wetting transitions on rough surfaces'. In: *Europhysics Letters* 68.3 (2004), p. 419.

[63] 'Chapter 23 - Plateau-Rayleigh Instability'. In: *Microfluidics: Modelling, Mechanics and Mathematics*. Ed. by Bastian E. Rapp. Micro and Nano Technologies. Oxford: Elsevier, 2017, pp. 467–477. ISBN: 978-1-4557-3141-1. DOI: https://doi.org/10.1016/B978-1-4557-3141-1.50023-X.

[64] Marleen Rombouts et al. 'Fundamentals of selective laser melting of alloyed steel powders'. In: *CIRP annals* 55.1 (2006), pp. 187–192.

[65] Hidekazu Kobatake et al. 'Surface tension of binary Al-Si liquid alloys'. In: *Journal of materials science* 50 (2015), pp. 3351–3360.

[66] *RS Alloys Optics*. URL: https://www.rsp-technology.com/site-media/user-uploads/rsp_alloys_optics_2018lr.pdf. (accessed: 01.06.2023).

[67] E. Bennett et al. 'Telescience with MARCO/HOLOP on board the spacelab D2-mission as a preparation for Columbus'. In: *Acta Astronautica* 26.8 (1992). The Next Century: Prospects for Space, pp. 551–561. ISSN: 0094-5765. DOI: https://doi.org/10.1016/0094-5765(92)90146-A.

[68] *Marangoni Convection*. URL: https://web.archive.org/web/20120308071605/http://www.comsol.com/showroom/gallery/110/. (accessed: 20.04.2023).

[69] Rofin-Sinar Laser Technologies Inc. 'PowerLine F, Operator's Manual'. 2014.

[70] Mari Martini et al. 'Development of 3D-printer for small scale testing of new metal alloys'. May 2021. URL: https://hdl.handle.net/11250/2778181.

[71] *X-VSR Series: Vertical lift stages with built-in controllers*. URL: https://www.zaber.com/products/vertical-stages/X-VSR/specs?part=X-VSR20A. (accessed: 21.05.2023).

[72] Y.D. Jia et al. 'Microstructure and thermal expansion behavior of Al-50Si synthesized by selective laser melting'. In: *Journal of Alloys and Compounds* 699 (2017), pp. 548–553. ISSN: 0925-8388. DOI: https://doi.org/10.1016/j.jallcom.2016.12.429.

[73] University of Cambridge Dissemination of IT for the Promotion of Materials Science. *The Ellingham Diagram*. (accessed: 20.03.2023). 2023. URL: https://www.doitpoms.ac.uk/tlplib/ellingham_diagrams/ellingham.php.

Appendix

A Ellingham Diagram

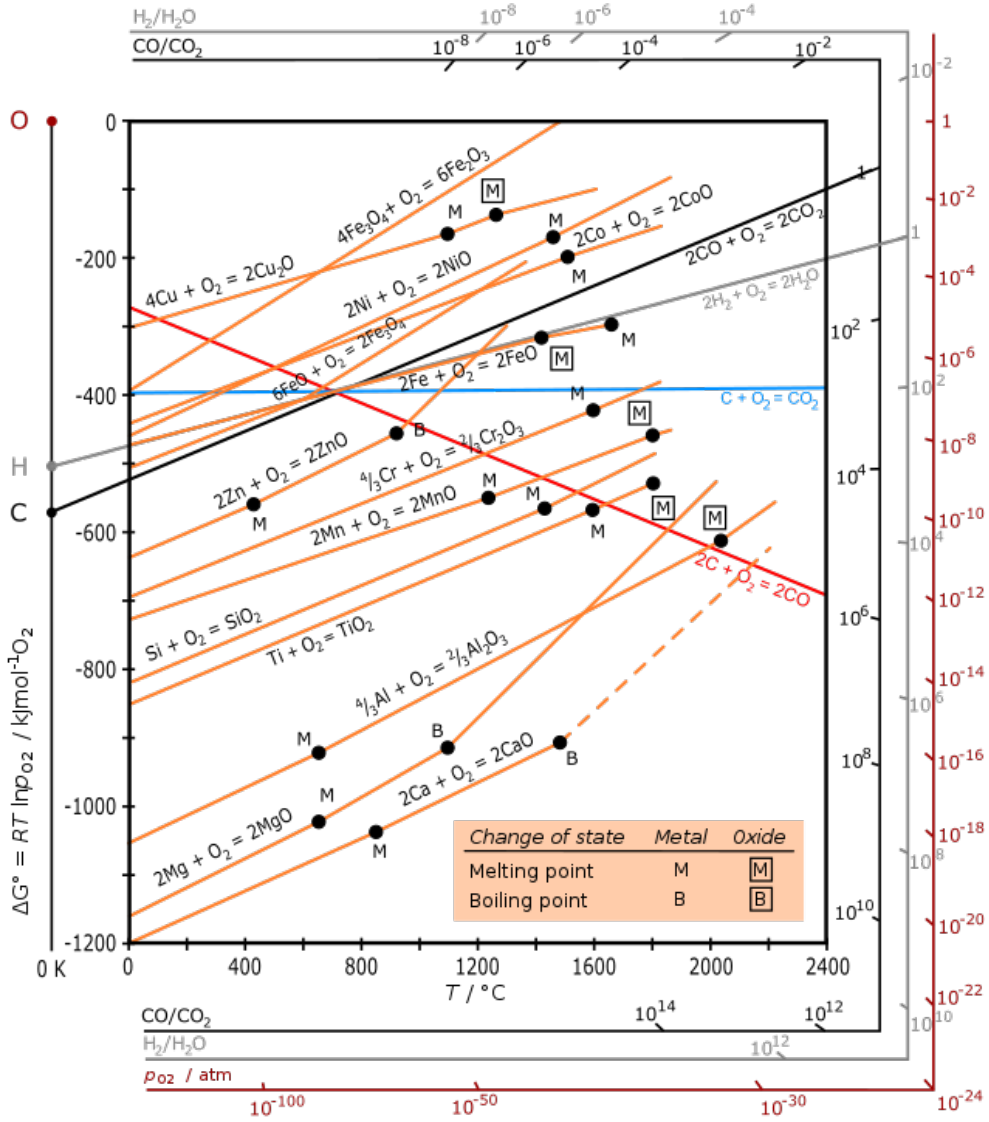

Figure 49: Ellingham diagram, adapted from [73].

B OM Panorama Image

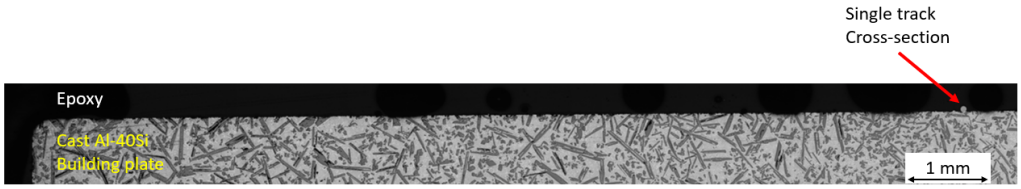

Figure 50: Example of an OM panorama image of the Al-40Si building plate cross-section conducted with the Zen Core software.

C User Guide to Mini 3D Printer for Manual Single-Layer Printing

The printing system consists of two separate systems, the VLM software controlling the laser, and the Rasberry Pi software controlling the powder distribution system (PDS). The printer setup is more thoroughly explained in Mostad et al. bachelor thesis [10]. The 3D printer's original setup was made to print multiple layered components by inserting a USB stick with a CAD file of the part. The system would then run automatically printing the part. Since this project demanded the possibility to print single-layered parts, the system software was updated. The update involved adding some new features to the PDS controlling software, enabling manual control of the powder bed, print bed, and powder distributor. In this user guide, the procedure of how to print single-layer parts with the new functions will be described step-wise below.

1. Power up the mini 3D printer by turning the main switch located just below the front panel. Remember to have inserted a USB stick connected to the powder distribution system controlling the computer. If no USB stick is inserted, the system will not function.

2. The keyboard needs to be manually switched between the two monitors for the VLM software, and the PDS software. Therefore, ensure that the keyboard is connected to the PDS monitor, via the USB entrance.

3. Click and open "Eitri.desktop" → Execute. The PDS controlling graphical user interface (GUI) will now appear, as shown in Fig. 51.

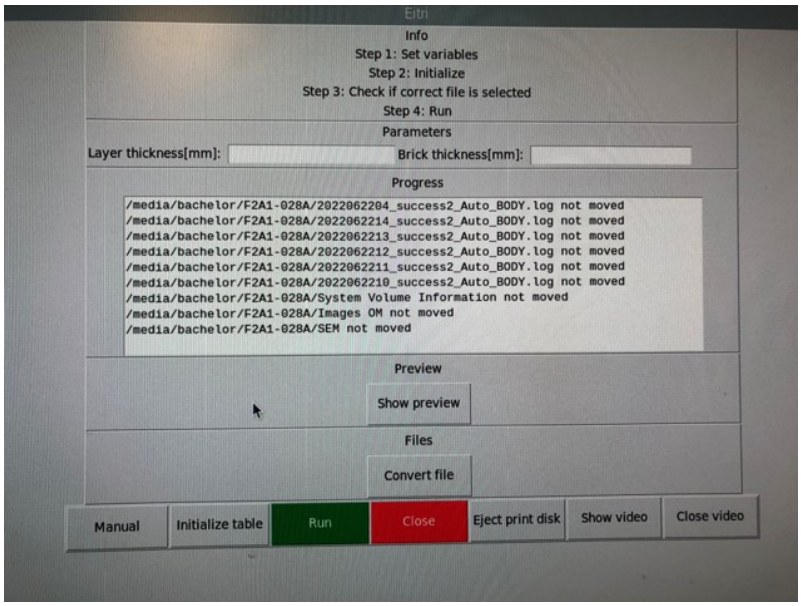

Figure 51: Graphical user interface (GUI) controlling the PDS system.

4. Set the desired layer thickness and brick thickness in the entry boxes.

5. Click on the “Manual” button. A new window will pop up, shown in Fig. 52, where it is possible to manually move the powder bed and print bed. For each button click, the actuators will move with a step size according to the layer thickness set earlier.

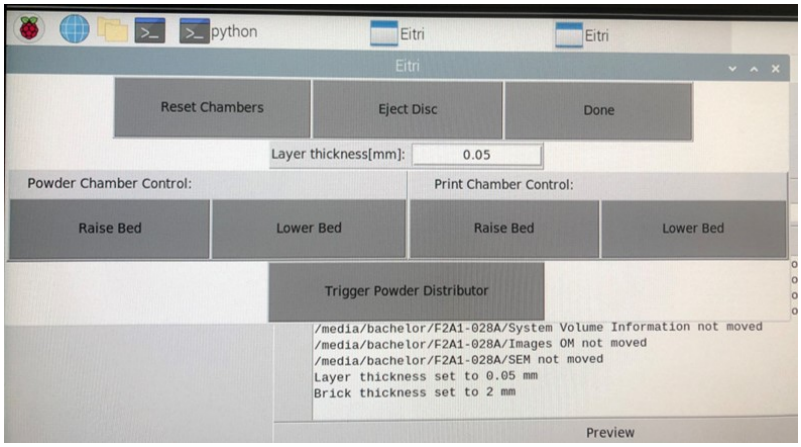

Figure 52: Manual PDS window.

6. To have a visual on the printing stage when operating, it is possible to click on the ”Show Video”. A live camera view of the printing stage should then appear in the bottom right corner, as pictured in Fig. 53.

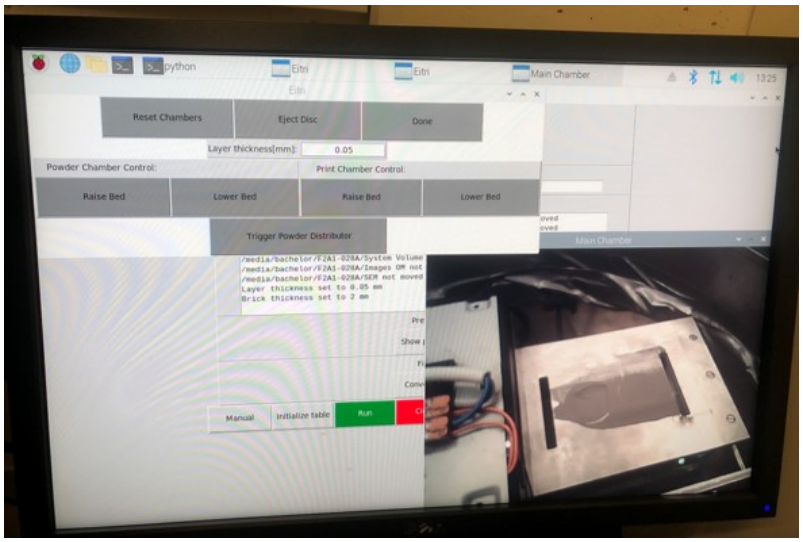

Figure 53: Manual PDS user interface with live video feed in the bottom right corner.

7. Make sure the powder bed is filled with a sufficient amount of powder corresponding number of layers to be printed.

8. Also make sure that the print bed is at the starting point, level with the rest of the printing surface. This can be done by clicking "Reset Chambers".

9. Then move the powder bed up, by clicking "Raise Bed" in the powder chamber control. The powder bed is now ready to distribute a new layer of powder onto the print bed.

10. Correspondingly move the print bed down, by clicking "Lower Bed". The print bed will move stepwise equal to the layer thickness for each click on the button. Consequently, one layer of powder with the entered layer thickness is achieved by clicking the button only once.

11. The horizontal actuator is now ready to be triggered by clicking "Trigger Powder Distributor". Click the same button one more time to bring it back to its initial position.

12. The print bed should now be covered with one single layer of powder, and is ready to be scanned. The desired scanning pattern is set in the VLM software. See Mostad et al. [10] for instructions on how to create a drawing in VLM.

13. To seal the chamber, place the plexiglass on top of the chamber, and press down to ensure a tight seal. The chamber is now ready to be purged with argon gas.

14. Before opening the argon gas bottle valve, start the oxygen detector by pressing the orange "ON/OFF" button. The detector will take 2-3 minutes to initialize.

15. When the oxygen detector display starts to show the oxygen level in real-time, the next step is to flush the chamber with argon gas. This is done by gently opening

the main valve on the gas bottle. The oxygen level can be monitored on the oxygen detector display.

16. When the oxygen level is below 0.1-0.2 %, the laser scanning can be initialized. The process of starting the laser scanning is described in the Rofin Laser manual [69], and in the mentioned bachelor thesis [10].

17. After printing a single layer, the procedure above can be repeated to print multiple layers. The printed sample is extracted from the printing stage by pressing the "Eject Disc" button.

18. When finished with the printing procedure, remember to turn off the argon gas, oxygen detector, and Eitri machine.

NTNU

Norwegian University of
Science and Technology